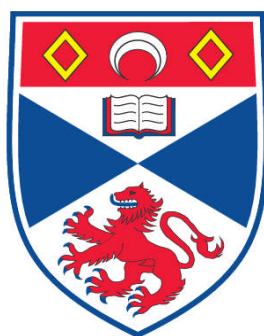


**APPLICATIONS OF ORDERED MESOPOROUS METAL OXIDES:
ENERGY STORAGE, ADSORPTION, AND CATALYSIS**

Yu Ren

**A Thesis Submitted for the Degree of PhD
at the
University of St. Andrews**



2010

**Full metadata for this item is available in
Research@StAndrews:FullText
at:**

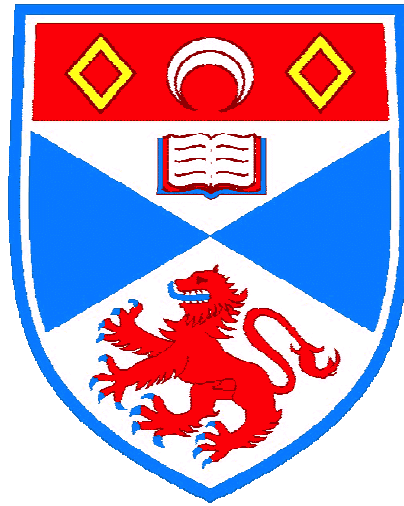
<https://research-repository.st-andrews.ac.uk/>

Please use this identifier to cite or link to this item:

<http://hdl.handle.net/10023/1705>

This item is protected by original copyright

**This item is licensed under a
Creative Commons License**



Applications of Ordered Mesoporous Metal Oxides: Energy Storage, Adsorption, and Catalysis.

A Thesis presented for the degree of
Doctor of Philosophy
in the Faculty of Science of the University of St. Andrews
by Yu Ren

July 2010

School of Chemistry
St. Andrews

1. Candidate's declarations:

I,, hereby certify that this thesis, which is approximately 32,000 words in length, has been written by me, that it is the record of work carried out by me and that it has not been submitted in any previous application for a higher degree.

I was admitted as a research student in September 2006 and as a candidate for the degree of Doctor of Philosophy in September 2006; the higher study for which this is a record was carried out in the University of St Andrews between 2006 and 2010.

Date signature of candidate

2. Supervisor's declaration:

I hereby certify that the candidate has fulfilled the conditions of the Resolution and Regulations appropriate for the degree of in the University of St Andrews and that the candidate is qualified to submit this thesis in application for that degree.

Date signature of supervisor

3. Permission for electronic publication:

In submitting this thesis to the University of St Andrews I understand that I am giving permission for it to be made available for use in accordance with the regulations of the University Library for the time being in force, subject to any copyright vested in the work not being affected thereby. I also understand that the title and the abstract will be published, and that a copy of the work may be made and supplied to any bona fide library or research worker, that my thesis will be electronically accessible for personal or research use unless exempt by award of an embargo as requested below, and that the library has the right to migrate my thesis into new electronic forms as required to ensure continued access to the thesis. I have obtained any third-party copyright permissions that may be required in order to allow such access and migration, or have requested the appropriate embargo below.

The following is an agreed request by candidate and supervisor regarding the electronic publication of this thesis:

Access to printed copy and electronic publication of thesis through the University of St Andrews.

Date signature of candidate

signature of supervisor

Acknowledgements

First of all, I would like to say great thanks to my supervisor, Prof. Peter Bruce, for his breaking through ideas and valuable guidance throughout the research work, which are essential to make this thesis possible.

I also would show special thanks to our scientific collaborators, Prof. Russell E. Morris of University of St Andrews, Prof. Heyong He and Dr. Zhen Ma of Fudan University, Dr. Sheng Dai of Oakridge National Lab, Prof. Clare P. Grey of Stony Brook University, and Dr. Dr. Martin Wilkening of Leibniz University Hannover. Their idea and time to collaborate on the work presented in this thesis or still under going.

Thanks to all the people who help me on many things: Mrs. Sylvia Williamson for measuring adsorption, chemical analysis, and thermalgravimetry, Dr. Adrian H. Hill for collecting magnetic information and neutron data, Dr. Rob Armstrong for collecting and refining the neutron data, Dr. Bo Xiao for collecting NO adsorption data, Miss Astrid-Karla Boes for collecting copper oxide catalytic data, Dr. Laurence Hardwick for the Raman spectroscopy measurement, and other people in PGB group for their help.

Finally I would like to thank my family, especially my wife, Huili Tang, for their understanding, support and love, to make all these into reality.

Contents	Page
Abstract	i-ii
Chapter 1. Introduction	1-19
1.1 A brief history of mesoporous materials	1-3
1.2 Soft templated transitional metal oxides	3-4
1.3 Ordered mesoporous metal oxides prepared by the hard template method	5-9
1.4 Comparison of the soft and hard template methods	9-11
1.5 Applications of ordered mesoporous metal oxides	11
1.5.1 Energy conversion and storage	11-14
1.5.2 Catalysis	14-16
1.5.3 Gas sensing	16-18
1.5.4 adsorption and separation	18-19
1.6 Target of this research	19
Chapter 2. Routine characterization techniques	20-33
2.1 Powder X-ray diffraction technique (PXRD)	20-22
2.2 <i>Ex situ</i> and <i>in situ</i> Raman spectroscopy	22-23
2.3 EXAFS	23-24
2.4 Neutron diffraction	24-25
2.5 Adsorption	25-27
2.5.1 Isotherms and hysteresis	25-26
2.5.2 Useful information from the adsorption analysis: Brunauer-Emmett-Teller (BET) surface area, pore size distribution, pore volume	26-27
2.6 Transmission electron microscopy	27-29
2.7 Magnetic properties by Superconducting Quantum Interference Devices (SQUID)	29-30
2.8 Thermogravimetry (TG)	30-31
2.9 Catalytic Co oxidation test	31

2.10 Electrochemical measurements	31-33
Chapter 3. Routine materials preparation	34-38
3.1 KIT-6 at different hydrothermal temperatures	34
3.2 KIT-6 at different calcination temperatures	34
3.3 Disordered mesoporous silica with <i>ca.</i> 8 nm pore	34-35
3.4 Two-step impregnation method for mesoporous Co ₃ O ₄	35
3.5 One-step ethanol evaporation method for mesoporous CeO ₂ , α -Fe ₂ O ₃ , and NiCoMnO ₄	35-36
3.6 Synthesis of mesoporous Cr ₂ O ₃ , β -MnO ₂ , Mn ₂ O ₃ , and NiO by the 'two-solvent' method	36
3.7 Preparation of the other mesoporous β -MnO ₂	36-37
3.8 Nitrate combustion method for mesoporous CuO	37
3.9 Dual template preparation of mesoporous manganese α -MnO ₂	37
3.10 Post-synthesis reduction for mesoporous Mn ₃ O ₄ and Cu-Cu ₂ O	37
3.11 Preparation of mesoporous anatase	38
Chapter 4. Tailoring the pore size/wall thickness of mesoporous transition metal oxides- mesoporous Co₃O₄	39-44
4.1 KIT-6 templates	39-41
4.2 Mesoporous Co ₃ O ₄	41-44
4.3 Conclusions	43
Chapter 5 Influence of size on the rate of mesoporous electrodes for lithium batteries	45-59
5.1 Results and discussion	45-58
5.1.1 Control of pore size/wall thickness	45-49
5.1.2 The structure of mesoporous Li _x MnO ₂ - β	49-50
5.1.3 Electrochemical behavior	50-53
5.1.4 Influence of mesodimensions on the two-phase intercalation reaction (first discharge of β -MnO ₂)	54-56
5.1.5 First discharge capacity at low rates	56-57
5.1.6 Influence of meso-dimensions on the single phase intercalation reaction (10th discharge of β -MnO ₂)	57-58
5.2 Conclusions	58-59

Chapter 6. Lithium intercalation into mesoporous anatase with an ordered 3D pore structure	60-69
6.1 Characterization by TEM, PXRD, and N ₂ sorption	60-63
6.2 Structure evolution by <i>ex situ</i> PXRD and <i>in situ</i> Raman microscopy	64-65
6.3 Electrochemical performance	65-69
6.4 Conclusion	69
Chapter 7. Ordered crystalline mesoporous α-MnO₂	70-77
7.1 Characterization of mesoporous α -MnO ₂	70-
7.1.1 TEM, XRD, N ₂ adsorption	70-73
7.1.2 Characterization of microporosity by N ₂ and CO ₂ adsorption, and HRTEM	73-74
7.1.3 Electrochemistry	74-76
7.1.4 Magnetic properties	76-77
7.2 Conclusion	77
Chapter 8. Ordered crystalline mesoporous Cu_xO exhibiting high NO storage capacity	78-86
8.1 Characterization of mesoporous Cu _x O by XRD, TEM, and N ₂ adsorption	78-83
8.2 NO adsorption and delivery	83-86
8.3 Conclusion	86
Chapter 9. Catalytic CO oxidation by mesoporous metal oxides	87-96
9.1 Mesoporous metal oxides characterized by PXRD, TEM, and N ₂ sorption	87-90
9.2 Catalytic CO oxidation	90-95
9.3 Conclusions	95-96
Chapter 10. Conclusions and future work	97-98
References	99-106
Publication list	I
List of Abbreviations and Acronyms	II

Abstract

The experimental data and results demonstrated here illustrate the preparation and application of mesoporous metal oxides in energy storage, adsorption, and catalysis.

First, a new method of controlling the pore size and wall thickness of mesoporous silica was developed by controlling the calcination temperature. A series of such silica were used as hard templates to prepare the mesoporous metal oxide Co_3O_4 .

Using other methods, such as varying the silica template hydrothermal treatment temperature, using colloid silica, varying the materials ratio etc., a series of mesoporous $\beta\text{-MnO}_2$ with different pore size and wall thickness were prepared. By using these materials it has been possible to explore the influence of pore size and wall thickness on the rate of lithium intercalation into mesoporous electrode.

There is intense interest in lithium intercalation into titanates due to their potential advantages (safety, rate) replacing graphite for new generation Li-ion battery. After the preparation of an ordered 3D mesoporous anatase the lithium intercalation as anode material has been investigated.

To the best of our knowledge, there are no reports of ordered crystalline mesoporous metal oxides with microporous walls. Here, for the first time, the preparation and characterization of three dimensional ordered crystalline mesoporous $\alpha\text{-MnO}_2$ with microporous wall was described, in which K^+ and KIT-6 mesoporous silica act to template the micropores and mesopores, respectively. It was used as a cathode material for Li-ion battery. Its adsorption behavior and magnetic property was also surveyed.

Following this we described the preparation and characterization of mesoporous CuO and reduced Cu_xO , and demonstrated their application in NO adsorption and delivery.

Finally a series of crystalline mesoporous metal oxides were prepared and evaluated as catalysts for the CO oxidation.

Chapter 1 Introduction

Nanoporous materials have attracted a great deal of technological interest during the past two decades, due to their wide range of applications including as catalysts, molecular sieves, separators and gas sensors, as well as electronic and electrochemical devices.¹⁻⁶ Most syntheses of nanoporous materials reported to date have focused on template-assisted, bottom-up processes, including soft templating (chelating agents, surfactants, block copolymers etc.)⁷⁻¹¹ and hard templating¹²⁻¹⁴ (porous alumina, carbon nanotubes, nanoporous silica and carbon) methods.

1.1 A brief history of mesoporous materials

According to the IUPAC definition, porous materials may be divided into three categories: pores with widths exceeding ~ 50 nm are called macropores; pores of widths between 2 and 50 nm are called mesopores; pores with widths not exceeding 2 nm are called micropores.¹⁵ Microporous aluminosilicates (zeolites) have been widely used as 'molecular sieving' catalysts in the petrochemical industry since later 1960s. In 1983, the first titanosilicate analogue zeolite, TS-1, was developed by Taramasso et al. (Enichem);¹⁶ it shows high activity as a heterogeneous catalyst for oxidation reactions. However, the small pore size of microporous zeolite materials or crystalline metal organic frameworks (which are a more recent class of microporous solid) greatly limit their applications. Although mesoporous silica or alumina gels are already commercially available as catalyst supporters, the first ordered mesoporous silica, MCM-41S, was only reported in the early 1990s.^{7,17} MCM-41 has a 2D hexagonal pore structure (Fig. 1-1), with a small pore diameter of 2-3 nm, a wall thickness of about 1 nm, large BET surface area of 600-1000 m²/g, and a pore volume of 0.8-1.0 cm³/g. MCM-41 is unstable due to its thin pore wall, compromising its potential application in catalysis, gas storage, and as a molecular filter etc.^{1,9,18} Subsequently, other mesoporous silicas were prepared as well including the 3D MCM-48, HMS, MSU.^{19,20}

In 1998 a new mesoporous silica SBA-15 was reported using a block copolymer as the template.²¹ It has the same mesopore symmetry as MCM-41, but with larger pore size (~ 8 nm diameter), thicker pore walls (~ 3 nm) and is much more stable. SBA-15 exhibits disordered micropores in the walls resulting from polymer template embedded in the

silica walls during the self-assembly process.^{22,23} Such microporosity influences the structure of replica materials formed using the silica as a hard template, such as the mesoporous 3D interconnected carbon CMK-3.²⁴

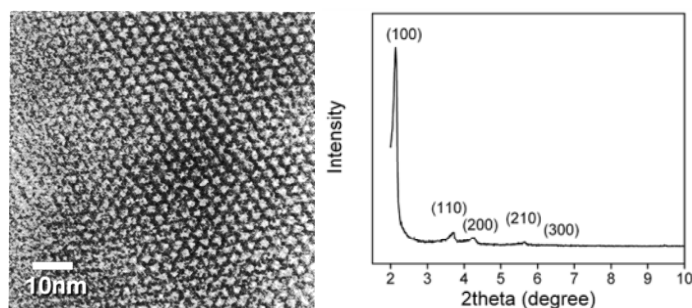


Figure 1-1 Typical TEM images of MCM-41 recorded along [001]¹⁷ direction and its low-angle PXRD pattern.

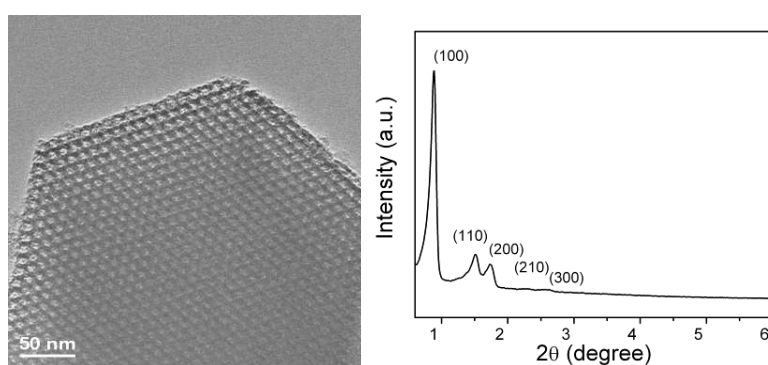


Figure 1-2 TEM images of SBA-15 recorded along [001] direction and the low-angle PXRD pattern of SBA-15.

Generally it is more difficult to prepare 3D ordered mesoporous silicas (such as MCM-48) than 2D mesopores (e.g., MCM-41 and SBA-15). The ionic surfactant directed cubic *Ia3d* MCM-48 is obtained under alkaline condition in a narrow composition range.²⁵ The block copolymer approach, along with other additives could be employed for the preparation of 3D (*Ia3d*) mesoporous silicas.^{26,27} A facile method of preparing a bi-continuous three-dimensional mesoporous silica (KIT-6) using a ternary triblock copolymer-butanol-water system was successfully developed, with a tunable pore size in the range of 4-12 nm.^{25,28} A typical TEM image and illustration of the pore structure of KIT-6 are shown in Figure 1-3. This material has thick walls (~ 4 nm), a large surface area (~ 800 m²/g), large pore size (~ 8 nm diameter) and a 3D bi-continuous pore

network. 3D mesostructures with large pores (more than 5 nm) and thick pore walls are believed to provide an open and highly accessible porosity for guest species, as well as good thermal stability. With these properties, mesoporous KIT-6 attracts increasing interest for potential application in catalysis, adsorption and separation, and as a nanohost for composite materials as well as a template for other mesoporous materials.^{29,30}

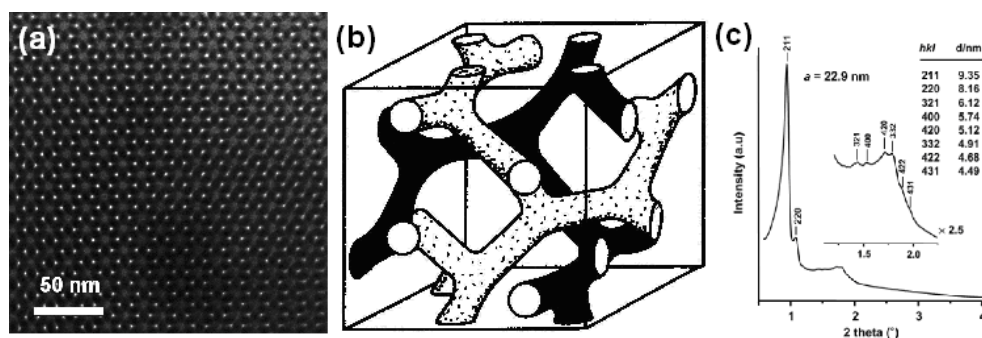


Figure 1-3 (a) TEM image for KIT-6 recorded along [111] direction; (b) a schematic diagram for KIT-6 pore structure; (c) XRD pattern of KIT-6.²⁸

Although many methods have been developed to prepare silica mesostructures, it is still not easy to apply these methods to the preparation of non-silica mesoporous materials, such as mesoporous transition metal oxides, and metal chalcogenides.^{2,31,32} Among such non-silica mesoporous materials, mesoporous transition metal oxides are particularly important targets, because they possess d-shell electrons confined to nanosized walls, highly redox active internal surfaces, and a 3D connected pore network from a suitable template. With these attributes they exhibit many interesting properties in energy conversion and storage, catalysis, adsorption, separation, sensing, and magnetic devices.³²⁻³⁷

1.2 Soft-templated transitional metal oxides

The soft template method can be divided into two approaches-the ligand assisted method and the Evaporation Induced Self-Assembly (EISA) method.³⁸

Although mesoporous silicas can be modified by introduction of metal cations including transitional metal cations, the first synthesis of a true mesoporous transition metal oxide was reported by Ying et al. in 1995, using long chain alkylamines as

templates.³⁹ This ‘ligand-assisted’ method was also used to prepare mesoporous Nb₂O₅.^{9,37} These materials have an ordered pore structure but amorphous walls.

Following their work, many groups began to explore the synthesis, properties, and potential applications of mesoporous transition metal oxides especially using the EISA method and employing the commercial poly(alkylene oxide) block copolymers or other home-made copolymers as structure-directing agents in non-aqueous solution^{8,10,40,41}

Sanchez and coworkers used different *in situ* methods, e.g. *in situ* SAXS and WAXS and *in situ* FTIR, to investigate the mechanism of the EISA process (Fig. 1-4).¹⁰ They divided this process into three steps: **a**, Preparation of stable solutions containing the KLE3739 copolymer (PBH₇₉- *b*-PEO₈₉, PBH = hydrogenated poly(butadiene)) template) and the inorganic precursors at the proper stoichiometry; **b**, evaporation induced self-assembly associated with dip-coating. Evaporation induces the progressive concentration of inorganic precursors into a homogeneous flexible poorly condensed network surrounding the surfactant mesophase; **c**, Treatment step involving pre-consolidation, template removal and network crystallization. They demonstrated that the mesostructure was formed at the final step. In this way, multi-metal-oxide nano-crystalline films (e.g. SrTiO₃, MgTa₂O₆) could be obtained, bridging the gap between conventional mesoporous materials and the properties of crystalline ternary or quaternary metallic oxides.¹⁰

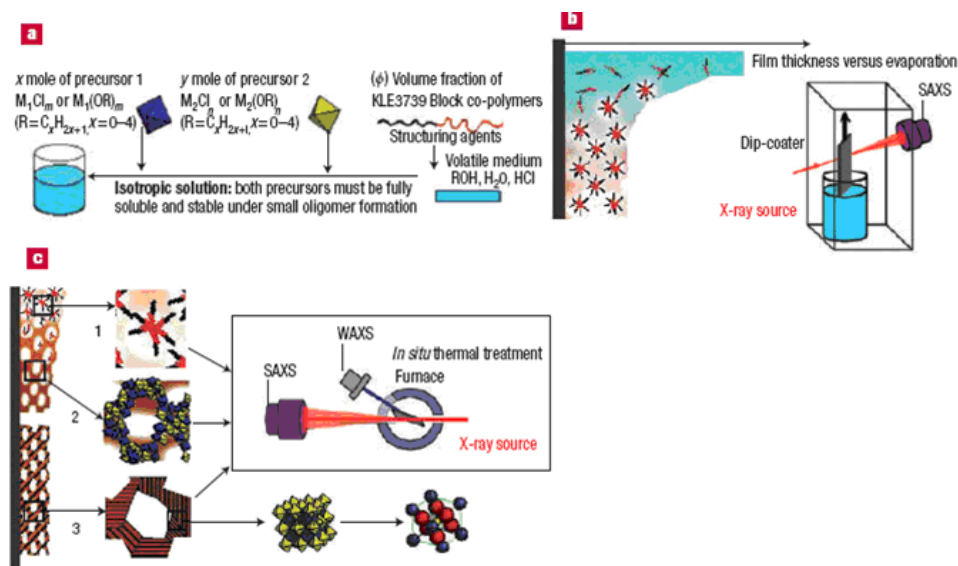


Figure 1-4 Scheme of the meso-crystallization process illustrating the three critical steps in detail.¹⁰

1.3 Ordered mesoporous metal oxides prepared by the hard template method

The concept of using a hard template to synthesize mesoporous materials has brought incredible possibilities for preparing novel mesostructured materials.¹⁴ The hard templating approach (also named as nanocasting), was originally designed using the porous anode oxidized Al_2O_3 membrane as hard template.⁴² Such porous Al_2O_3 membranes have been used to prepare metal, metal oxide, and metal sulfide nanostructures by electrodeposition or chemical vapor deposition (CVD).⁴³ The pore size of the materials formed using this method are usually larger than 20 nm with a relatively broad pore size distribution and poor pore structure regularity. Mesoporous silicate materials with highly ordered pore structures and uniform pore size are better hard templates. The hard template method using mesoporous silica was first introduced for the preparation of 3D mesoporous carbon, CMK-1, and mesoporous Pt networks using MCM-48 as the hard template.^{44,45} The schematic diagram representing the process is shown in Fig. 1-5. First the silica mesopores are infiltrated with a metallic salt precursor solution; the precursor is then converted to the dense material by for example, reduction or decomposition, to form the desired material inside the pores. Then the mesoporous silica template is removed using NaOH or HF solution and after washing, a material replicating the mesostructure of the hard template is obtained. Although the method was first developed to prepare mesoporous carbons,⁴⁵⁻⁴⁸ later it was also used as hard template for metal oxides.^{14,49,50} Such a method had been described as nanocasting,^{14,50} the hard template method,⁵⁰ exotemplating⁵¹, or repeated template method.¹³

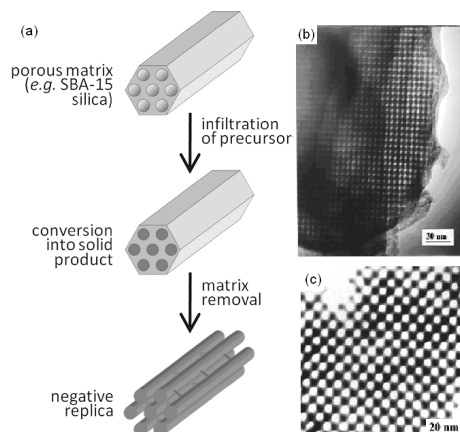


Figure 1-5 (a) Schematic diagram of hard template synthesis; TEM images of (b) mesoporous carbon CMK-1 and (c) Pt network using MCM-48 as the hard template.^{44,45}

Different mesoporous silicas or mesoporous carbons have been used as hard templates, such as MCM-48, SBA-15, KIT-6, SBA-16, FDU-12, and CMK-3, with or without surface modification. The first preparation of 3D highly crystalline porous transition metal oxides was reported in 2003, in which amine functionalized SBA-15 was used as the hard template.^{52,53} Mesoporous single crystalline Cr₂O₃ with highly ordered pores was obtained, consisting of nanowire arrays connected by short bridges (Fig. 1-6). Later, several other mesoporous metal oxides were prepared with a similar surface modification method, e.g. WO₃^{54,55} and α-Fe₂O₃.⁵⁶ Other surface functionalized hard templates have also been used, including for example, hydroxy rich^{30,53} or vinyl functionalized silica.⁵⁷

Highly ordered mesoporous metal oxides can also be prepared without surface functionalization using the dual-solvent, solvent evaporation, solid–liquid, or impregnation-precipitation-calcination methods.

For the dual-solvent method, a suspension of mesoporous silica in dry hexane is prepared followed by addition of a concentrated aqueous solution of metal nitrate (generally the solution volume is equal to the silica pore volume to maximize the impregnation quantity and prevent growth of metal oxides out of the pores).⁵⁸ The solvent evaporation method involves fully mixing mesoporous silica template with the selected metal nitrate in ethanol.⁵⁹ The nitrate precursor is expected to migrate into the pores by capillary action during the slow evaporation of ethanol. The solid–liquid method is a development of the evaporation method.⁶⁰ In this process, a metal nitrate is ground with a mesoporous silica template, and is expected to move into the pores of silica after melting when the mixed solid is heated to a temperature above the melting point of the precursor. The method is, of course, limited to the precursors that must have a melting point lower than the decomposition temperature. The impregnation-precipitation-calcination method is quite different from the above methods, employing low cost metal chlorides rather than nitrates as the starting materials. First, mesoporous silica is impregnated with metal chloride and dried, treated with NH₃ (gas or solution) to convert the chloride into hydroxide, and then calcined to the oxide. The impregnation-precipitation-calcination process is repeated twice more and after the removal of the silica template, the mesoporous metal oxide is obtained. That was first developed to prepare mesoporous

CeO₂, later applied to Co₃O₄, NiO, RuO₂ etc.^{61,62} Recently, a combustion method was developed for the preparation of mesoporous CuO.⁶³

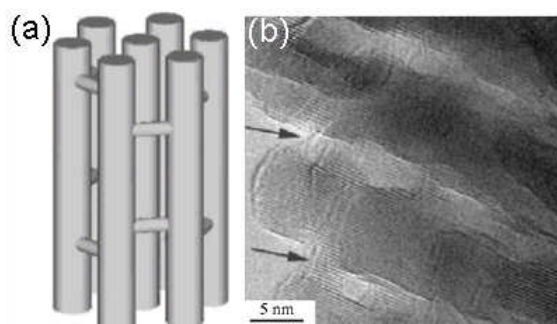


Figure 1-6 (a) Mesostructure model and (b) HRTEM image for mesoporous Cr₂O₃. The arrows indicate the small ‘bridges’ between the wires.⁵²

Using one or other of the above hard templating methods, a series of transitional metal oxides have now been prepared, including Cr₂O₃,^{52,58,60,63-65} CeO₂,^{60,61,63,66-71} NiO,^{30,55,60,63,70,72} In₂O₃,^{30,63,70,73-76} α-Fe₂O₃,^{56,63,77} γ-Fe₂O₃ and Fe₃O₄,⁷⁸ Co₃O₄,^{30,57,63,64,70,74,76,79-81} β-MnO₂,⁸²⁻⁸⁴ Mn₂O₃ and Mn₃O₄,^{63,85} Mn_xO_y,³⁰ WO₃,^{55,67,86-89} TiO₂,⁹⁰⁻⁹² etc.

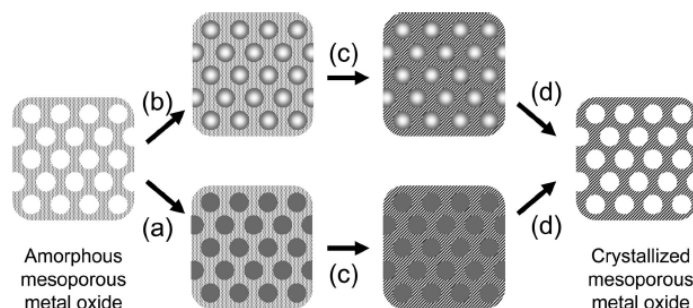


Figure 1-7 Schematic illustration of the strategy for reinforced crystallization of mesoporous metal oxides: (a) back filling, (b) coating, (c) crystallization, and (d) removal of the reinforcement.⁹³

One problem for ordered amorphous mesoporous metal oxide is the stability of the mesostructure during crystallization, thus a silica/carbon enforcement method was developed, which combines the advantages of the hard and soft template method. In this way highly crystalline ordered mesoporous Nb₂O₅, Ta₂O₅, (Ta, Nb)₂O₅, Al₂TiO₅, TiZr₂O₆, TiNb₂O₆ have been obtained.^{93,94} Recently Lee et al. prepared ordered

crystalline TiO_2 and Nb_2O_5 in a 'one-pot' synthesis using block copolymers with an sp^2 -hybridized carbon-containing hydrophobic block as the structure-directing agents, which converts to a sturdy, amorphous carbon material under appropriate heating conditions. This in-situ obtained carbon is sufficient to act as a rigid hard template keeping the pores of the oxides intact while crystallizing at temperatures as high as $1,000\text{ }^\circ\text{C}$.⁹⁵

The F. Schüth group in Germany and our group separately developed a post-synthesis solid-solid conversion method for the preparation of a series of transitional metal oxides and lithium metal oxide that are of mixed valence or valence that is not easily accessed directly from solution. Mesoporous Fe_3O_4 was the first mesoporous metal oxide with low valence (Fe^{2+}) to be synthesized; it was prepared from mesoporous $\alpha\text{-Fe}_2\text{O}_3$ by reduction in 5% H_2 (balanced with 95% argon) at $350\text{ }^\circ\text{C}$ for 1 h.⁷⁸ Mesoporous Mn_3O_4 was prepared by a similar procedure from mesoporous Mn_2O_3 in 5% H_2 (balanced with 95% argon) at $280\text{ }^\circ\text{C}$ for 3 h.^{63,85} Schüth and coworkers prepared ordered mesoporous CoO by the thermal treatment of mesoporous Co_3O_4 with hot glycerol as the reducing agent.⁹⁶ Recently we found that mesoporous CoO and Mn_3O_4 could also be obtained from mesoporous Co_3O_4 and MnO_2 using the 5% H_2 (balanced with 95% argon), respectively.

It demonstrated that post-synthesis reaction with lithium salts was successful to lithiate mesoporous transitional metal oxides for the first time. For example, mesoporous Mn_3O_4 or Co_3O_4 with LiOH to obtain ordered mesoporous Li-Mn-O spinel or LT-LiCoO_2 electrode materials.^{59,97} We have also prepared mesoporous $\text{LiNi}_{2/3}\text{Co}_{2/3}\text{Mn}_{2/3}\text{O}_4$ spinel. It is interesting to find that all lithium containing mesoporous metal oxides prepared to date adopt the spinel structure before and after the reaction with lithium salt (Co_3O_4 to LT-LiCoO_2 , Mn_3O_4 to Li-Mn-O spinel, NiCoMnO_4 spinel to $\text{LiNi}_{2/3}\text{Co}_{2/3}\text{Mn}_{2/3}\text{O}_4$ spinel).⁹⁸ The solid-solid conversion of rutile MnO_2 with LiOH leads to mesostructure collapsed LiMn_2O_4 .⁹⁹

The solid-solid conversion process involves a significant change of structure. For example, reduction of Mn_2O_3 (corundum structure) to Mn_3O_4 (spinel structure) involves a significant loss of oxygen and change of the O^{2-} stacking from hexagonal to cubic close packing. Such a transformation requires shearing of the AB planes (hcp) to the ABC stacking (ccp). The ability to do so while preserving the mesoporous structure

demonstrates that the thin walls (< 8 nm thick) can accommodate the strain of such a structural transformation without breakdown of the mesostructure. The loss of oxygen on solid-solid conversion results in decreasing the wall thickness while preserving the basic pore morphology, further demonstrating the flexible mesostructure in its accommodating strain from structural change.

Table 1-1 Structure transformation of the mesoporous metal oxide by solid-solid conversion

Start material	Structure	Final material	Structure	Reference
$\alpha\text{-Fe}_2\text{O}_3$	Hematite	Fe_3O_4	Spinel	78
Mn_2O_3	Corundum	Mn_3O_4	Spinel	85
Co_3O_4	Spinel	CoO	Cubic	96
Co_3O_4	Spinel	LT-LiCoO ₂	Spinel	59
Mn_3O_4	Spinel	LiMn ₂ O ₄	Spinel	97
NiCoMnO ₄	Spinel	LiNi _{2/3} Co _{2/3} Mn _{2/3} O ₄	Spinel	98
NiCoMnO _x	Spinel	Li _x Co _{1/3} Ni _{1/3} Mn _{1/3} O ₂	Spinel	100

1.4 Comparison of the soft and hard template methods

Materials prepared by soft template and hard template method have their advantages and disadvantages.

For soft-template method, the surfactants can be of low cost and the synthesis is easy compared to the hard template which has to be prepared. Also low temperature is often employed. However, the products resulting from the soft template method, just like the silica materials prepared by similar approaches, usually have amorphous or semi-crystalline walls and poor thermal stability, which greatly limits their applications.⁷⁷ Using specially designed polymer template such as KLE, crystalline metal oxides could be obtained, but all these syntheses are based on complicated sol-gel processes, the hydrolysis and polymerization of the transitional metal ions are difficult to control.^{10,101-}

104

The hard template procedure offers a number of advantages. The mesostructure of the target material may be controlled by selecting different templates, because many mesoporous silicas with different porous structures are already known and some are

already commercial available. With the hard template method, mesoporous metal oxides with highly crystalline walls may be obtained, leading to better properties for potential application in energy storage, catalysis, sensing, adsorption and separation.

However the hard template method also has its disadvantages. First, the mesoporous metal oxide materials must be stable to NaOH or HF solutions used to remove the silica template; although a mesoporous carbon be used instead. For example, the synthesis of pure mesoporous ZnO, MgO, Al₂O₃ has not been possible using mesoporous silica, while using mesoporous carbon CMK-3 as the template, such mesoporous metal oxides have been obtained.¹⁰⁵⁻¹⁰⁹ Second a solution step is still required as the means of introducing the transition metal precursor and this limits the range of materials to those stable in solution. Also, materials for which the precursors react with the mesoporous silica cannot be synthesized (e.g. lithium). While using mesoporous carbon as the hard template, one predominant disadvantage is the poor wetting of the pore walls by the aqueous precursor solution. To some extent, the post-synthesis reduction and post-synthesis solid-solid conversion enable preparation of low-valence metal oxides and lithium containing compound, greatly enriching the range of mesoporous materials and their applications.^{59,78,85,97}

Tiemman recently suggested the use of the term -‘repeated template method’ to describe the hard template synthesis of mesoporous metal oxides, because first soft template had been employed in the procedure (Fig. 1-8).¹³

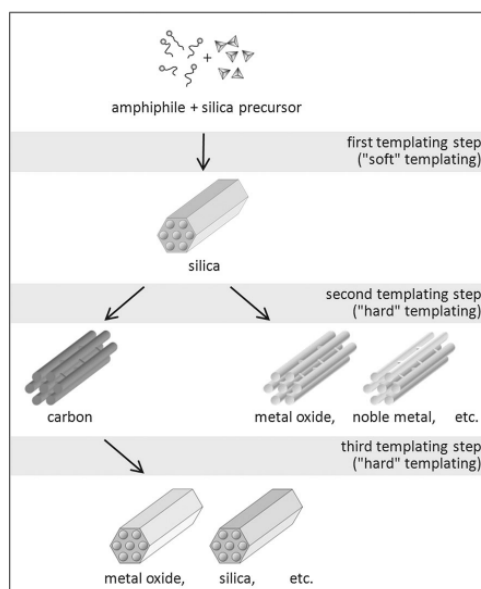


Figure 1-8 Schematic drawing of repeated templating for the synthesis of ordered mesoporous materials. The first step is “soft templating” (endotemplating), i.e., structure formation by utilization of amphiphilic structure directors; the following steps are “hard templating” (exotemplating).¹³

1.5 Applications of ordered mesoporous metal oxides

1.5.1 Energy conversion and storage

Up to now, a number of ordered mesoporous electrode materials have been reported, not limited to lithium metal oxides, i.e. mesoporous carbon CMK-3,¹¹⁰ SnO_x/CMK-3 composite,¹¹¹ LT-LiCoO₂,⁵⁹ Co₃O₄,⁸⁰ Fe₂O₃,¹¹² β-MnO₂,⁸²⁻⁸⁴ LiFePO₄,¹¹³ SnO₂,¹¹⁴ S/CMK-3,¹¹⁵ TiO₂,⁹⁰⁻⁹² and Li-Mn-O spinel.⁹⁷

Shortly after the preparation of mesoporous carbon CMK-3,²⁴ its electrochemistry performance was reported, which exhibited high specific capacity (850-1100 mAh/g) as an anode for rechargeable lithium batteries.¹¹⁰ Fan *et al.* used a SnO_x/CMK-3 nanocomposite as the negative electrode for a lithium battery.¹¹¹ Recently, mesoporous and nanowire SnO₂ anode materials for lithium batteries were prepared. The as-prepared SnO₂ nanowires had a diameter of 6 nm and a length of >3 μm and Brunauer–Emmett–Teller (BET) surface area of 80 m²/g, while mesoporous SnO₂ exhibits a pore size of 3.8 nm and a BET surface area of 160 m²/g. The charge capacities of these two anodes were similar to each other at 800 mAh/g, but mesoporous SnO₂ showed much improved cycle life performance and rate capabilities because of its higher surface area than nanowire SnO₂. The capacity retention of the mesoporous SnO₂ was 98%, compared with 31% for the SnO₂ nanowires at a 10 C rate (= 4000 mA/g). The improved electrochemical performance of the mesoporous SnO₂ was related to the regular porosity which permitted thorough flooding of the electrolyte between the particles, and the mesopores which acted as a buffer zone during the great volume contraction and expansion of Sn on cycling.¹¹⁴ Nazar’s group prepared a highly ordered interwoven composite structure composed of conductive mesoporous carbon CMK-3 framework constraining sulfur within the channels and generating good electrical contact to the insulating sulfur. The structure provides access to Li⁺ ingress/egress and reactivity with the sulfur, and it was speculated that the kinetic inhibition to diffusion within the framework and the sorption properties of

the carbon aid trapping of the polysulfides formed during the redox process, preventing them from transferring to the cathode and resulting in self-discharge. Reversible capacities up to 1320 mAh/g were obtained.¹¹⁵

The lithium in Li-ion batteries is confined in the cathode so the cathode materials normally need to be lithium transitional metal oxides. There have been very few studies of such ordered mesoporous solids because of the difficulty in synthesizing such materials (lithium will react with template silica). The first example of an ordered mesoporous lithium transition metal oxide, the low temperature polymorph of LiCoO_2 (spinel structure, not layered $R\bar{3}m$ structure), has been synthesized and shown to exhibit better properties as a cathode compared with the same compound in nanoparticulate form. The synthesis employed the hard templates (SBA-15 and KIT-6) to form a lithium free metal oxide Co_3O_4 then post synthesis reaction with lithium hydroxide to form LT- LiCoO_2 .⁵⁹ Crucially the ordered mesoporous structure is retained while converting Co_3O_4 to LT- LiCoO_2 . Lim et al. reported the preparation of nanowire LiFePO_4 cathodes using the hard templates SBA-15.¹¹³ Electrochemical cycling of the nanowire LiFePO_4 cathodes demonstrates excellent rate capability even above 10C rate, showing >89% capacity retention of the initial capacity, with a BET surface area of $45 \text{ m}^2/\text{g}$.

We have synthesized an ordered mesoporous $\text{Li}_{1.12}\text{Mn}_{1.88}\text{O}_4$ spinel and used it as the cathode in a Li-ion battery.⁹⁷ Recent interest has been focused on spinel with this composition because the oxidation state of Mn is higher than that in stoichiometric LiMn_2O_4 and the associated lower Mn^{3+} content reduces manganese dissolution. The mesoporous form exhibits better capacity retention than the bulk, 50% higher than the equivalent $\text{Li}_{1.12}\text{Mn}_{1.88}\text{O}_2$ bulk phase at a rate of 3000 mA g^{-1} (30C, fully charge or discharge in 2 min.), demonstrating the superior rate capability obtained by using a mesoporous spinel. Its volumetric energy density is 10% higher than the bulk despite the porosity. Remarkably, despite the high surface area ($90 \text{ m}^2\text{g}^{-1}$), the capacity retention at low rate (30 mA/g) and $50 \text{ }^\circ\text{C}$ is comparable to the bulk material and much better than the nanoparticle $\text{Li}_{1.12}\text{Mn}_{1.88}\text{O}_4$. Evidently the combination of nm and μm structures of the mesopores offer the advantages of both length scales. Luo et al. also reported mesoporous Li-Mn-O spinel as an electrode material, but only an irregular pore structure was obtained.⁹⁹

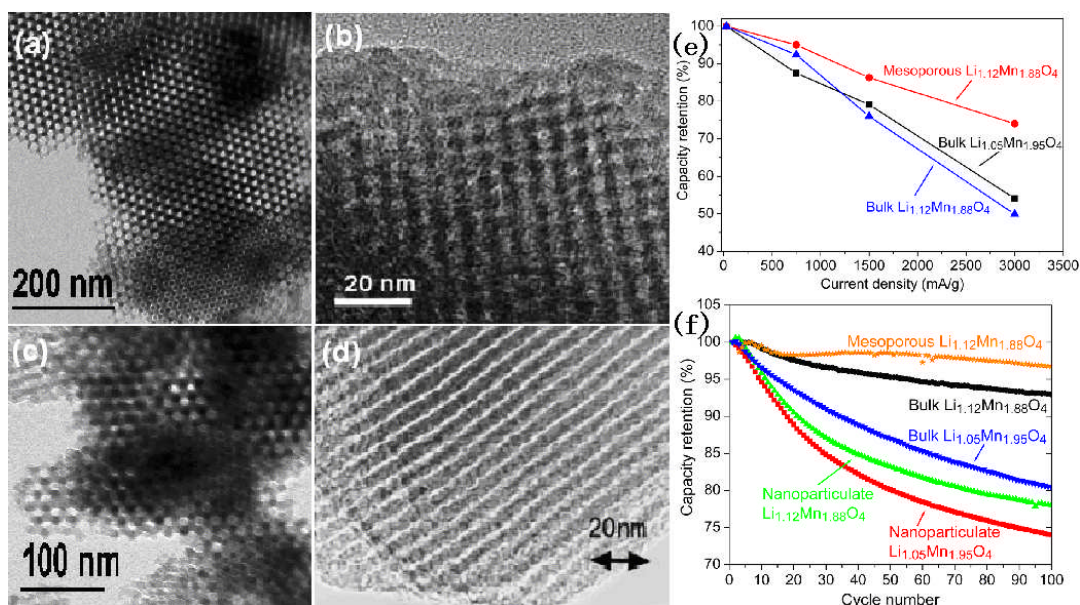


Figure 1-9 TEM images of mesoporous (a) β - MnO_2 ,⁸³ (b) SnO_2 ,¹¹⁴ (c) Li-Mn-O spinel,⁹⁷ (d) CMK-3.¹¹⁰ (e) Rate capability for mesoporous $\text{Li}_{1.12}\text{Mn}_{1.88}\text{O}_4$ (\bullet), bulk $\text{Li}_{1.05}\text{Mn}_{1.95}\text{O}_4$ (\blacksquare), and bulk $\text{Li}_{1.12}\text{Mn}_{1.88}\text{O}_4$ (\blacktriangle); capacity retention expressed as percentage capacity at 30 mA/g (0.30C); (f) Cycling data for mesoporous $\text{Li}_{1.12}\text{Mn}_{1.88}\text{O}_4$ (*), bulk $\text{Li}_{1.12}\text{Mn}_{1.88}\text{O}_4$ (\bullet), nanoparticulate $\text{Li}_{1.12}\text{Mn}_{1.88}\text{O}_4$ (\blacktriangle), bulk $\text{Li}_{1.05}\text{Mn}_{1.95}\text{O}_4$ (\blacktriangledown) and nanoparticulate $\text{Li}_{1.05}\text{Mn}_{1.95}\text{O}_4$ (\blacksquare), at 50 °C at 30 mA/g (0.30C) between 3–4.3 V.⁹⁷

Ordered mesoporous transitional metal oxides without Li have been used as anode materials. Examples are Co_3O_4 ,⁸⁰ β - MnO_2 ,⁸²⁻⁸⁴ Fe_2O_3 ,¹¹² TiO_2 rutile and anatase.⁹⁰⁻⁹² Our group⁸³ and Xia group⁸² reported the preparation of mesoporous β - MnO_2 using KIT-6 as the hard template at almost the same time. Bulk β - MnO_2 is electrochemically inert. However, mesoporous β - MnO_2 (rutile structure) with a highly ordered pore structure (3.4 nm) and highly crystalline walls (~ 7 nm) is capable of reversibly accommodating lithium, up to a composition of $\text{Li}_{0.92}\text{MnO}_2$ (equivalent to a charge storage of 284 mAh/g).⁸³ Remarkably, the crystal structure and the ordered mesostructure are preserved after many cycles (Li intercalation/deintercalation). Recently, the influence of mesoporous pore diameter and wall thickness on lithium intercalation rate has also been investigated.⁸⁴

Electrodes based on conversion reactions generally show a higher capacity than graphite (1000 mAh/g compared with 370 mAh/g) but suffer from a number of problems,

including low rate capability. Using mesoporous, nanoparticulate, and bulk Fe_2O_3 , the factors influencing the rate of the Fe_2O_3 conversion electrode were examined, demonstrating that electron transport to and within the particles is rate limiting.¹¹² A composite electrode based on mesoporous Fe_2O_3 can store 700 mAh/g at a rate of 3000 mA/g (or 6 mAh /cm² at 26 mA/cm²). More information about ordered mesoporous electrode materials can be obtained in the recent reviews and related references therein.^{6,116}

1.5.2 Catalysis

The synthesis of crystalline mesoporous transition metal oxides can deliver materials with highly ordered pore structures and highly crystalline walls, as well as good thermal stability.^{30,52,53,58,61,77} Despite the high internal surface area of mesoporous transitional metal oxides and the redox activity of their surfaces, investigation of ordered mesoporous metal oxides as catalysts has been limited, for instance, only a few isolated systems for CO oxidation were reported.^{68,117,118}

Hexagonal and cubic phases of manganese oxide mesoporous structures (MOMS) have been prepared by oxidation of $\text{Mn}(\text{OH})_2$.⁴⁰ The hexagonal MOMS materials form a hexagonal array of pores with an open porous structure and exceptional thermal stability (1000 °C). The walls of the mesopores are composed of nanocrystallites of dense phases of Mn_2O_3 and Mn_3O_4 , with MnO_6 octahedra as the primary building blocks. Catalytic oxidations of cyclohexane and n-hexane in aqueous solutions in a batch reactor show conversions of around 10% and 8%, respectively.

A series of CeO_2 based materials with different amounts of CuO have been prepared by wet impregnation.⁶⁸ CuO can be homogeneously loaded into the ceria replica. Compared with the porous CeO_2 prepared by direct decomposition of cerium nitrate hydrate, this CeO_2 shows high catalytic reactivity for CO oxidation, the T_{50} (temperature of 50% CO conversion) on this ceria replica is 83 K lower than on the decomposed ceria, and the CuO-loaded mesoporous ceria show even higher activity more active for this catalytic reaction, the lowest T_{50} is only 389 K, obtained by the 20% CuO loading. A simple synthesis for highly ordered mesoporous $\text{Ce}_{1-x}\text{Zr}_x\text{O}_2$ solid solutions with various Ce/Zr ratios has been achieved using EISA method.¹¹⁷ The Pt-loaded meso- $\text{Ce}_{0.5}\text{Zr}_{0.5}\text{O}_2$ catalyst is tested for CO oxidation and cyclohexene hydrogenation and exhibits high

catalytic activity, demonstrating that the as-prepared mesoporous $Ce_{1-x}Zr_xO_2$ have potential catalytic applications. Cubic ordered mesoporous Co_3O_4 , prepared via the nanocasting pathway using KIT-6 as hard template, was found to be an excellent catalyst for low temperature CO oxidation, with the activity clearly depending on surface area and pore systems of the catalysts. Recently, we prepared ten different ordered mesoporous metal oxides and tested for CO oxidation.⁶³ Among them, mesoporous Co_3O_4 , β - MnO_2 , and NiO show appreciable CO oxidation activity below 0 °C, and the catalytic activities of mesoporous β - MnO_2 , and NiO are even higher than those of their nanoparticulate counterparts with large surface areas. β - MnO_2 is particularly interesting because it combines low cost and low toxicity with high activity ($T_{50} = 39$ °C).

As in the description in Section 1-3, reinforcement (carbon or silica) could be utilized to strengthen the periodic structure of amorphous materials so that the original ordered mesoporous structure is preserved during thermal treatment for crystallization.⁴⁹ The reinforcement was removed after crystallization. Mesoporous Ta_2O_5 was prepared by the above reinforcement method and the enhancement of photocatalytic activity for the total decomposition of water was shown.

Roggenbuck *et al.* synthesized mesoporous CeO_2 using CMK-3 carbon as a hard template.⁶⁹ The obtained products exhibit uniform pores with a diameter of *ca.* 5 nm in a two-dimensional hexagonal periodic arrangement, as well as inter-particle porosity, broadly distributed around *ca.* 35 nm; the specific surface area is 148 m²/g. Catalytic tests reveal that the activity of the mesoporous products in methanol decomposition are substantially higher than for a non-porous sample. Mesoporous CeO_2 or MgO supported iron oxide nanoparticle for methanol decomposition was also investigated later.¹¹⁹ The summary of chemical reactions catalyzed by ordered crystalline mesoporous metal oxide was given in Table 1-2.

Table 1-2 Summary of different catalytic reaction using ordered mesoporous metal oxides as catalyst

No.	Catalytic reaction	Mesoporous catalyst	Ref
1	CO oxidation	CeO_2 , Co_3O_4 , Cr_2O_3 , CuO , Fe_2O_3 , β - MnO_2 , Mn_2O_3 , Mn_3O_4 , NiO , $NiCoMnO_4$	⁶³

		CuO-loaded mesoporous CeO ₂	68
		Ce _x Zr _{1-x} O ₂	117
2	Oxidations of cyclohexane and n-hexane	MnO _x	40
3	Cyclohexene hydrogenation	Pt/Ce _x Zr _{1-x} O ₂ , Ta ₂ O ₅	49, 117
4	Photocatalytic total oxidation of water pollutant	Ta ₂ O ₅	49
5	Methanol decomposition	CeO ₂ , Fe ₂ O ₃ /CeO ₂ , Fe ₂ O ₃ /MgO	69,119
6	Trace ethylene oxidation	Co ₃ O ₄ and Au/Co ₃ O ₄	120
7	Total Oxidation of Naphthalene	CeO ₂	121,122
8	NH ₃ oxidation to N ₂	CuO/RuO ₂	123

1.5.3 Gas sensing

Metal oxide semiconductor gas sensors supply good advantages with respect to other gas sensor devices because their operation is at elevated temperatures and in harsh environments, they are mechanically robust and relatively inexpensive and offer exquisite sensing capabilities.¹²⁴ Since the gas sensing includes the adsorption and catalytic reactions on a surface, the main parameter to tailor the sensitivity of a semiconductor sensor material is the surface area.¹²⁵ For this purpose, ordered mesoporous oxides have been synthesized for their potential applications as sensors (TiO₂, SnO₂, WO₃, ZnO).^{2, 6, 126} Hyodo etc. prepared a series of ordered TiO₂ and SnO₂ materials using surfactant or copolymer as the soft template with or without phosphoric acid treatment. Phosphoric acid (PA) treatment was found to be effective for improving the thermal stability of the ordered mesoporous structure.¹²⁷

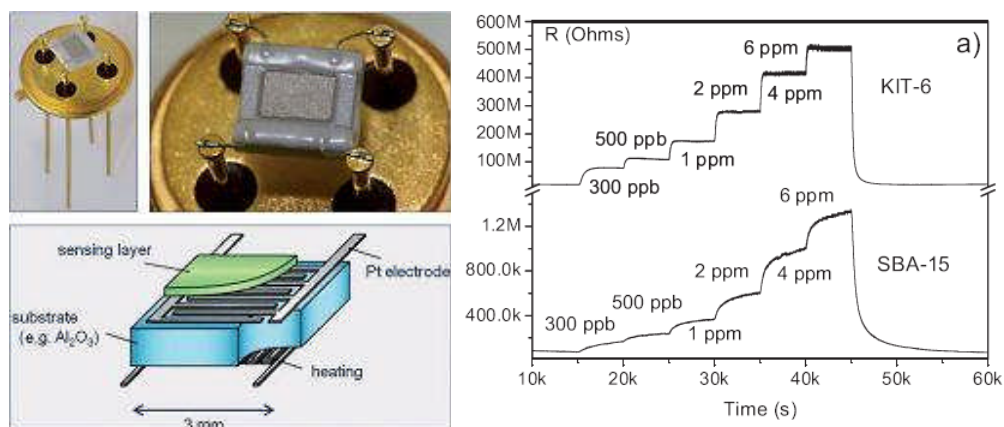


Figure 1-10 Left: photographs(top) and schematic drawing (bottom) of an example sensor substrate (UST Umweltsensortechnik GmbH, Germany);¹²⁵ right: dynamic response of pure SBA-15 and KIT-6 WO_3 replicas to different concentrations of NO_2 in synthetic air at $230\text{ }^\circ\text{C}$.⁸⁶

The H_2 sensitivity of the mesoporous SnO_2 sensor was superior to that of a conventional SnO_2 sensor.¹²⁸ It was found H_2 sensitivity of mesoporous SnO_2 was largely dependent on its specific surface area, the sensitivity being highest with the highest specific surface area.¹²⁹ With the same surface area, the larger pores are more sensitive than smaller pores. However, electrical resistance levels in air of the monolith sensors based on the mesoporous materials were close to the limit for practical measurement. The coating of mesoporous SnO_2 on common SnO_2 was effective for improving the gas-sensing properties, while maintaining the sensor resistance in air at a practical level. For example, NO_x sensitivity of conventional SnO_2 markedly increased with the coating, while H_2 sensitivity of the coated sensor was lower than that of mesoporous SnO_2 .¹²⁷

Rossinyol and his coworkers prepared mesoporous CeO_2 and WO_3 using hard template of SBA-15 and KIT-6.⁶⁷ Pure WO_3 replica from KIT-6 displays a higher response rate as well as a lower response time to NO_2 gas than the replica of SBA-15.⁸⁶ This behavior is explained by taking into account that the KIT-6 replica has a higher surface area and its mesostructure is fully maintained after the screen-printing step involved in sensors preparation. The presence of chromium in the material results in a shorter response time and improved sensor response to the lowest NO_2 concentrations tested. Recently they developed a mesoporous CaO -loaded In_2O_3 material (with $\text{Ca}/\text{In}_2\text{O}_3$

ratios ranging from 2.5 to 8.5 at %) and used it as a resistive gas sensor for the detection of CO₂.⁷³ In this process, first a mesoporous In₂O₃ matrix has been obtained by hard template route from the SBA-15 silica template. Additive presence does not distort the lattice of In₂O₃, which crystallizes in the Ia3d cubic space group. Pure In₂O₃ based sensors show low sensitivity to CO₂, whereas those containing the additive show an important response in the 300-5000 ppm range of gas concentrations. As seen by DRIFTS, the electrical response arises from the interaction between CO₃²⁻ and CO₂, yielding bicarbonates products. The reaction is water-assisted, so that hydration of the sensing material ensures sensor reliability whilst its dehydration would inhibit sensor response.

Tiemann group prepared mesoporous ZnO and Co₃O₄ for CO and NO₂ sensing,^{13,126} which exhibit promising gas-sensing performance: mesoporous Co₃O₄, synthesized by using mesoporous SBA-15 silica as the structure matrix turned out to be more sensitive to CO at lower operation temperature than a non-porous Co₃O₄ sample.

Highly ordered mesoporous niobium oxide films doped with cytochrome *c* were employed as a biosensor for the electrocatalysis of hydrogen peroxide, as cytochrome *c* adsorbed on an electrode surface displays a pseudoperoxidase activity due to the presence of cytochrome heme.¹³⁰ It is observed that the adsorbed protein molecules still retain their electrocatalytic activity and that the biosensor shows a 100% enhancement in sensitivity over the blank Nb₂O₅ electrode.

1.5.4 Adsorption and separation

Over the past decade crystalline microporous materials have continued to find new applications in their traditional areas of use, such as catalysis, separation and ion exchange. Following the discovery of ordered mesoporous materials, these solids have also been regarded as suitable for such applications, with several studies illustrating that they can serve as stationary phases in high performance liquid chromatography. Bio-molecule separations have also been attempted, the pore size and pore uniformity of mesoporous materials may make them suitable for macromolecule separations, which, if accomplished, should lead to commercial use. The encapsulation of enzymes and other proteins into ordered mesoporous inorganic host materials has attracted considerable

attention over the past few years.⁴ This research has demonstrated that bio-molecules immobilized in inorganic matrixes retain their functional characteristics to a large extent. However, there is very little reported on the application of adsorption and separation for mesoporous metal oxides materials. The fabrication of nano-crystals by the nanocasting technique could be useful for this application. Ferrihydrite which was successfully prepared by using silica gel as hard template is an excellent sorbent for the removal of heavy metals from waste streams.^{131,132} Our initial result found that mesoporous CuO is a good material for NO adsorption and delivery, while mesoporous α -MnO₂ is good at CO₂ adsorption, which is described in later chapters.

1.6 Target of this research

Realizing the limitation of the present methods placed on the range of mesoporous transition metal oxides that could be synthesized, new ways in which new mesoporous materials could be prepared that were not previously possible are required. This includes transition metal oxide mesopores in previously inaccessible oxidation states and the first examples of ordered mesoporous CuO, anatase and α -MnO₂ hard templating from KIT-6 through the fine controlling of the chemistry.

New electrode materials hold the key to future safer, cheaper, environmental-friendly, and higher power rechargeable lithium batteries, in order to mitigate CO₂ emissions and global warming. Mesoporous electrode materials offer a potentially excellent solution. Their micron size particles ensure better inter-particle contact than for nanoparticles, while the electrolyte can flood the pores providing a high contact area. The thin walls ensure rapid lithium intercalation/deintercalation. The detailed analysis of nanosize factors on lithium intercalation rate is important for the development of new generation lithium batteries for the electrical or hybrid vehicles.

In addition to their electrochemical properties, mesoporous materials (e.g. mesoporous transition metal oxides) have potentially unique catalytic, adsorption, sensing, and magnetic properties. With the aid of new simple and straight-forward synthesis methods, novel nanomaterials may be prepared and the investigation of their properties and new applications are possible.

Chapter 2 Routine characterization techniques

2.1 Powder X-ray diffraction technique (PXRD)

After the discovery of X-rays by Röntgen in 1895, and the principles of X-ray diffraction by Laue and the Bragg family in 1910s, it still took several decades for the commercialization of powder X-ray diffractometer. As shown in Figure 2-1, the specific plane spacing d between two planes (hkl) is related to the diffraction angle θ by the Bragg law: $n\lambda = 2d\sin\theta$, where d is the distance between adjacent planes of atoms, θ is the angle of incident X-ray beam, n is the order of the diffracted beam, λ is the wavelength of the X-ray beam.

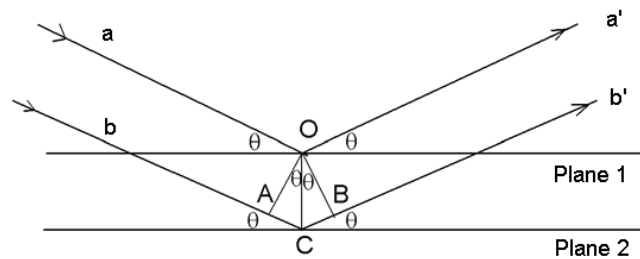


Figure 2-1 X-ray diffraction. Plane 1 and Plane 2 are lattice plane 1 and plane 2. O and C are the contact points for injection lights and lattice planes.

PXRD is widely used in many fields, e.g. phase identification, crystallinity, lattice parameters, expansion tensors, bulk modulus, phase transitions. The phase identification is the basic application of PXRD. The diffraction pattern is the fingerprint of any crystalline phase and powder diffraction has been extensively used to identify the mixture of useful materials. Phase identification is based on the comparison of the set of reflections of the sample with that of pure reference phases, or with a database. The Powder Diffraction File (PDF) distributed by the International Centre for Diffraction Data (ICDD) (formerly ASTM, then JCPDS), is the base most commonly used. Indexing of a powder pattern from the set of d spacing (i.e. the determination of the value of the h , k , and l regularly for each reflection line) can be difficult, particularly in the case of phases with crystal systems of low symmetry (e.g. triclinic). Nowadays, automatic programs using interactive methods and running on personal computers make the task

easy. In this thesis, all indexing based on PXRD data was carried out using the Stoe software.

There are many factors that determine the width of a diffraction peak. These factors include: instrumental factors, the presence of defects to the perfect lattice, differences in strain in different grains, and the size of the crystallites. To correlate the size of nanoparticle in a solid to the broadening of a peak in a diffraction pattern the Debye-Scherrer equation could be used,¹³³ $\tau = \frac{K\lambda}{\beta \cos \theta}$, in which τ is the average particle size, K is the shape factor, λ is the X-ray wavelength, typically 1.54 Å for $\text{Cu}\alpha$ and 1.936 Å for $\text{Fe}\alpha$, β is the line broadening at half the maximum intensity (FWHM) in radians, and θ is the Bragg angle. The dimensionless shape factor K has a typical value of about 0.9, but varies with the actual shape of the crystallite. The Debye-Scherrer equation is limited to nanosized particles (< 100 nm).



Figure 2-2 Stoe STADI/P powder diffractometer.

In the current thesis, wide-angle PXRD data were collected in a Stoe STADI/P powder diffractometer operating in transmission mode and with a low angle position sensitive detector. Incident radiation was generated using a $\text{FeK}\alpha_1$ source ($\lambda = 1.936 \text{ \AA}$). The patterns of CeO_2 , Cr_2O_3 , and TiO_2 were obtained on a Philips PW1710 in reflection geometry with $\text{Cu K}\alpha_1$ radiation ($\lambda = 1.541 \text{ \AA}$). While low-angle PXRD measurements were carried out using a Rigaku/MS, D/max-rB with $\text{Cu K}\alpha_1$ radiation ($\lambda = 1.541 \text{ \AA}$) operating in reflection mode and a scintillation detector (in Analysis and Characterization Center, Fudan University, Shanghai, China). For common samples, the PXRD measurements are carried out at room temperature under air; while for those air-sensitive

samples, the samples were sealed between two polymer films or in a micro-capillary (0.7 or 0.5 mm diameter) by using vacuum grease and all assembling work was carried out in an argon filled glove box. For nanomaterials (relative low crystalline), generally the step size is 0.1° (step time 100 s); for bulk materials, step size is 0.3° (step time 30 s).

2.2 *Ex situ* and *in situ* Raman spectroscopy

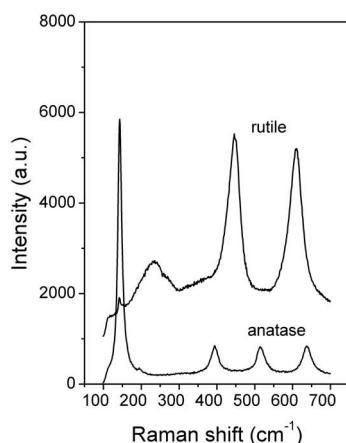


Figure 2-3 Typical Raman spectra of anatase and rutile.

When a monochromatic light was shed on a molecule, there will be different interaction between the inlet light and the molecule (its photons): infrared adsorption, Rayleigh scattering (elastically), and Raman scattering (inelastically) in which the scattered light has longer or shorter wavelength than the inlet light wavelength. So if the inlet light frequency is ν , the related scattered Raman signals will be $\nu \pm \Delta\nu$.

Although the Raman scattering of light was predicted in 1923, it was only observed in 1928 by C. V. Raman and this technology was named after his same. George Placzek developed early systematic theory in 1930s.

Raman combined with IR have long been used to distinguish the functional groups in organic compounds. It has also been used for identification purpose between different inorganic polymorphs and other crystalline structure information. Due to its high sensitivity, nondestructive, and surface enhanced characteristics, different new Raman technologies have been developed and employed in cutting edge research technologies, such as in-situ Raman spectroscopy,¹³⁴ Raman microscopy,¹³⁵ tip-enhanced Raman,¹³⁶

etc. In the current research work, we investigate *in situ* the anatase structure change (from tetragonal to orthorhombic) upon lithium intercalation directly.

The *in situ* Raman data were collected by a Renishaw InVia Raman inverted and upright microscope system (Renishaw, Wotton-under-Edge, UK), equipped with 50/0.5 long working distance objectives. A laser excitation wavelength of 632.8 nm was used, with a filter employed to reduce the laser power to 3mW at the electrode surface.⁹²

2.3 EXAFS

X-rays interact with a substance in these ways-diffraction, emission, and adsorption. For X-ray adsorption, the spectra were recorded especially near the adsorption edge. X-ray Absorption Spectroscopy (XAS) includes both Extended X-Ray Absorption Fine Structure (EXAFS) and X-ray Absorption Near Edge Structure (XANES). XAS is the measurement of the X-ray absorption coefficient of a material as a function of energy: $I_t = I_0 e^{-\mu x}$, here I_0 is X-ray intensity shone on the sample, I_t is X-rays intensity that are transmitted through sample, x is the thickness of the sample and μ is the X-ray absorption coefficient. When the input X-ray energy matches the binding energy of an electron of an atom within the sample, absorption increases dramatically, causing a drop of I_t -the absorption edge. However, when the input X-ray is energetic enough to excite one of the core electrons to form a photo-electron, it will be scattered by the near atoms. It is the interference between the outgoing electron and the back-scattered ones which leads to oscillations visible in the absorption spectrum above the edge, which can extend to up to 1000 eV past the edge. These oscillations are called the Extended X-ray absorption fine structure (EXAFS).

EXAFS spectra are displayed as graphs of the absorption coefficient of a given material versus energy, typically in a 500 – 1000 eV range beginning before an absorption edge of an element in the sample. The X-ray absorption coefficient is usually normalized to unit step height. While XANES examines the fine structure in the near edge region (oxidation state), EXAFS studies the variation of adsorption with energy over a much wide range. EXAFS is suitable for both crystalline and non crystalline materials because it could determine the local structure of each element and not the average signal of normal diffraction techniques. EXAFS can be used to probe the

coordination around the target atom, including the distances, coordination number and species of the atoms immediately surrounding the selected element.

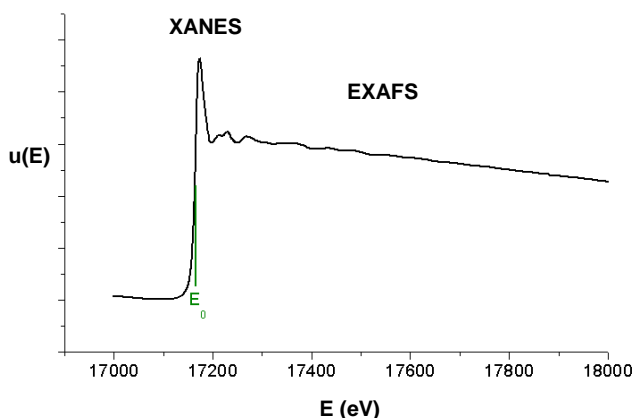


Figure 2-4 A typical XAS pattern

In the current thesis work, The XANES and EXAFS data were collected at the station 9.3 in CLRC Daresbury Synchrotron Radiation Source. This source has electron energy of 2 GeV and the average current for these measurements was ~150 mA. The data were collected in transmission mode and the beam current was measured using gas filled ion chamber detectors. The scan range was from ~100 eV below the absorption edge to several hundred eV beyond the edge.

2.4 Neutron diffraction

Neutron diffraction is an important technique. It can provide information on both the crystal and magnetic structure and is used for crystal structure determination and refinement

The scattering power between the neutron and X-ray is quite different. X-ray scattering amplitude is a function of the atomic number (extra-nuclear electron) because X-Rays are scattered by electrons, whereas neutrons are scattered by nucleus. So some light nuclei have strong scattering power, which result in one good point for neutron diffraction-sensitivity to light element-H, Li etc. So neutron diffraction is often employed in the structure determination of Li-containing compound.

In the current thesis work, samples for neutron diffraction (Li intercalated β - MnO_2) were prepared electrochemically at a rate of 10 mA/g. After the first discharge, cells were

transferred to an argon-filled glove box before opening and removing the active material. The electrodes were rinsed with a small amount of dry solvent (DMC) to remove residual electrolyte. They were then left under dynamic vacuum overnight to ensure all solvent had evaporated. The samples were then transferred to 2 mm quartz capillaries. The structures of the materials were characterized using neutron diffraction. Time-of-flight powder neutron diffraction data were collected on both the GEM and POLARIS instruments at ISIS, Rutherford Appleton Laboratory. The structures were refined by the Rietveld method using the program TOPAS.¹³⁷

2.5 Adsorption

According to IUPAC definition, adsorption (in the present context, positive adsorption at the gas/solid interface) is the enrichment of one or more components in an interfacial layer.¹⁵ Most materials in this thesis work are highly porous and possess large specific surface areas. The determination of surface area is generally considered to be an important requirement in solid materials characterization. In addition, it is usually necessary to specify the nature of the pore structure since this may control the transport of the species of a catalytic or electrochemical reaction process. Gas adsorption is most often used methodology to determine the surface area and pore size distribution of solids.

2.5.1 Isotherms and hysteresis types

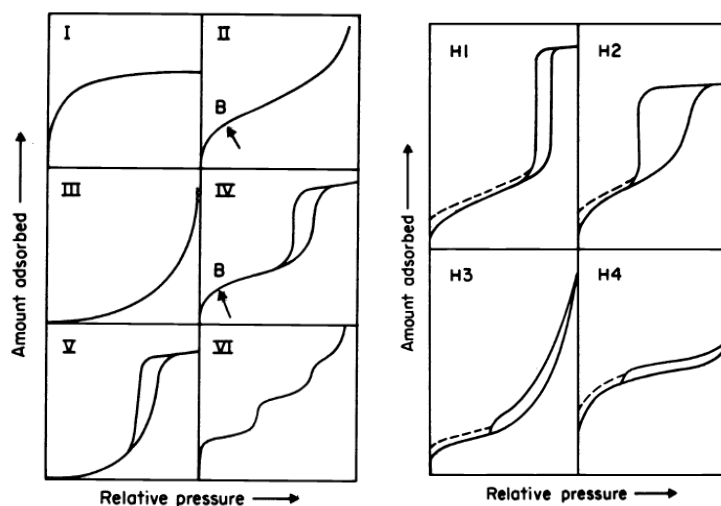


Figure 2-5 Type of physisorption isotherms (left) and hysteresis loops (right).¹⁵

Majority N₂ adsorption isotherms could be divided into six typical groups, which are shown in Fig. 2-5.¹⁵ Type I isotherms are usually given by microporous materials considered to be monolayer adsorption due to limited pore width (Langmuir adsorption). Adsorption on many macroporous solids proceeds via a multilayer formation result in that the amount adsorbed increases gradually as the relative pressure increases, although the multilayer buildup close to the saturation vapor pressure may be quite rapid. This unrestricted multilayer formation process gives rise to type II isotherms. Type IV has a characteristic hysteresis loop, associated with the capillary condensation in mesopores. Type III and V are uncommon. III appears in nitrogen adsorption on polypropylene. Type VI shows the stepwise multilayer adsorption on a non-porous surface.

Hysteresis loops in the multilayer range of nitrogen adsorption isotherms are related to different pore morphologies. Generally H1 is associated with porous materials consisting of approximately uniform spheres in fairly regular array, and narrow pore size distribution. For loop type H2, the pore size and shape is well defined. The loop type H3, is observed with slit-shaped pores. For type H4, it is associated with narrow slit-like pores.

2.5.2 Useful information from the adsorption analysis: Brunauer-Emmett-Teller (BET) surface area, pore size distribution, pore volume

Now the Brunauer-Emmett-Teller (BET) gas adsorption method has become the most widely used standard procedure for the determination of the surface area of a porous materials.¹³⁸ The BET equation can be expressed by the following function:

$$\frac{1}{v[(P_0/P)-1]} = \frac{1}{v_m c} \left(\frac{P}{P_0}\right) + \frac{1}{v_m}$$

In this function, P is the equilibrium pressure of nitrogen, P_0 is the saturation pressure of nitrogen at the adsorption temperature, v is the quantity of adsorbed nitrogen in the solid, c is the BET constant and v_m is the quantity of adsorbed nitrogen via monolayer mechanism. Because the linear relationship in this function only exists in the relative pressure (P/P_0) range from 0.05 to 0.25, the data for calculation of the surface area by BET method were chosen in this pressure range.

The t-Plot calculation allows quantitative analysis of the area and total volume ascribed to micropores. The commonly used practical method of extracting mesopore distribution from isotherm data is using Kelvin-based theories, such as the BJH method, combining pore size with a critical condensation pressure. The BJH pore size distribution was calculated considering both the change in adsorbate layer thickness and the liquid condensed in pore cores. BJH reports could be from both adsorption and desorption data.

For the current thesis work, nitrogen adsorption-desorption measurements were carried out by using different machines, including Hiden IGA porosimeter, Micromeritics ASAP 2020 and Tristar 3020. The typical sample weight used in the measurement was 10-20 mg for Hiden IGA and 0.1-0.2 g for other two Micromeritics machines. The degas conditions were normally set to 180 minutes at 120 °C under vacuum (10^{-3} - 10^{-5} Pa) and all adsorption-desorption measurements were carried out under liquid nitrogen temperature. For carbon dioxide adsorption, the α -MnO₂ was dehydrated at 150 °C for 180 min, the adsorption test was carried out under an ethanol-dry ice bath. For NO adsorption, the mesoporous metal oxides were degassed at 150 °C under vacuum (10^{-3} - 10^{-5} Pa) for 3 h. The adsorption and desorption was carried out at ambient temperature.



Figure 2-6 Micromeritics ASAP 2020, Tristar 3020, and Hiden IGA porosimeter.

2.6 Transmission electron microscopy

The Transmission Electron Microscopy (TEM) is a technique whereby a beam of electrons (like light for common light microscopy) passes through a thin sample, interacting with the sample as it passes through. An image is formed from the interaction of the transferred electrons with the sample; the image is magnified and focused onto an imaging capture device, such as a fluorescent screen, a layer of photographic film, or a CCD camera. Resolution and magnification of a microscope are related to the wavelength

and the energy of the radiation. The shorter the wavelength, the better the resolution. So TEM has higher resolution than common microscopy. The first TEM was built by Max Knoll and Ernst Ruska in 1931, with this group developing the first TEM with resolving power greater than that of light in 1933 and the first commercial TEM in 1939. A TEM is composed of several main components, including a vacuum system, an electron gun (generating electron beam), electromagnetic lenses, specimen stage, apertures, imaging system and appendix.

An electron diffraction unit and Energy dispersive X-ray spectroscopy (EDX or EDS) are usually attached to the TEM. When an electron beam is focused onto a small part of the sample (normal several to hundreds of nanometers by adjusting the spot size), an electron diffraction pattern can be obtained (Selected Area Electron Diffraction, SAED). From the diffraction pattern, the crystallinity of the specimen could be determined: for the image consisting of a pattern of dots in the case of a single crystal, or a series of rings in the case of a polycrystalline or amorphous solid material. Based on electron diffraction measurements for single crystalline sample, it is possible to carry out electron crystallography studies, which means solving the crystal structure of a very small single crystal using the diffracted electron beams in an electron microscope. By using a series of SAED patterns from different orientations taken on a selected particle in TEM and combining all reflections, an electron density map may be obtained and a three-dimensional model can be set up, as for mesostructure determination of mesoporous silica KIT-6.²⁹ Further refinements are required to determine the final structure of the sample. This technique is very useful if crystalline domain size is on a nano-scale which is too small for normal PXRD studies. This includes crystals which have a particularly short crystal dimension, such as nano-crystals, nanowire crystals, and porous materials with nano-scale crystalline walls. Further, as the crystallography is carried out in a TEM, in principle, crystallography may be performed on different parts of a sample which have different composition on a sub-micron scale.

EDS is an analytical technique used for the elemental analysis. As a type of spectroscopy, it relies on the investigation of a sample through interactions between electromagnetic radiation and matter, analyzing X-rays emitted by the matter in response to being hit with charged particles. Its characterization capabilities are due in large part to

the fundamental principle that each element has a unique atomic structure allowing x-rays that are characteristic of an element's atomic structure to be identified uniquely from each other. However, it has its disadvantage, including relative low accuracy and the fact it can not detect light elements, such as H, He, Li etc.

TEM studies discussed in the following chapters were carried out by using a JEOL JEM-2011 (Fig. 2-7). This TEM uses a LaB₆ filament as the electron source and the accelerating voltage is 200 kV. TEM and HRTEM images, SAED patterns were all recorded by a Gatan CCD camera in a digital format. The SAED patterns could also be recorded on traditional films followed by developing in a dark room and transforming into a digital form by scanning. The camera length for recording SAED patterns was set to 80 cm and the exposing time was varied depending on the brightness of the diffraction spots. An energy dispersive X-ray analysis (EDXA) system was attached to this TEM, which was used to identifying the elemental composition of the sample.

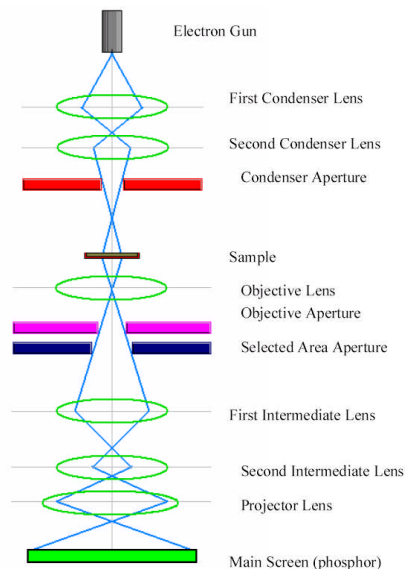


Figure 2-7 JEOL JEM 2011 and its structure illustration¹³⁹

2.7 Magnetic properties by Superconducting quantum interference devices (SQUID)

Superconducting quantum interference devices (SQUID) are used to measure very small magnetic fields with extremely high sensitivity. Based on the discovery of the Josephson Effect in 1962, the first dc SQUID was introduced in 1964 Ford Research Labs. Because of the extremely high sensitivity to the weak magnetic field, SQUID have

been used to study many topics, such as magnetic properties of materials, biological phenomena and in the geographical field.

The device used to measure the magnetic properties in the current thesis studies is a Quantum Design SQUID magnetometer, which is located in University of Edinburgh. Magnetization dependence with temperature measurements were performed on polycrystalline samples of mesoporous and bulk α -MnO₂ with a MPMS[®] Quantum Design SQUID magnetometer. The samples were encapsulated in eicosane (C₂₀H₄₂, melting point 310 K) in gelatin capsules to prevent grain re-orientation in strong magnetic fields, and finally held in the measurement chamber in a diamagnetic straw. Zero field and field cooled measurements (zfc and fc) were taken from 2-300 K, with an applied measurement field of 100 Oe (1 Oe = 10³/4 π A m⁻¹) and 1000 Oe (mesoporous sample only).

2.8 Thermogravimetry (TG)

Thermal analysis involves the measurement of certain physical and chemical properties as a function of temperature. Those could be heat capacity, mass, enthalpy etc. Thermal analysis can be used for detecting the materials' decomposition, phase change, glass change temperature, phase diagram etc. Thermogravimetry (TG) measures the change in mass of a solid material as a function of temperature or time. The result is a continuous record as illustrated in Fig. 2-8. The materials is heated at a constant rate (generally 5-10 °C/min) and has a constant mass of M_i until it starts to decompose at a certain temperature of T_i. Since in TG, the heating is dynamic, the decomposition process often lasts for a certain temperature range, from T_i to T_{ii}; then a new plateau appears after T_{ii} and the new constant mass is M_{ii}. The mass change of ΔM is the principal property of the material and could be used for quantitative calculation of the composition change, possible reaction process etc. The temperature value of T_i and T_{ii} can be greatly influenced by the reaction atmosphere, particle size and heating rate. In this thesis, the TG analysis was used to determine the water composition in α -MnO₂ mesostructure. The analysis was performed on Rheometrics TG 1000M with a heating rate of 10 °C/min under Argon from room temperature to 600 °C.

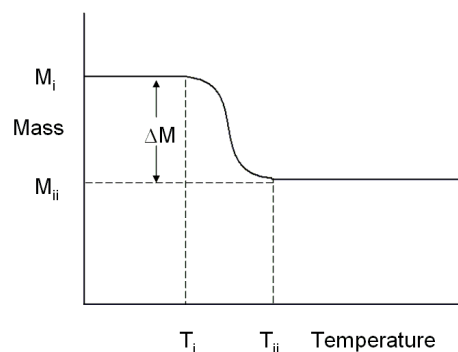


Figure 2-8 Schematic TG curve for a single step decomposition reaction



Figure 2-9 Photo of TG (Rheometrics TG 1000M), glovebox (MBraun), and MACCOR 4200 system.

2.9 Catalytic CO oxidation test

Catalytic CO oxidation was tested in a plug-flow microreactor (Altamira AMI 200). 50 mg of catalyst was loaded into a U-shaped quartz tube (4 mm i.d.). After the catalyst was pretreated in flowing 8% O₂ (balanced with He) at 200 or 400 °C for 1 h, the catalyst was then cooled down, the gas stream switched to 1% CO (balanced with air) and the reaction temperature ramped using a furnace (at a rate of 1 °C/min above ambient temperature) or by immersing the U-shaped tube in ice-water or acetone-liquid N₂ mixture to record the light-off curve. The flow rate of the reactant stream was 37 cm³/min, and the space velocity was 44400 cm³/(h·gcat.). A portion of the product stream was extracted periodically with an automatic sampling valve and analyzed using a dual-column gas chromatograph with a thermal conductivity detector.

2.10 Electrochemistry measurements

Coin type cells were used in the electrochemical tests carried out in this thesis. Coin cells are a convenient means of making many cells quickly and inexpensively. They are more akin to the commercially available cells. The coin cell kits were supplied by the National Research Council, Canada (NRC) (25 mm in diameter by 2.5 mm in height), an exploded view can be seen in Fig. 2-10. All cell parts are dried before use. A typical assembling of a coin type cell is described as following: first the dried sample is mixed with Kynar 2801 (a co-polymer based on polyvinylidene fluoride), and Super S (MMM) carbon in a selected weight ratio, e.g. 70:15:15. Acetone (Aldrich, > 99%) is usually used to disperse this mixture because under mild temperature the Kynar 2801 could be fully dissolved in it. Then about 50 μm thick film is cast onto an Al (purity 99.5%, thickness 0.050 mm, Advent Research Materials, Ltd.) or Cu (purity 99.95+%, temper hard, oxygen free high conductivity, thickness 0.050 mm Advent Research Materials Ltd) foil using a Doctor-Blade technique. After solvent evaporation at room temperature, the foil is cut into small discs (13 mm in diameter) and dried in a vacuum oven at 80 °C for 8-12 h. After drying under vacuum, the sample discs are transported into an Ar filled MBraun glovebox for the assembling ($\text{H}_2\text{O} < 0.1$ ppm; $\text{O}_2 < 0.1$ ppm). An active material coated disc is first placed on a coin cell bottom part with coated side facing upward, and then two pieces of separator are placed on the sample disc followed by adding 8-10 droplets of electrolyte LP30 (Merck; 1M LiPF_6 in 1:1 v/v ethylene carbonate : dimethyl carbonate). A small piece of lithium metal (cast from lithium ribbon, 99.9%, Aldrich), a steel disc, a spring and a coin cell top part with a plastic sealing ring are placed on the top following this order. Finally the cell is sealed by using a coin cell pressure system.

A MACCOR 4200 is used to collect the electrochemistry data. All tests were carried out at 30 °C in an oven unless is specified. For the characterization of electrode materials after cycling by other techniques, such as PXRD, TEM or neutron diffraction analysis, the powder of active material was recovered from the cell followed by washing with dimethyl carbonate (DMC) several times and drying under dynamic vacuum without exposure to air.

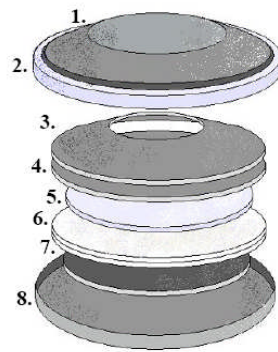


Figure 2-10 Exploded view of coin cell. 1. Lid 2. Cell sealing grommet. 3. Spring. 4. Spacer. 5. Lithium metal anode. 6. Glass fiber separators (Fisher) separator soaked in electrolyte LP30. 7. Composite cathode disc based on Cu or Al plate. 8. Base.¹³⁹

Chapter 3 Routine materials preparation

3.1 KIT-6 at different hydrothermal temperatures

The mesoporous silica, KIT-6, was synthesized using different hydrothermal treatment temperatures (45, 60, 80, 100, and 120 °C) following the procedure described in previous reports.^{25,28} 10 g of the copolymer P123 surfactant was mixed with 349.4 mL of distilled water and 16 ml of concentrated HCl (36%). After stirring the mixture at 35 °C until homogeneous, 10 g of n-butanol (99.4%) was added, stirred for one hour and then combined with 21.5 g of tetraethyl orthosilicate (98%). After stirring at 35 °C for 24 h, the mixture was heated in an autoclave at 45, 60, 80, 100, or 120 °C for a further 24 h. The precipitate was filtered, dried at 60 °C, then added to 300-400 mL of ethanol and 20-30 mL of concentrated HCl (36%). Following 1-2 h stirring, the mixture was filtered, washed several times with ethanol and water then dried at 60 °C. The resulting mesoporous solid was calcined at 500 °C for 3 h in air. The samples were denoted as KIT-45, KIT-60, KIT-80, KIT-100, and KIT-120 respectively according to their hydrothermal treatment temperatures. If not specified, the following mesoporous metal oxides are all prepared using the KIT-100 as the hard template.

3.2 KIT-6 at different calcination temperatures

Synthesis of the mesoporous silica KIT-6 was based on the procedure described previously.^{25,28} A typical synthesis procedure was described in Section 3.1 with the only difference being the calcination step. The resulting mesoporous solid was heated at a rate of 3 °C/min, and then calcined at various temperatures for 3 h to remove the copolymer template and tailor the pore size. The mesoporous silicas with different pore size prepared here are denoted KIT-X where X corresponds to the calcination temperature. (500 -1000 °C).

3.3 Disordered mesoporous silica with *ca.* 8 nm pore

The preparation of disordered mesoporous silica with a pore diameter of *ca.* 8 nm was similar to the procedure for KIT-100, except that a different mole ratio of the reactants was used (0.017 P123/2.6 TEOS/2.6 BuOH/1.83 HCl/195 H₂O), such that the composition was located in the disordered region of the phase diagram.²⁵ 10 g of the copolymer P123 surfactant was mixed with 349.4 mL of distilled water and 16 mL of

concentrated HCl (36%). After stirring the mixture at 35 °C until homogeneous, 20 g n-butanol (99.4%) was added, stirred for one hour and then combined with 55.9 g of tetraethyl orthosilicate (98%). Following stirring at 35 °C for 24 h, the mixture was heated in an autoclave at 100 °C for a further 24 h. The resulting mixture was filtered, dried at 60 °C, then added to 300-400 mL of ethanol and 20-30 mL of concentrated HCl (36%). After 1-2 h stirring, the mixture was filtered, washed several times with ethanol and water then dried at 60 °C. Following this procedure the resulting mesoporous solid was calcined at 500 °C for 3 h in air.

3.4 Two-step impregnation method for mesoporous Co_3O_4

$\text{Co}(\text{NO}_3)_2 \cdot 6\text{H}_2\text{O}$ (98%, Aldrich; 1 g) was dissolved in ethanol (20 mL) then mesoporous silica KIT-100 (2 g) was added. After stirring at room temperature until all the solution had been absorbed, the sample was heated slowly to 300 °C and calcined at that temperature for 3 h. The impregnation procedure was repeated, and the sample was then calcined at 500 °C for 3 h. The resulting sample was treated twice with a 10% solution of HF in water to remove the silica template, then washed with water and ethanol several times, and then dried at 60 °C.

3.5 One-step ethanol evaporation method for mesoporous CeO_2 , $\alpha\text{-Fe}_2\text{O}_3$, and NiCoMnO_4

1.5 g of $\text{Fe}(\text{NO}_3)_3 \cdot 9\text{H}_2\text{O}$ or $\text{Ce}(\text{NO}_3)_3 \cdot 6\text{H}_2\text{O}$ were dissolved in 20 mL of ethanol followed by the addition of 1 g of KIT-100. After stirring the mixture at room temperature until a nearly dry powder was obtained, the sample was heated slowly to 500 °C at a heating rate of 1 °C/min and kept at 500 °C for 6 h. The resulting sample was treated three times with a hot solution of 2 M NaOH, centrifuged, washed several times with water and ethanol, and then dried at 60 °C in an oven.

The synthesis of mesoporous NiCoMnO_4 is similar to that of crystalline mesoporous $\alpha\text{-Fe}_2\text{O}_3$.⁷⁷ 1.5 g of an equi-molar mixture of Ni, Co and Mn nitrates was dissolved in 20 mL of ethanol followed by the addition of 1 g of mesoporous silica KIT-100. After stirring the mixture at room temperature until a nearly dry powder was obtained, the sample was heated slowly to 800 °C at a heating rate of 1 °C/min in air, and kept at that temperature for 5 h. The resulting sample was treated three times with a hot solution of 2

M NaOH to remove the silica template, centrifuged, washed several times with water and ethanol, and then dried at 60 °C.

3.6 Synthesis of mesoporous Cr₂O₃, β-MnO₂, Mn₂O₃, and NiO by the ‘two-solvent’ method

Here the synthesis of mesoporous β-MnO₂ is shown as an example.⁸³ 30 g of Mn(NO₃)₂·6H₂O was dissolved in 20 mL of water to form a saturated solution. 5 g of KIT-100 was dispersed in 200 mL of dried *n*-hexane. After stirring at room temperature for 3 h, 5 mL of the saturated Mn(NO₃)₂ solution was added slowly with stirring. The mixture was stirred overnight, filtered and dried at room temperature until a completely dried powder was obtained. The sample was heated to 400 °C at a heating rate of 1 °C/min., calcined at that temperature for 3 h, and the resulting material treated twice with a hot solution of 2 M NaOH, followed by washing with water several times and drying at 60 °C. The only difference in the procedure for the other three metal oxides is the calcination conditions, Cr₂O₃: 500 °C for 3 h; Mn₂O₃: 600 °C for 3 h; NiO: 500 °C for 3 h. When preparing mesoporous β-MnO₂ with KIT-60, KIT-80, KIT-120 and the disordered ~ 8 nm mesoporous silica, the whole process is the same. When preparing mesoporous β-MnO₂ with KIT-45, only 3.5 mL of the saturated Mn(NO₃)₂ solution was used for impregnation.

3.7 Preparation of the other mesoporous β-MnO₂

The preparation of ordered mesoporous β-MnO₂ with a relatively high proportion of large pores (denoted as β-MnO₂-100B) followed a previously reported procedure.⁷² 4 g of Mn(NO₃)₂·6H₂O (98%) was dissolved in 150 mL of ethanol, followed by addition of 5 g of mesoporous silica, KIT-100. After stirring at room temperature until all the solution had been absorbed, the powder was re-dispersed in 100 mL of dry *n*-hexane under stirring in an open beaker. Once all the solvent had evaporated, the sample was heated slowly to 400 °C at a rate of 1 °C/min and calcined at that temperature for 3 h. After cooling to room temperature, the resulting sample was treated twice with a hot aqueous solution of 2 M NaOH to remove the silica template, followed by washing with water several times and then drying at 60 °C.

The preparation of disordered mesoporous β-MnO₂ with a pore diameter of ca. 30 nm was as follows: 100 g of Ludox AS-40 colloid silica (40%) was first dried at 60 °C

overnight, then impregnated with 10 mL of saturated $\text{Mn}(\text{NO}_3)_2$ solution and again dried. Following this procedure it was calcined at 400 °C for 3 h. Finally the resulting material was treated twice with a 2 M hot NaOH solution, followed by washing with water several times and drying at 60 °C.

3.8 Nitrate combustion method for mesoporous CuO

Mesoporous CuO was prepared by a nitrate combustion method.⁹⁸ 2.0 g of $\text{Cu}(\text{NO}_3)_2 \cdot 2.5\text{H}_2\text{O}$ was dissolved in 2.0 g of distilled water, and 1.0 g of KIT-100 was added. After drying at 100 °C for 1 h, the copper precursor-silica composite was exposed to the vapor from an aqueous ammonia solution at room temperature for 1 h and dried at 100 °C for 1 h. This impregnation-ammoniation-drying process was repeated twice more with aqueous solutions of 1.5 and 1.0 g $\text{Cu}(\text{NO}_3)_2 \cdot 2.5\text{H}_2\text{O}$, respectively. The resulting copper precursor-silica nano-composite was calcined at 400 °C for 6 h with a heating rate of 1 °C/min to obtain the CuO/silica nanostructure. (Caution: this reaction method involves rigid combustion taking place below 200 °C. A large open crucible should be used.) Finally, mesoporous CuO was obtained by treating the CuO-silica composite several times with a hot solution of 0.1 M NaOH, followed by washing with distilled water three times and absolute ethanol twice then drying at 60 °C for 2 h.

3.9 Dual template preparation of mesoporous manganese $\alpha\text{-MnO}_2$

In a typical synthesis of mesoporous $\alpha\text{-MnO}_2$, 7.53 g of $\text{Mn}(\text{NO}_3)_2 \cdot 4\text{H}_2\text{O}$ (98%, Aldrich) and 1.01 g KNO_3 was dissolved in ~ 10 mL of water to form a KNO_3 and $\text{Mn}(\text{NO}_3)_2$ mixture solution with molar ratio of $\text{Mn}/\text{K} = 3.0$. 5 g of mesoporous KIT-100 was dispersed in 200 mL of dried n-hexane. After stirring at room temperature for 3 h, 5 mL of mixture solution was added slowly with stirring. The mixture was stirred overnight, filtered and dried at room temperature until a completely dried powder was obtained. The sample was heated slowly to 500 °C, calcined at that temperature for 5 h and the resulting material treated twice with a 2 M hot KOH solution in water, to remove the silica template, followed by washed with water several times, and then drying at 60 °C.

3.10 Post-synthesis reduction for mesoporous Mn_3O_4 and Cu-Cu₂O

Mesoporous Mn_3O_4 was obtained by reduction of mesoporous Mn_2O_3 at 280 °C for 3 h under 5% H_2 / 95% Ar. Mesoporous Cu-Cu₂O was obtained by reduction of mesoporous CuO at 180 °C for 3 h under 5% H_2 / 95% Ar.

3.11 Preparation of mesoporous anatase

A typical synthesis of mesoporous anatase TiO_2 is as follows: 10 g of titanium oxysulfate (Aldrich, $\text{Ti} \geq 29\%$, free $\text{H}_2\text{SO}_4 \leq 17\%$) was dissolved in 50 mL of deionised water. Then the solution was added dropwisely to 500 mL of 1 mol/L $\text{NH}_3\cdot\text{H}_2\text{O}$ (Aldrich) solution with stirring and a white TiO_2 precipitate formed. After stirring for 24 h, the mixture was filtered and washed with distilled water. Then the fresh precipitate was dissolved in the 15 mL of nitric acid (Aldrich, 70%). Mesoporous KIT-100 silica was impregnated with an aqueous solution of $\text{TiO}(\text{NO}_3)_2$ (*ca.* 2.5 g solution per g KIT-100) using the incipient-wetness method, dried at 60 °C overnight and calcined at 400 °C for 5 h. The resulting material was treated twice with a hot NaOH solution (2 mol/L) to remove the template, followed by washing with water three times and drying at 60 °C for 6 h.

Chapter 4 Tailoring the pore size/wall thickness of mesoporous transition metal oxides- mesoporous Co_3O_4

The mesoporous silicas with different pore size here are tailored by variation of the calcination temperatures (silica denoted KIT-X where X corresponds to calcination temperature). The preparation of mesoporous Co_3O_4 followed the procedure described in Section 3.4. The resulting mesoporous Co_3O_4 replicas are denoted as $\text{Co}_3\text{O}_4\text{-X}$, where X corresponds to calcination temperature of the silica template.

4.1 KIT-6 templates

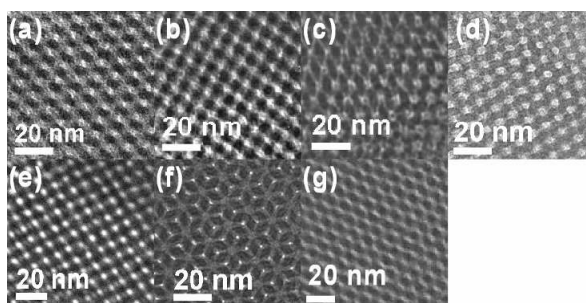


Figure 4-1 TEM images of mesoporous KIT silica calcined at (a) 500 °C, (b) 600 °C, (c) 700 °C, (d) 800 °C, (e) 900 °C, (f) 950 °C, and (g) 1000 °C.

TEM data for the KIT mesoporous silicas calcined at temperatures from 500 °C to 1000 °C are presented in Fig. 4-1. In each case many regions of the sample were examined and the TEM's presented in Fig. 4-1 are representative of the materials as a whole. It is evident that the ordered gyroidal $Ia3d$ mesostructure of the KIT silica is preserved at all calcination temperatures.

Low angle PXRD data for the KIT mesoporous silica calcined at different temperatures are shown in Fig. 4-2. The peaks shift to higher 2θ values with increasing calcination temperature, consistent with shrinkage of the mesostructure. There is evidence of increasing peak broadening and reduction in peak intensity with increasing calcination temperature, indicative of some reduction in the ordering of the pores. However as is evident in the TEM images (Fig. 4-1), ordering is still high even when calcined at 1000 °C. The a_0 lattice parameters for the KIT mesostructure extracted from the PXRD data are listed in Table 4-1 along with the corresponding values extracted from the TEM data. They are in good agreement, both showing a

reduction in lattice parameter with increasing calcination temperature. It is noteworthy that the KIT-1000 mesopore remains ordered even though the lattice parameter has contracted by 36% compared with the value for KIT-500.

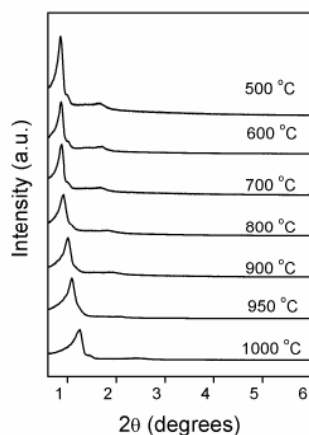


Figure 4-2 Low-angle X-ray diffraction patterns of the KIT mesoporous silica calcined at different temperatures.

The pore size and pore size distribution of the mesoporous silica were investigated in more detail using N_2 -sorption measurements. The absorption-desorption isotherms for each mesoporous silica are shown in Fig. 4-3a. They correspond to a type IV isotherm with a H1 hysteresis loop that reduces in size and shifts progressively to lower P/P_0 at higher calcination temperatures, consistent with reduction in the pore size.¹⁵ Such pore size reduction is shown clearly in Fig. 4-3b and Table 4-1 where the pore diameter is seen to reduce from 8.1 nm for KIT-500 to 2.4 nm for KIT-1000, i.e. the latter is approaching microporous dimensions, consistent with the changes in the absorption-desorption isotherm in Fig. 4-3a for this material. The pore size distribution varies somewhat with calcination temperatures (Fig. 4-3b). The distribution becomes narrower with increasing temperature. The BET surface area decreases from 806 (KIT-500) to 227 m^2g^{-1} (KIT-1000) and the pore volume reduces from 1.16 to 0.16 cm^3g^{-1} . The pore wall thicknesses have also been calculated using DFT analysis of the absorption branch of the N_2 isotherm and are presented in Table 4-1. The pore wall thickness increases from 1.9 (KIT-500) to 5.4 nm (KIT-1000) i.e. a change of over 180%.

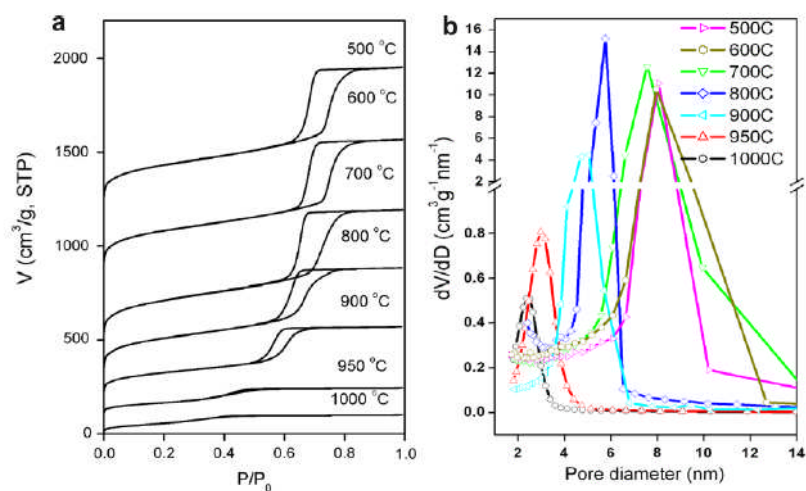


Figure 4-3 (a) N_2 adsorption-desorption isotherms and (b) pore size distribution for the KIT mesoporous silica samples synthesized at different calcination temperatures. The isotherms of KIT-500, KIT-600, KIT-700, KIT-800, KIT-900, and KIT-950 are offset vertically by 1200, 850, 500, 300, 200, and $100 \text{ cm}^3 \text{ g}^{-1} \text{ nm}^{-1}$, respectively.

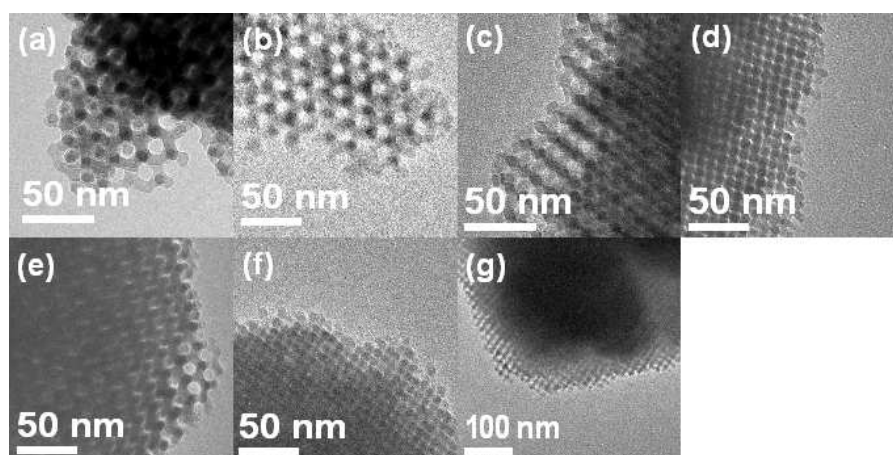


Figure 4-4 TEM figures of mesoporous Co_3O_4 : (a) Co_3O_4 -500, (b) Co_3O_4 -600, (c) Co_3O_4 -700, (d) Co_3O_4 -800, (e) Co_3O_4 -900, (f) Co_3O_4 -950, and (g) Co_3O_4 -1000.

4.2 Mesoporous Co_3O_4

To explore the use of the systematic series of KIT-6 silica mesopores as hard templates for the formation of other mesoporous solids, e.g. mesoporous transitional metal oxides, with controlled pore size and wall thickness, a series of mesoporous Co_3O_4 materials were synthesized.

The formation of ordered mesopore structures for all the mesoporous Co_3O_4 materials was confirmed by TEM (Fig. 4-4). The pore structures replicate that of the hard template KIT-X, with space group of $Ia3d$. The mesoporous structure is preserved throughout each material as confirmed by examination of many different particles.

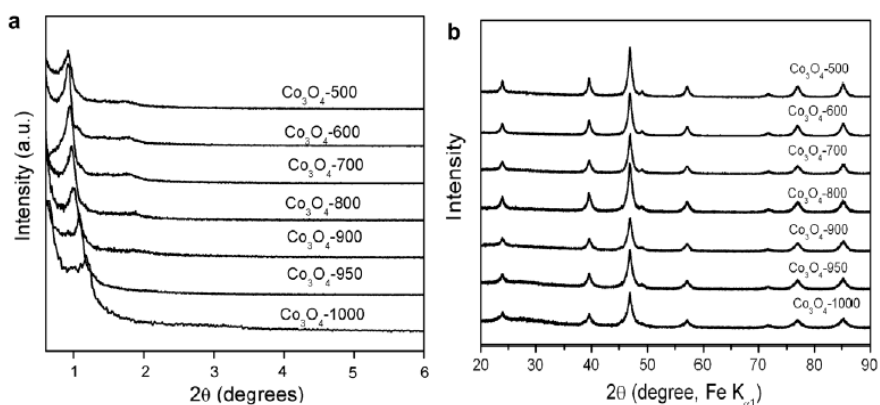


Figure 4-5 (a) Low-angle and (b) wide-angle X-ray diffraction patterns of mesoporous Co_3O_4 prepared from different mesoporous silicas calcined at different temperatures.

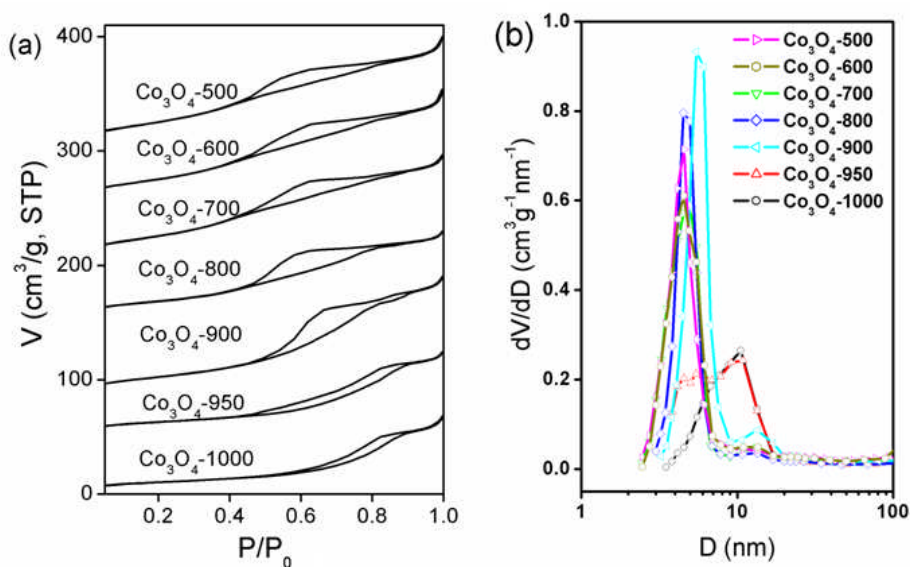


Figure 4-6 (a) N_2 adsorption-desorption isotherms and (b) pore size distribution for the mesoporous Co_3O_4 samples.

The low and wide angle PXRD data are shown in Fig. 4-5. They confirm synthesis of the Co_3O_4 structure (ICDD No. 42-1467) and of an ordered mesostructure, consistent with the TEM data. The somewhat reduced order of

mesoporous silica prepared at the highest temperatures, Fig. 4-2, is reflected in the loss of the higher angle peak near 2° for Co_3O_4 -950 and Co_3O_4 -1000 (Note the temperatures refer to the silica synthesis, as above and not the temperature used to form the Co_3O_4 , which was synthesized at 500°C throughout).

The N_2 -sorption data and pore size distributions for mesoporous Co_3O_4 are shown in Fig. 4-6. Pore sizes, wall thicknesses, pore volumes, surface areas and mesostructure lattice parameters are presented in Table 4-1. The lattice parameters exhibit the same trend as for the silica, reducing with increasing temperature. The wall thickness of the Co_3O_4 agrees well with the pore diameter of the corresponding silica, both reduce with increasing temperature. The pore diameter of the Co_3O_4 increases with increasing temperature, as does the corresponding silica wall thickness, however the diameter of the former is always larger than the silica wall thickness. Such a difference is commonly observed and has been attributed to incomplete occupation of the pore space with Co_3O_4 after calcination.^{57,118} Considering the pore size distribution, Fig. 4-6b, above 800°C it exhibits two peaks, with the larger pore size increasing in proportion with temperature. It is known that the larger pore arises when the microporous bridges linking the two sets of pores in KIT-6 are broken, resulting in the filling of one or other set of pores but not both simultaneously.^{64,72,79} We conclude that the higher calcination temperature must reduce the micro-bridges resulting in the appearance of the larger pores in the replica Co_3O_4 structure.

4.3 Conclusions

The pore size and wall thickness of mesoporous silica, specifically 3D mesoporous KIT, have been varied over a wide range encompassing pore diameters from 2.4 to 8.1 nm and wall thicknesses from 1.9-5.4 nm, respectively by controlling the calcination temperature between 500 to 1000°C . This range of materials has been used as hard templates to form the mesoporous metal oxide Co_3O_4 , with pore sizes and wall thicknesses within the ranges 3.7 to 11.9 nm and 2.2 to 8.2 nm respectively. When the calcination temperature of the mesoporous silica is greater than 800°C , a bimodal mesoporous metal oxide is obtained.

Table 4-1 Texture properties of the mesoporous silicas and the cobalt oxides

Parameter	Mesoporous silica ^a							Mesoporous Co ₃ O ₄ ^a						
	500	600	700	800	900	950	1000	500	600	700	800	900	950	1000
$a_{\text{XRD}}^{\text{b}}$ (nm)	25.2	25.0	24.5	23.6	21.5	19.9	17.3	23.6	23.5	23.0	22.3	22.0	19.9	18.4
$a_{\text{TEM}}^{\text{c}}$ (nm)	24.7	24.4	23.9	22.9	20.7	17.8	16.9	-	-	-	-	-	-	-
$S_{\text{BET}}^{\text{d}}$ (m ² g ⁻¹)	806	785	742	724	447	249	227	98	96	98	68	77	46	37
V^{e} (cm ³ g ⁻¹)	1.16	1.10	1.07	0.90	0.58	0.22	0.16	0.16	0.16	0.15	0.12	0.16	0.11	0.11
D^{f} (nm)	8.1	8.0	7.3	6.0	4.7	3.0	2.4	3.7	3.8	3.8	4.1	6.2	7.7	11.9
W^{g} (nm)	1.9	1.9	2.3	3.5	3.9	5.1	5.4	8.1	8.0	7.7	7.0	4.8	2.2	-
$V_{\text{micro}}^{\text{h}}$ (cm ³ g ⁻¹)	0.089	0.070	0.023	0.019	0.001	-	-	-	-	-	-	-	-	-

^a The numbers correspond to the silica template calcination temperature; ^b The unit cell parameters a_{XRD} obtained from the small angle X-ray diffraction patterns; ^c The unit cell parameters a_{TEM} extracted from TEM data; ^d S_{BET} , BET surface area deduced from N₂ isotherms in the relative pressure range 0.05-0.25; ^e V , total pore volume at relative pressure 0.99; ^f D , pore diameters calculated using the BJH method from the adsorption branch; ^g W , pore wall thickness calculated by the DFT method; ^h V_{micro} , micropore volume, calculated by the t -plot method.

Chapter 5 Influence of size on the rate of mesoporous electrodes for lithium batteries

Composite electrodes containing ordered mesoporous intercalation hosts, e.g. mesoporous LiMn_2O_4 spinel, have been described and shown to exhibit superior rate performance and capacity retention on cycling, compared with bulk and nanoparticulate electrodes; thus demonstrating the potential advantages of mesoporous electrodes.⁹⁷ However, a fundamental understanding of how the critical dimensions of pore size and wall thickness control the rate capability of such an electrode is important in further evaluating the potential of mesoporous intercalation electrodes. This problem was addressed in this chapter. We choose the mesoporous intercalation electrode $\beta\text{-MnO}_2$ to investigate the influence of the meso-dimensions on rate capability for several reasons.⁸³ First, it is quite challenging to prepare a series of mesoporous intercalation electrodes of the same material that vary systematically in pore size and wall thickness whilst preserving the same highly crystalline structure within the walls, but this has proved possible for $\beta\text{-MnO}_2$. Second, it has been shown previously that intercalation of Li into mesoporous $\beta\text{-MnO}_2$ on the first discharge is associated with a two-phase intercalation reaction, whereas on subsequent cycling lithium intercalation occurs within a single phase. Such duality allows us to investigate the influence of pore size and wall thickness on two-phase and single-phase intercalation processes within the same material.⁸⁴

5.1 Results and discussion

Here first the control of pore size/wall thickness and characterization of the mesoporous materials will be described, followed by the structure analysis of the lithium intercalated, $\text{Li}_x\text{MnO}_2\text{-}\beta$, phase and then the electrochemical behaviour associated with the two-phase and single-phase intercalation will be discussed.

5.1.1 Control of pore size/wall thickness

Ordered mesoporous $\beta\text{-MnO}_2$ was synthesized using the ordered mesoporous silica, KIT-6 as a hard template (Section 3.6), because the high processing temperatures compared with soft templates ensures the combination of an ordered pore structure and highly crystalline walls that is desirable for intercalation. KIT-6 possesses a 3D pore structure that results in a mesoporous $\beta\text{-MnO}_2$ with a replica 3D pore architecture.⁸³ The pore size of KIT-6 was varied by altering the hydrothermal conditions used during the synthesis.^{25,28} Since the pores of the silica template become the walls of the mesoporous $\beta\text{-MnO}_2$, it is possible to obtain a range of wall thicknesses for the latter. It is difficult to vary continuously the pore size in mesoporous $\beta\text{-MnO}_2$. However

it is possible to prepare mesoporous β -MnO₂ with a bimodal pore size distribution and to vary the ratio of the two pore sizes and in this way explore the influence of pore size on rate. KIT-6 contains two set of mesopores connected by microporous channels.^{25,28,29} The prevalence of these channels varies with the hydrothermal synthesis conditions. A large number of microporous channels ensures complete filling of both sets of mesopores resulting, on casting, in mesoporous β -MnO₂ with pores of \sim 3.4 nm diameter, whereas fewer microporous channels, along with the use of a lower ratio of Mn(NO₃)₂ to KIT-6, results in a mesoporous β -MnO₂ with 11 nm diameter pores.^{58,72,79} A more detailed explanation of how different pore sizes may be generated is given in the cited references.^{64,72,79} Generally bimodal pore size distributions are obtained (i.e. 3.4 nm and 11 nm diameter pores co-exist). In this way mesoporous β -MnO₂ with different proportions of large (*ca.* 11 nm) to small (*ca.* 3.4 nm) diameter pores may be prepared. The degree to which the pore size and wall thickness can be varied whilst preserving the highly ordered mesostructure is restricted. Therefore to explore thicker walls and larger pores we synthesized two mesoporous β -MnO₂ materials with disordered pore structures. The first uses a silica template synthesized by the same method as KIT-6, but employing different mole ratios of reactants that take the solution composition outside the ordered regime (Section 3.3).²⁵ The second employed colloid silica beads (\sim 30 nm) that self-assembly to form a mesoporous structure (see Section 3.7).

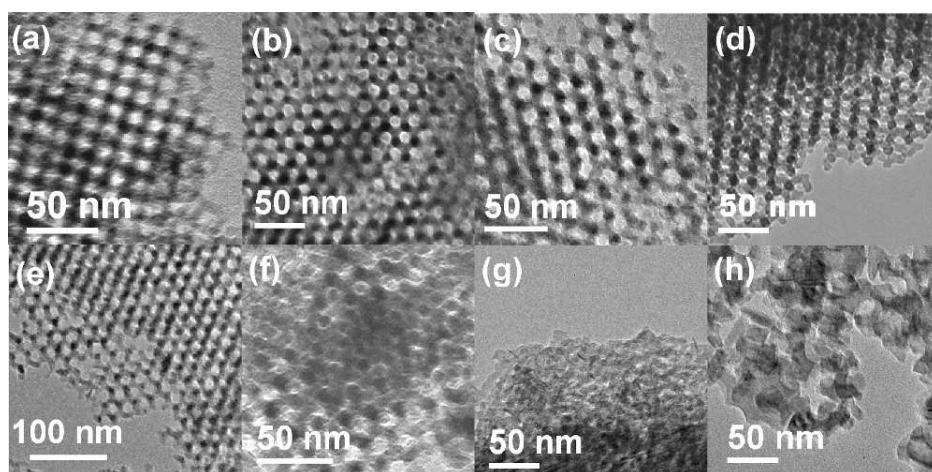


Figure 5-1 TEM images of different crystalline mesoporous β -MnO₂ materials: (a) β -MnO₂-45, (b) β -MnO₂-60, (c) β -MnO₂-80, (d) β -MnO₂-100, (e) β -MnO₂-100B, (f) β -MnO₂-120, (g) β -MnO₂-d4, and (h) β -MnO₂-d30.

The following nomenclature was used to describe the various mesoporous β -MnO₂ materials: β -MnO₂-45, 60, 80, 100, 120 - templated from KIT-6 synthesized using the corresponding hydrothermal temperatures. β -MnO₂-100B - templated from KIT-6 synthesized at 100 °C but with a lower proportion of β -MnO₂ precursor to KIT-6 ratio than β -MnO₂-100 (Section 3.7). β -MnO₂-d4 and β -MnO₂-d30 correspond to the two disordered materials with average pore dimensions of 4 and 30 nm, respectively.

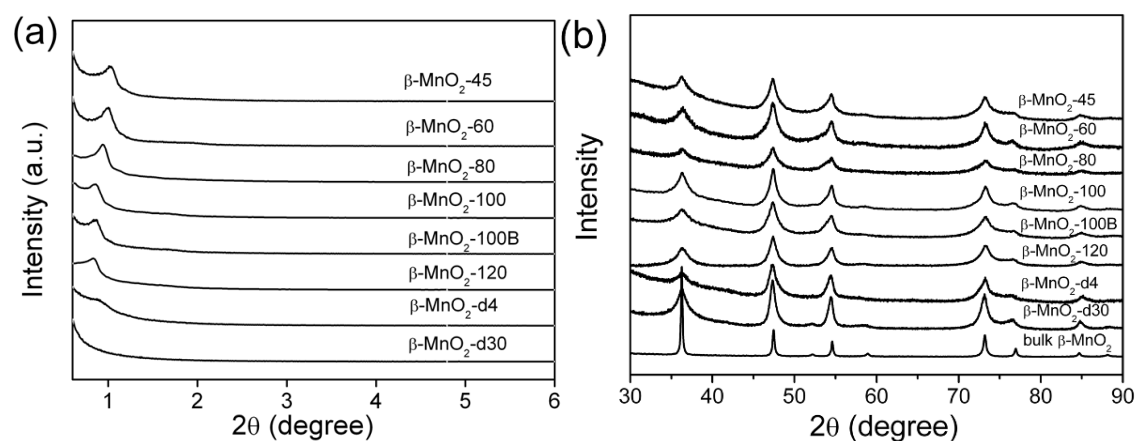


Figure 5-2 (a) Low-angle and (b) wide-angle PXRD patterns of different crystalline mesoporous β -MnO₂ materials.

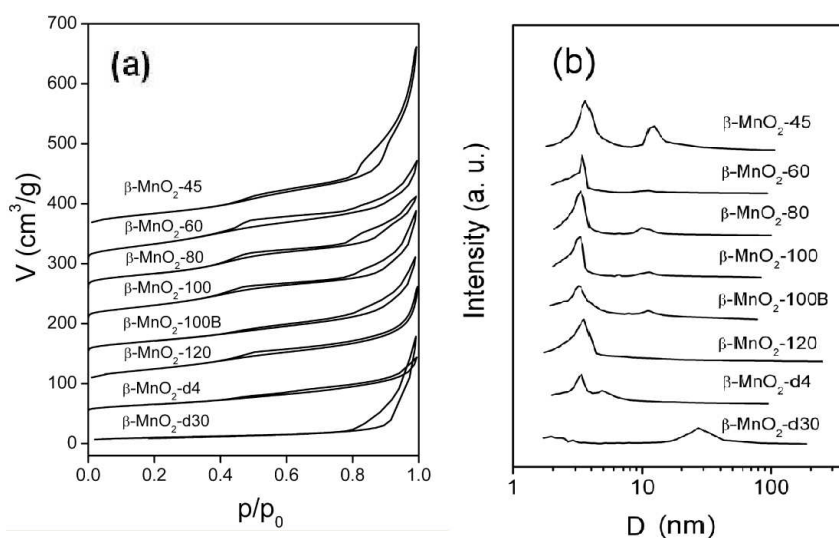


Figure 5-3 N₂ adsorption-desorption isotherms (a) and pore size distributions (b) for the crystalline mesoporous β -MnO₂ materials. The isotherms for β -MnO₂-45, β -MnO₂-60, β -MnO₂-80, β -MnO₂-100, β -MnO₂-100B, β -MnO₂-120, β -MnO₂-d4, and β -MnO₂-d30 are offset vertically by 350, 300, 250, 200, 150, 100, 50, and 0 cm³/g, respectively.

TEM images for the various mesoporous materials are shown in Fig. 5-1. The porosity is clearly evident and examination of many particles demonstrated that the mesoporosity is replicated throughout the materials. Low and wide angle powder X-ray diffraction data for all the materials are presented in Fig. 5-2. The mesoporous materials from β -MnO₂-45 through to 120 all exhibit a well defined low angle peak at around 1° in 2 θ , consistent with the well ordered pore structures evident in Fig. 5-1(a-f). The peak in Fig. 5-2(a) corresponds to the 211 reflection of the *Ia3d* space group anticipated for the replica structure of KIT-6. The a_0 lattice parameters for the mesostructures obtained from the low angle PXRD data are presented in Table 1.

Table 5-1 Physicochemical properties of the mesoporous β -MnO₂ materials ^a

Materials	a_0 (nm)	S_{BET} (m ² /g)	D (nm)	V (cm ³ /g)	Pore wall thickness (nm, by TEM)
β -MnO ₂ -45	21.0	123	3.5/11.2 (0.46)	0.48	4.7
β -MnO ₂ -60	21.6	133	3.4/11.0 (0.06)	0.24	5.0
β -MnO ₂ -80	23.0	124	3.3/11.0 (0.14)	0.24	6.5
β -MnO ₂ -100	25.2	121	3.3/11.1 (0.14)	0.26	7.5
β -MnO ₂ -120	25.9	99	3.5	0.25	8.5
β -MnO ₂ -100B	25.0	87	3.3/11.1 (0.26)	0.23	7.5
β -MnO ₂ -d4	24.7	120	3.4/5.0 (0.45)	0.25	8-10
β -MnO ₂ -d30	-	35	28	0.24	20-30

^a a_0 , the unit cell parameters obtained from the low-angle PXRD data; S_{BET} , surface area calculated by the BET method; D , pore diameter calculated by the BJH method (ratios of large (11 nm or 5 nm) to small (3.4 nm) pore volumes are given in parentheses); V , total pore volume at $P/P_0 = 0.99$.

Although β -MnO₂-d4 is designated as disordered, a small peak is evident in the low angle PXRD indicating a degree of order.²⁰ From the wide angle PXRD data, Fig. 5-2(b), it is clear that all the mesoporous materials possess the same β -MnO₂ crystal structure, although of course the peaks are broadened compared with bulk β -MnO₂ in keeping with the small dimensions of the mesoporous walls.

The pore structures were investigated further by nitrogen sorption measurements (Fig. 5-3a). These data exhibit a typical type IV isotherm with a H2 hysteresis loop, as expected for such mesoporous metal oxides.^{15,58} The BET surface areas, pore sizes (determined by the BJH method), pore volumes and wall thicknesses are presented in Table 5-1. The relative proportions of the two sets of pores were obtained from the peak areas in the pore size distribution plot (Fig. 5-3b). The pore volumes are similar for all the materials except β -MnO₂-45. Considering first the four mesopores, β -MnO₂-60, 80, 100, and 120, the pore wall thickness increases systematically from 5.0 to 8.5 nm on increasing the hydrothermal synthesis temperature. The pore sizes for all four mesopores are invariant but the proportion of the larger (11 nm pores) is very small (6% and 0%) for β -MnO₂-60 and 120, rising to 14% for β -MnO₂-80 and 100. β -MnO₂-100B possesses the same wall thickness and pore size as β -MnO₂-100 but the proportion of larger (11 nm pores) has increased substantially to 26% and the surface area has decreased; thus offering a very direct comparison of how such factors influence the performance. As can be seen from Table 1 the two disordered materials exhibit thicker walls, 8-10 and 20-30 nm for β -MnO₂-d4 and d30, respectively. Although the larger pore in β -MnO₂-d4 (5 nm) is smaller than those in ordered materials (11 nm), the proportion of the larger pores in β -MnO₂-d4 is significantly high at 45%. β -MnO₂-d30 possesses a large pore size of ~28 nm diameter. Of course with these disordered materials pore size distributions are inevitably broader than in the highly ordered materials.

5.1.2 The structure of mesoporous Li_xMnO₂- β

On intercalating lithium into mesoporous β -MnO₂, the material transforms from the tetragonal rutile structure (space group P4₂/mnm) to a new phase, mesoporous Li_xMnO₂- β with orthorhombic symmetry (space group Pnnm). Note that the previous report of this transformation assigned a tetragonal space group to Li_xMnO₂- β , as a result of the poor quality of the powder X-ray diffraction data.⁸³ The powder neutron diffraction pattern for the Li_xMnO₂- β phase exhibits very broad peaks (Fig. 5-4(a)), to an extent that precludes direct structure elucidation. Recently we have investigated lithium intercalation into β -MnO₂ nanowires with a diameter of approximately 50 nm. The powder neutron diffraction pattern is shown in Fig. 5-4(b). Comparison of Fig. 5-4(a) and 4(b) demonstrate significant structural similarity. Both patterns may be indexed on the same orthorhombic unit cell, but because the diameter of the wires is much greater than the thickness of the walls in mesoporous β -MnO₂ (~ 8 nm), the peaks

in the neutron powder pattern of the Li_xMnO_2 - β nanowires are sharper and hence better resolved (Fig. 5-4(b)). By first elucidating the structure of the Li_xMnO_2 - β nanowires, it has been possible to establish the structure of lithium intercalated mesoporous β - MnO_2 . Structure elucidation of the Li_xMnO_2 - β nanowires is described in detail elsewhere and is based on refinement starting from Li_xRuO_2 .^{140,141} Using the structure obtained for the lithium intercalated nanowires, Rietveld refinement was carried out on the Li_xMnO_2 - β mesoporous phase, resulting in the structure shown in Fig. 5-5(b) and detailed in Table 5-2. The fit is good, as is reflected in a R_{wp} of 2.4% ($R_{\text{exp}} = 2.1\%$). The structure of mesoporous orthorhombic Li_xMnO_2 - β is in essence a significantly distorted form of the tetragonal rutile structure with Li^+ ions in the tunnels (Fig. 5-5). Comparison of the lattice parameters of the parent phase with those for mesoporous Li_xMnO_2 - β shows that a very large anisotropic cell expansion occurs on lithium intercalation. The a parameter expands by almost 16.7%, and b by 13.5%, whilst the c parameter actually contracts by 2%. The c direction lies along the 1×1 tunnels with a and b perpendicular to the tunnel axis. The large increase in a and b corresponds to a significant increase in the width of the 1×1 tunnel in order to accommodate the Li^+ ions, which are located in the octahedral sites. The MnO framework is clearly similar to the parent rutile structure but the MnO_6 octahedra are enlarged and distorted, with elongated apical bonds, consistent with Jahn-Teller active Mn^{3+} (MnO_6 distortion shown in Fig. 5-5). The elongation of the MnO_6 octahedra occurs along the $[110]$ direction in the ab plane and is in accord with the expansion of 1×1 tunnels.

Table 5-2 Refined crystallographic parameters for mesoporous Li_xMnO_2 - β -100 at end of the first discharge.

$R_e = 2.1\%$, $R_{\text{wp}} = 2.4\%$, $R_p = 2.1\%$, Space group $Pnmm$, $a = 5.141(7) \text{ \AA}$, $b = 5.003(2) \text{ \AA}$, $c = 2.8131(8) \text{ \AA}$.

Atom	Wyckoff symbol	x/a	y/b	z/c	B_{iso}	occupancy
Mn	2a	0.0	0.0	0.0	0.8(2)	1
O1	4g	0.277(3)	0.3218(14)	0.0	0.40(7)	1
Li1	2d	0.0	0.5	0.5	0.5(-)	0.99(12)

6.1.3 Electrochemical behavior

Composite electrodes composed of the various mesoporous materials, carbon, and binder, were fabricated as described in Section 2.10. Since our primary interest is to understand how the meso-dimensions of the mesoporous electrodes influence the rate capability, it is important to establish first that the observed electrochemical behavior is limited by these factors, rather than by lithium ion transport between the particles or electron transport to the particles. It has been known for decades that, especially at high rates, the transport of lithium within the electrolyte inside the composite electrode can be rate limiting.¹⁴² Such transport may be confused with diffusion inside the particles. To ensure that the electrode thickness and

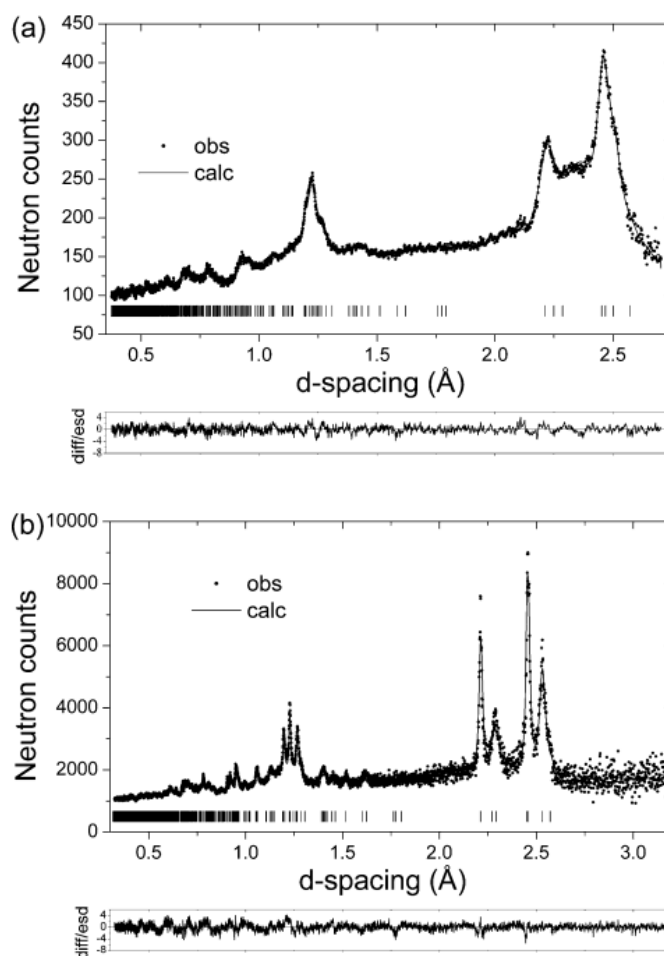


Figure 5-4 Refined powder neutron diffraction patterns for (a) mesoporous $\text{Li}_x\text{MnO}_2\text{-}\beta\text{-100}$, (b) $\text{Li}_x\text{MnO}_2\text{-}\beta$ nanowires. Dots represent observed data and solid line the calculated pattern. The lower line is the difference/esd. Tick marks represent allowed reflections.

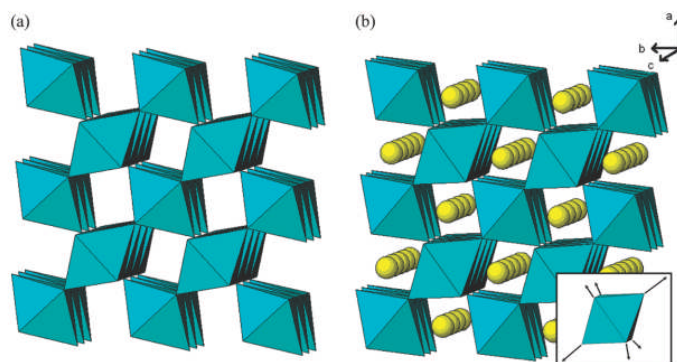


Figure 5-5 Crystal structures of (a) β - MnO_2 and (b) Li_xMnO_2 - β viewed down the 1×1 tunnels. Inset shows the distortion of the MnO_6 octahedra on intercalation.

current densities used here are within a range such that the rate is not limited by transport in the electrolyte, β - MnO_2 -100B electrodes were prepared with various electrode thicknesses (loadings). Their discharge capacities are shown in Fig. 5-6 for two different rates, 600 and 1500 mA/g. At the highest rate, the highest loading is associated with a lower capacity, therefore a loading of 2.5 mg/cm^2 was chosen in order to investigate the effect of mesoporous dimensions on rates up to 1500 mA/g. To ensure that the rate performance was not limited by electron transport to the particles, three different β - MnO_2 -100B based electrodes containing increasing proportions of carbon were investigated, Fig. 5-7. At the highest rate used, 1500 mA/g, a carbon content of at least 15% was necessary to ensure that the discharge capacity was not limited by electron transport to the particles. This composite electrode composition was used throughout the remaining studies.

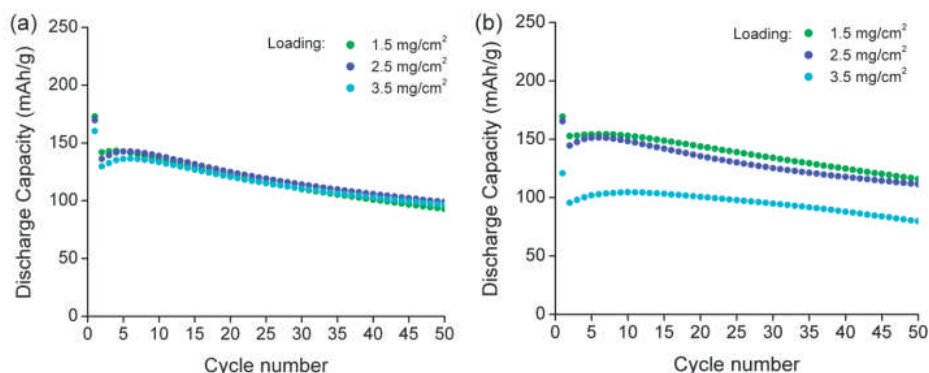


Figure 5-6 Variation of the discharge capacity with cycle number for composite electrodes containing mesoporous β - MnO_2 -100B, Super S carbon and Kyner 2801, with weight ratios of

70:15:15 and with three different β -MnO₂ mass loadings, at rates of (a) 600 mA/g and (b) 1500 mA/g.

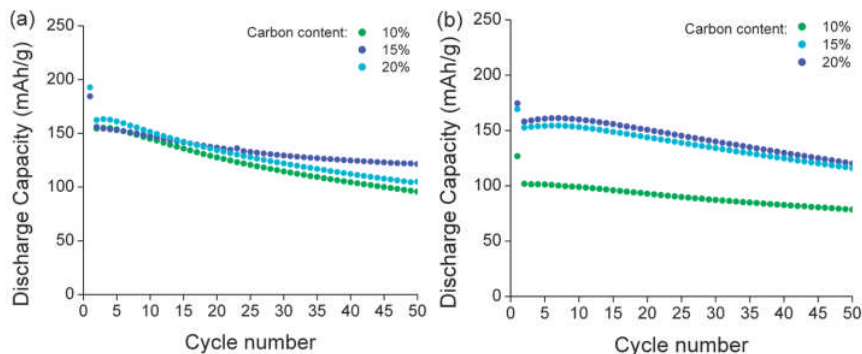


Figure 5-7 Variation of the discharge capacity with cycle number for composite electrodes containing mesoporous β -MnO₂-100B, Super S carbon, and Kyner 2801 with the three different weight ratios (green 80:10:10, blue 70:15:15, cyan 70:20:10) at rates of (a) 300 mA/g and (b) 1500 mA/g. The active material mass loading is 2.5 mg/cm².

The variation of load potential with state-of-charge for the first and tenth cycles of mesoporous β -MnO₂ is shown in Fig. 5-8. The first discharge exhibits a well defined plateau associated with the two-phase intercalation process between β -MnO₂ and Li_xMnO₂- β . After cycling, the load curve shows a continuous variation of potential with state of charge, in accord with the known single phase intercalation process associated with Li_xMnO₂- β .⁸³ In the following two sections we consider, in turn, how the mesodimensions influence the one and two-phase intercalation processes.

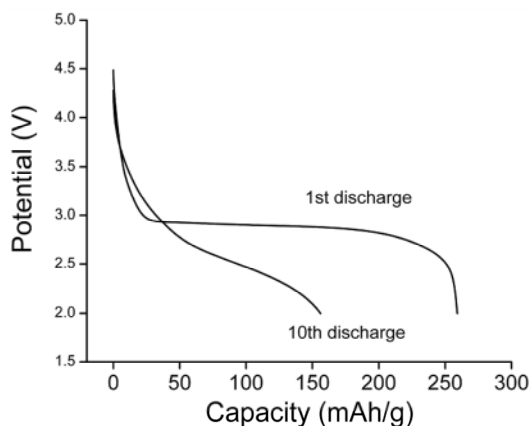


Figure 5-8 Typical variation of potential with state of charge (load curves) for the first and tenth discharges of mesoporous β -MnO₂.

5.1.4 Influence of mesodimensions on the two-phase intercalation reaction (first discharge of β -MnO₂)

The discharge rate capability of each mesoporous β -MnO₂ material on 1st discharge is demonstrated by plotting the variation of the first discharge capacity as a function of current density (rate). These data are presented in Fig. 5-9. The better the capacity retention with increasing the current density, the better the discharge rate capability of the material. The absolute capacities at low rates differ for different mesopores (we shall return to this point later) hence the data are presented as a percentage of the discharge capacity at the lowest rate (15 mA/g) to facilitate comparison of the rate capabilities for different mesoporous materials. Considering first the four materials, mesoporous β -MnO₂-60, 80, 100, and 120, which differ principally in their wall thickness, it is evident that the rate capability decreases with increasing pore wall thickness from 5 to 8.5 nm i.e. an increase in wall thickness of 70%.

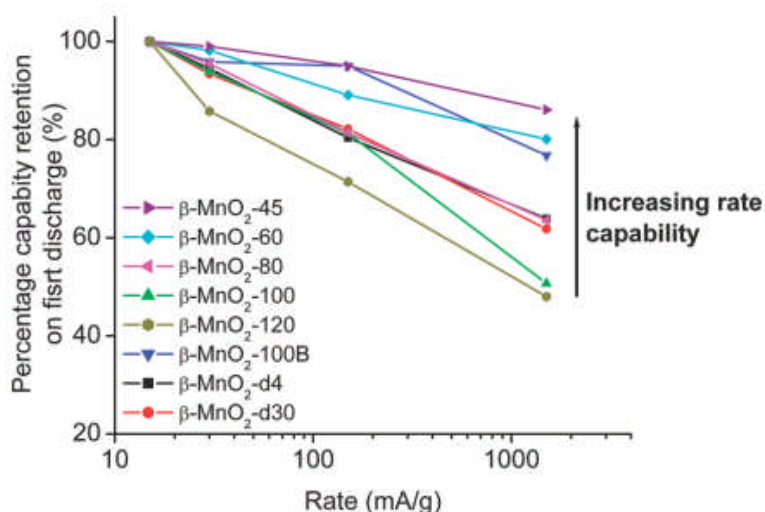


Figure 5-9 The first discharge capacity for different mesoporous β -MnO₂ electrodes as a function of rate. Note the capacity is expressed as a percentage of the discharge capacity at the lowest rate (15 mA/g). The active material mass loading is 2.5 mg/cm².

Comparing the rate capability of β -MnO₂-100B and β -MnO₂-100, the capacity retention of the former is clearly superior to the latter. The wall thickness is the same in both cases, 7.5 nm, therefore the origin of the difference must lie in the pore size. β -MnO₂-100B possesses a significantly higher proportion of the larger, 11 nm, pores, 26% versus 14%. This demonstrates that, for pore sizes and wall thicknesses within the range studied in this work, both parameters

play an important role in determining the rate. The significance of the pore size is further reinforced by comparing β -MnO₂-45 and β -MnO₂-60; there is only a small difference in wall thickness (4.7 and 5 nm respectively) but the latter has a much higher proportion of 11 nm pores (46% vs 6% for β -MnO₂-60). β -MnO₂-45 exhibits better rate performance than β -MnO₂-60.

Comparing the rate capability of the disordered materials with those just discussed, β -MnO₂-d4 has a greater wall thickness than β -MnO₂-100 and β -MnO₂-100B, yet its rate capability lies between the two 100 materials, this must be an effect of the pore sizes. Although β -MnO₂-d4 does not have 11 nm pores, it does have a higher proportion of 5 nm pores (45%) compared with the proportion of 11 nm pores in either β -MnO₂-100 (14%) or β -MnO₂-100B (26%). It appears that such a large proportion of 5 nm pores is sufficient to raise the rate capability of β -MnO₂-d4 above that of β -MnO₂-100 but not β -MnO₂-100B. Finally, β -MnO₂-d30 has thick walls, 20-30 nm, and therefore should have the poorest rate performance. However it also has the largest pores, ~ 28 nm, which places its rate capability between β -MnO₂-100 and β -MnO₂-100B.

Considering the influence of pore size on rate, an increase in rate capability with increasing pore diameter is consistent with the expectation that larger pores permit more facile Li⁺ transport in the electrolyte within the pores. The data presented here show that varying the pore size between 5 and 30 nm has a significant effect on the rate capability for current densities in the range 100-1500 mAh/g.

Considering the influence of wall thickness on rate, it is known that for two phase intercalation reactions, such as in LiFePO₄, nanoparticles exhibit significantly higher rate capability than micron sized particles.¹⁴³⁻¹⁴⁷ Recent work has attributed this to a change in the intercalation mechanism from one in which the new phase, in this case FePO₄, nucleates and grows through the LiFePO₄ particle when of micron dimensions¹⁴⁸ to one in which either LiFePO₄ or FePO₄ but not both, are present within a single particle.¹⁴⁹ In the case of mesoporous electrodes the walls are of nanometer dimensions but the particles are micron sized, hence an entire particle cannot convert from one phase to another, phase boundaries must remain. The results presented here show that the thin walls can accommodate the strain of the phase boundary between β -MnO₂ and Li_xMnO₂- β despite the large volume expansion on intercalation (55.7 to 72.3 Å³) and its significant anisotropy ($a = 4.406(4)$ Å, $c = 2.868(4)$ Å for the β -MnO₂; and $a = 5.141(7)$ Å, $b = 5.002(2)$ Å, $c = 2.813(8)$ Å for Li_xMnO₂- β). For this

reason, despite the particle size being of micron dimensions, the intercalation process is rendered far more facile than for dense micron sized materials.

5.1.5 First discharge capacity at low rates

In order to compare the discharge rate capabilities of different mesoporous β - MnO_2 materials, the capacities in Fig. 5-9 were expressed as a percentage of their capacity at the lowest rate (15 mA/g), because the low rate capacities differ from one mesoporous β - MnO_2 to another. The first discharge capacities at 15 mA/g for each mesopore are presented in Fig. 5-10. Considering the four mesoporous materials β - MnO_2 -45, β - MnO_2 -60, β - MnO_2 -80, and β - MnO_2 -100, it is clear that the discharge capacity increases with increasing wall thickness. This is counter to what would be expected if the capacities were limited by kinetics. We have observed similar behaviour in other mesoporous materials, specifically mesoporous β - MnO_2 with a 1D pore structure prepared from SBA-15, for which capacities increased from 225 mAh/g (wall thickness 7.5 nm) to 265 mAh/g (wall thickness 10.1 nm) at 15mA/g.¹⁵⁰ We cannot be certain of the origin of this effect but offer the following hypothesis. We propose that the explanation lies in the relative proportion of "bulk" and "near surface" regions within the walls of the mesoporous solids and that the latter is a poor host for Li. At the centre of the walls of the mesoporous solid, farthest from the pores, the structure will be that of undistorted bulk β - MnO_2 . Progressing from this region towards the pores, it is possible that the crystal structure will become increasingly distorted. This could arise from the severe curvature of the walls of the small (nm) pores. Recently, we have studied a different nanomaterial, $\text{TiO}_2(\text{B})$ nanotubes.¹⁵¹⁻¹⁵³ The nanotube is composed of thin walls formed by folding a 2.5 nm slab, of the $\text{TiO}_2(\text{B})$ crystal structure to form a tube of internal diameter 5 nm. We have shown that this curvature induces severe distortions of the regular $\text{TiO}_2(\text{B})$ crystal structure.¹⁵³ However in the case of $\text{TiO}_2(\text{B})$ nanotubes the distorted structure results in an increased capacity to store Li, whereas here the opposite must be true. It should be recalled that the mesoporous materials are grown within a silica template, the walls of which are disordered and form interfaces with what becomes the pore surfaces of β - MnO_2 on template removal. This could induce disorder in the β - MnO_2 walls close to the pore surfaces. The thinnest pore walls are found for β - MnO_2 -45 (4.7 nm) with the pore wall thickness increasing by 50% in the case of β - MnO_2 -100. Therefore the proportion of distorted "near-surface" structure compared with "bulk" structure will be greatest for β - MnO_2 -45. If the distorted structure is less able to accommodate lithium than the undistorted (bulk)

structure then the highest capacity will be found in the mesopore with thickest walls i.e. in β -MnO₂-100, in accord with observation (Fig. 5-10).

A further increase in wall thickness does not increase the capacity, as demonstrated by β -MnO₂-d4 and β -MnO₂-d30. This may be attributed to the fact that as the walls become thicker the proportion of undistorted structure dominates and hence the capacity saturates. Finally, we must consider the cases of β -MnO₂-100B and β -MnO₂-120 the former exhibits a lower first discharge capacity than β -MnO₂-100 with the same wall thickness and the latter a lower capacity despite thicker walls. The common factor is both have significantly lower surface areas than β -MnO₂-100 (Table 5-1). Why should the reduction in surface area reduce the capacity of the material? When lithium is inserted into β -MnO₂, the lithium rich phase will nucleate and grow at a variety of points scattered across the pore wall surfaces. We speculate that the lower surface areas of β -MnO₂-100B and β -MnO₂-120 will result in fewer nuclei from which the new phase grows and, even at this low rate, greater polarization will occur. However this hypothesis requires further examination in future work.

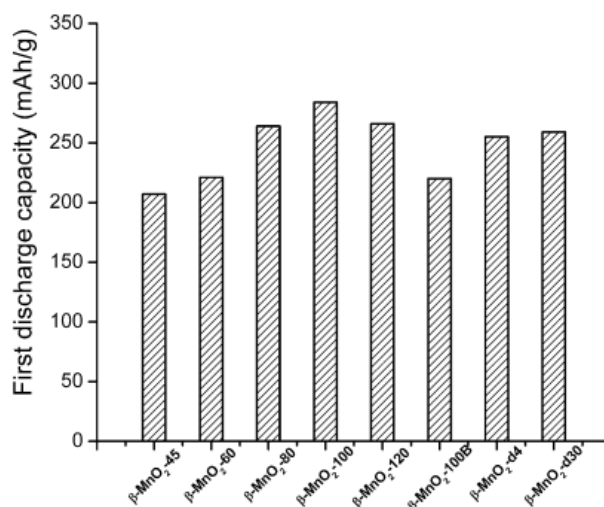


Figure 5-10 The first discharge capacities at 15 mA/g for different mesoporous β -MnO₂.

5.1.6 Influence of meso-dimensions on the single phase intercalation reaction (10th discharge of β -MnO₂)

Turning to the influence of pore size and wall thickness on the rate of lithium intercalation for a single phase reaction, i.e. at high cycle numbers within the mesoporous Li_xMnO₂- β phase, the discharge capacity retention with increasing rate for cycle 10 is shown in Fig. 5-11. The data demonstrate that at the extremities of the range of pore size/wall thickness explored in this work,

i.e. for β -MnO₂-45 (which combines the thinnest walls, 4.7 nm, with a high proportion, 46%, of large, 11 nm, pores) and β -MnO₂-120 (combining relatively thick walls, 8.5 nm, with 100% of 3.5 nm pores), pore size and wall thickness influence the rate performance. However, it is interesting to note that the rest of the materials studied here, except β -MnO₂-100 at the very highest current density (1500 mA/g) show little variation of rate capability with variation of pore size and wall thickness.

Comparing lithium intercalation into β -MnO₂, *via* a single phase mechanism with that *via* a two-phase process, it is clear that the latter is sensitive to variations in both pore size and wall thickness, whereas the former is insensitive to such variations except for the more extreme combinations of pore size and wall thickness studied here. Of course the range of pore size and wall thickness reported here is limited and restricted to one system β -MnO₂, therefore the observed trends should be considered in that context. Nevertheless they do offer a valuable guide to the effect of mesoporous morphology on electrode performance.

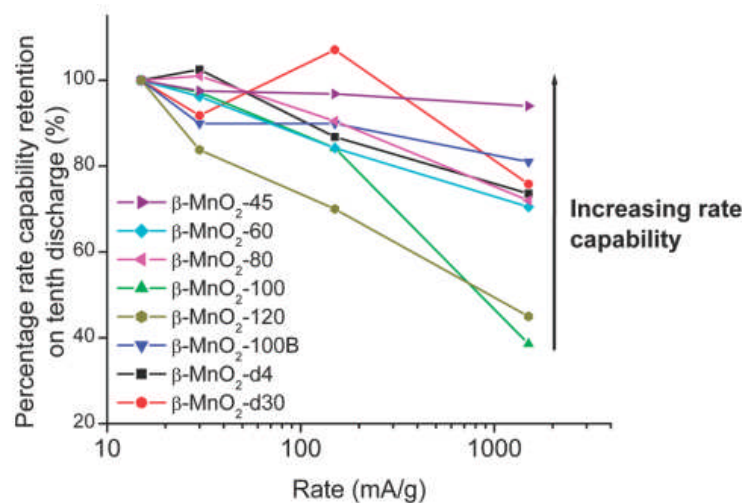


Figure 5-11. The tenth discharge capacities for the different mesoporous β -MnO₂ electrodes at different rates as a percentage of the discharge capacity at the lowest rate (15 mA/g). The active materials mass loading is 2.5 mg/cm².

5.2 Conclusion

By preparing a series of electrodes based on mesoporous β -MnO₂ as the intercalation host, with pore sizes ranging from 3.4 to 28 nm in diameter, and wall thicknesses from 4.7 to 30 nm, it has been possible to explore the influence of pore size and wall thickness on the rate of intercalation. The rate capabilities of both one and two-phase intercalation processes have been

investigated by examining the first discharge (two phase) and tenth discharge (single phase) behavior, permitting comparison of the influence of the pore size/wall thickness between the two mechanisms. The pore size and wall thickness have a significant effect on the rate of lithium intercalation *via* single phase and two phase mechanisms. However the former requires more extreme variation in pore size/wall thickness to promote a change in rate than the latter.

Chapter 6 Lithium intercalation into mesoporous anatase with an ordered 3D pore structure

There is intense interest in lithium intercalation into titanates for two reasons. First, because they have potential advantages (safety, rate) replacing graphite as anodes in a new generation of rechargeable lithium batteries.^{6,154} Second, because they represent an excellent model system (simple composition and structure) with which to investigate the profound influence the nanoscale can have on intercalation.¹⁵⁵⁻¹⁵⁷ Of the various titanates, TiO₂ is potentially the most attractive host, as it can in principle accommodate 1 Li/Ti (336 mAhg⁻¹), however in practice the best that has been achieved for bulk TiO₂ is 0.5Li/Ti in anatase. Reducing the dimensions to the nanoscale transforms the behavior of TiO₂, with much higher capacities to store lithium and better reversibility.¹⁵⁵⁻¹⁵⁷ There is a great deal of interest in TiO₂ nanoparticles, nanowires and nanotubes.^{151,156-159} Here we prepared mesoporous anatase with an ordered 3D pore structure, using a hard template, and investigated its properties as a lithium intercalation host. It exhibits a hierarchical pore structure. Despite being composed of micron sized particles, the ordered mesoporous morphology inside the particles results in a high capacity to store Li and high rates of intercalation. It has been proposed that the reason nanoparticles such as anatase and LiFePO₄ exhibit facile Li insertion is the ability of such particles to transform spontaneously from one phase to the other, i.e., a particle is either phase A or B but not both.^{149,157} The micron sized mesoporous particles cannot do so but still show facile intercalation. This is related to the ease with which the strain of transforming between the anatase (phase A) and the orthorhombic Li_{0.59}TiO₂ structures (phase B) is accommodated within the thin (6.5 nm) walls on intercalation. Exploring the properties of such new electrode architectures represents a scientifically important foundation for the development of new generations of rechargeable lithium batteries to be used in transport and other applications.

6.1 Characterization by TEM, PXRD, and N₂ sorption

Mesoporous anatase with an ordered 3D pore structure was synthesized using the silica KIT-6 as a hard template (see Section 3.11). The ordered pore structure is evident in the TEM data, Fig. 6-1a and 1b, and replicates that of the KIT-6 hard template with

space group $Ia3d$. An a_0 lattice parameter for the mesostructure of 23.3 nm was extracted from the data. The mesoporous structure is preserved throughout as demonstrated by examining many particles. The walls (6.5 nm) are composed of anatase crystallites. A lattice spacing of 0.350 nm was observed in HRTEM (Fig. 6-1b), in good agreement with the d-spacing of 0.352 nm associated with the (101) direction of anatase (ICDD 00-001-5062). The low and wide angle PXRD data are shown in Fig. 6-2. The low angle diffraction patterns exhibit one relatively sharp peak below 1° , which could be indexed as the 211 reflection in the $Ia3d$ space group, corresponding to an a_0 lattice parameter of 23.5 nm in good agreement with the TEM data. The broad peaks in the wide angle PXRD for the as-prepared mesoporous material are in good agreement with those for anatase nanoparticles, AK-1 (Bayer), Fig. 6-2A. The mesoporous anatase peak widths are greater than those of the nanoparticles in accord with the walls being thinner than the diameter of the nanoparticles (15 nm).

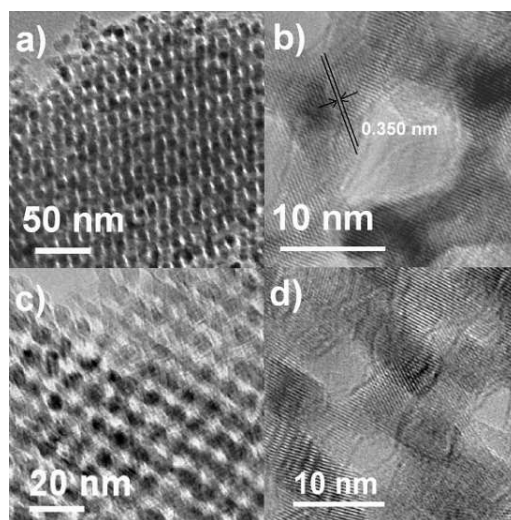
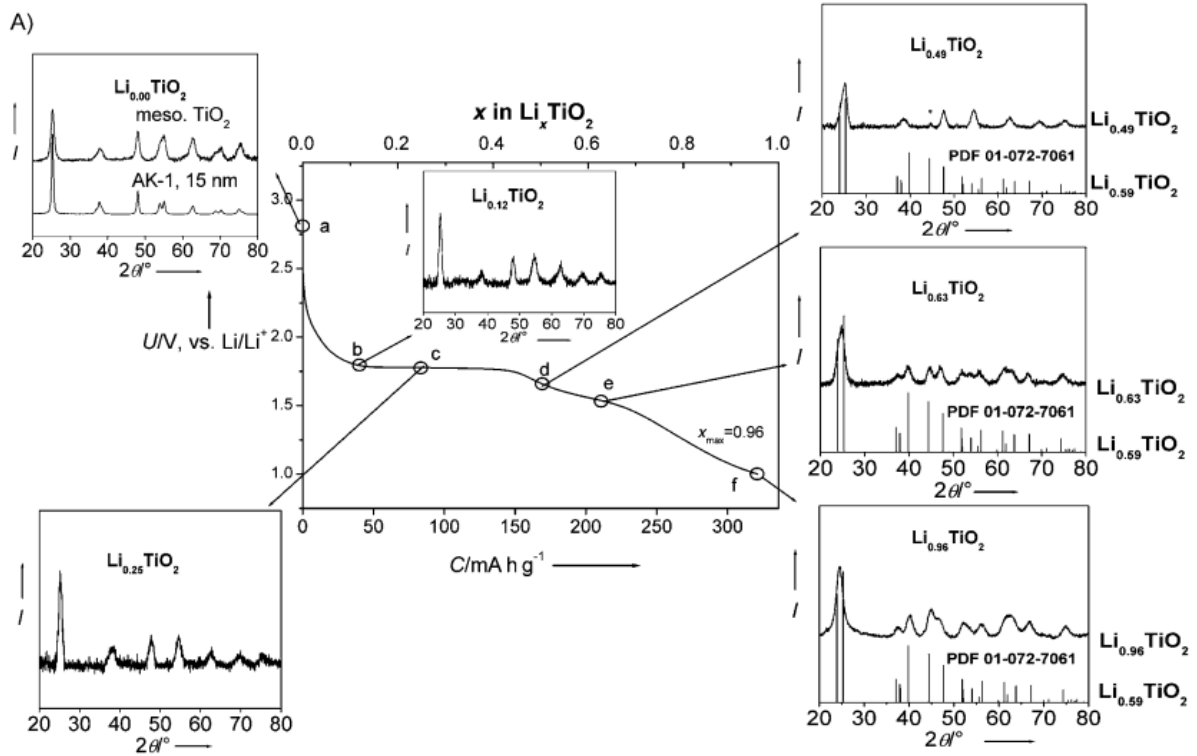


Figure 6-1 TEM and HRTEM data for ordered mesoporous anatase: a) and b), as prepared; c) and d) after 1000 cycles ($12\ 000\ \text{mA g}^{-1}$).

The mesostructures were investigated further by N_2 sorption measurements. Typical type IV isotherms exhibiting H2 hysteresis were observed (Fig. 6-3a); consistent with the mesoporosity evident in the TEM and low angle PXRD data. BJH pore size distributions exhibit at least three peaks, demonstrating a hierarchical pore structure. A well resolved narrow peak centered at 5 nm, a peak at approximately 11 nm and a third broad peak at

~50 nm, (Fig. 6-3b). The first peak corresponds to the mesopores observed by TEM in Fig. 6-1. The second arises because KIT-6 has two interpenetrating sets of pores connected by microporous bridges. In regions where the bridges are complete both pores will be filled and the replica TiO₂ is composed of the 5 nm pores. Where the bridges are incomplete and only one set of KIT-6 pores are filled the replica exhibits 11 nm pores, see Fig. 6-4a. Such a phenomenon had been discussed previously for other KIT-6 templated materials.⁶⁴ The third peak corresponds to interparticle voids. The 11 and 50 nm voids are seen in the TEM data in Fig. 4-9b, providing further evidence for the hierarchical pore structure. The BET surface area is 205 m²g⁻¹.



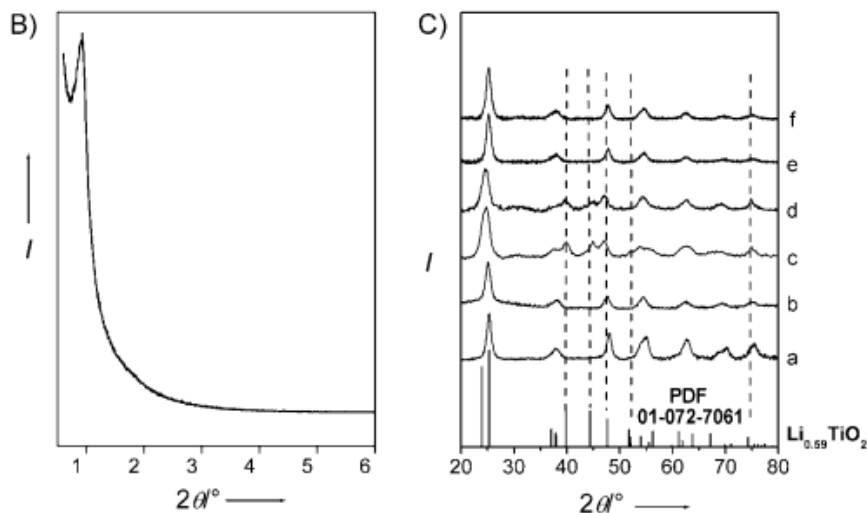


Figure 6-2 A) Variation of potential on the first discharge (30 mA g^{-1}) and associated *ex-situ* wide angle PXRD patterns. B) The low angle PXRD pattern of mesoporous anatase. C) The *ex-situ* wide angle PXRD patterns of a) mesoporous anatase, b) mesoporous anatase charged to 3.00 V on the 2nd cycle, discharged to c) 1.5 V and d) 1.0 V after 200 cycle at the rate of 30 mA g^{-1} , charged to 3 V after e) 500 cycle, and f) 1000 cycle at the rate of $12\,000 \text{ mA g}^{-1}$. Standard of orthorhombic $\text{Li}_{0.59}\text{TiO}_2$ phase (ICDD No. 01-072-7061) is shown for comparison.

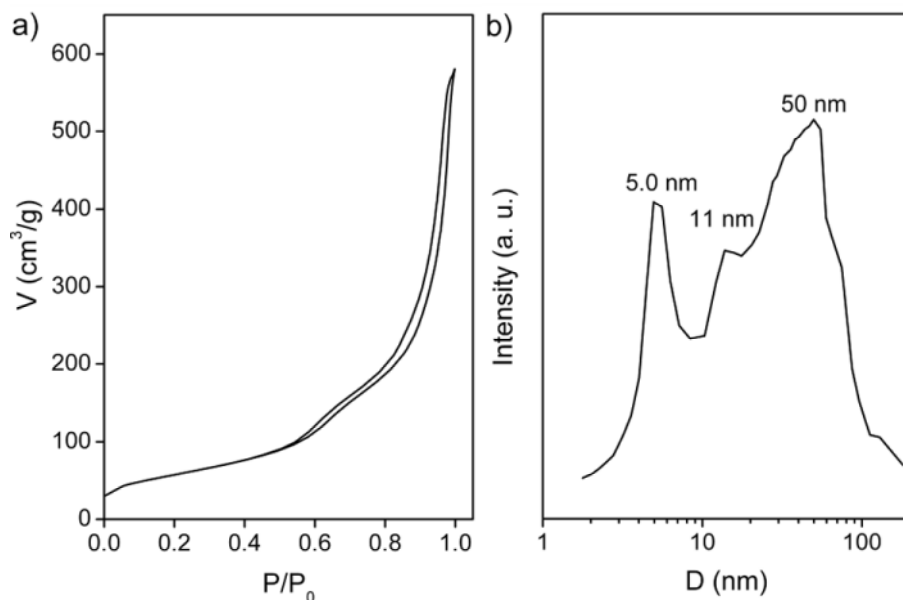


Figure 6-3 N_2 sorption isotherms a) and BJH pore size distribution b) for mesoporous anatase.

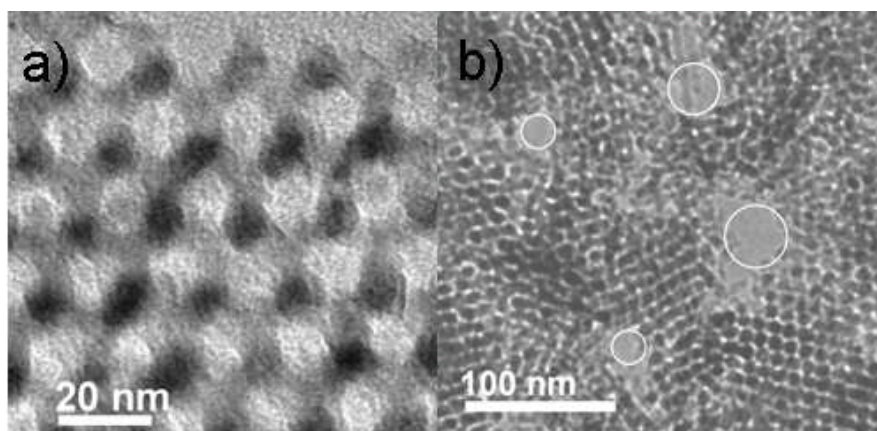


Figure 6-4 a) TEM image showing the 11 nm pores present in mesoporous anatase. b) TEM data of mesoporous anatase at low magnification. Different inter-particle voids are labeled with white circles. All of the voids sizes are between 20-60 nm.

6.2 Structure evolution by *ex-situ* PXRD and *in-situ* Raman microscopy

Electrodes were constructed by mixing anatase, Super S, and Kyner in the weight ratios 70:15:15 and incorporated into electrochemical cells as described in the Section 2.10. The variation of potential on lithium intercalation (discharge) is shown in Fig. 6-2A along with the PXRD data collected at various points along the curve. The load curve and associate structural changes are similar to those observed for nanoparticulate anatase.^{155,156} A capacity of 322 mAhg^{-1} at 0.09C (30 mAg^{-1} ; note that $1\text{C} = 336 \text{ mAg}^{-1}$) is observed. The potential changes continuously for lithium insertion up to $x = 0.12$ in Li_xTiO_2 , in accord with the PXRD data which suggest retention of the tetragonal anatase structure but with a small volume expansion ($a = 3.784 \pm 0.002 \text{ \AA}$, $c = 9.51 \pm 0.015 \text{ \AA}$ for as-prepared mesoporous anatase and $a = 3.797 \pm 0.004 \text{ \AA}$, $c = 9.455 \pm 0.008 \text{ \AA}$ for $\text{Li}_{0.12}\text{TiO}_2$). Thereafter the load curve exhibits a plateau up to approximately $x = 0.46$ indicative of a two phase intercalation process. The 101 anatase peak is broadened by 20 % at $x = 0.25$, providing some evidence that changes are occurring along the plateau. However, no distinct peaks of a second phase appear until the end of the plateau at $x = 0.49$, at which point the 45° peak associated with the orthorhombic phase is observed. Thereafter orthorhombic $\text{Li}_{0.59}\text{TiO}_2$ dominates the PXRD and exhibits a continuous lattice

expansion up to the maximum intercalation composition of $x = 0.96$. The structural changes associated with the load curve were investigated further by *in-situ* Raman microscopy (Fig. 6-5). The as-prepared tetragonal anatase phase is characterized by a strong peak at 150 cm^{-1} that decreases dramatically in intensity on lithium insertion up to $x = 0.05$. Thereafter peaks corresponding to the orthorhombic phase are clearly evident and dominate the spectrum, in part because of the dramatic loss of intensity of the 150 cm^{-1} peak of anatase.¹³⁵ These Raman data demonstrate that the orthorhombic phase begins to grow even before the onset of the plateau. Raman spectroscopy is capable of probing short range structure not easily observed by PXRD, which more clearly probes long range order. Taking the Raman, PXRD and electrochemical data together, they indicate that nuclei of the orthorhombic phase begin to form even at $x = 0.05$, but are too small to produce well defined peaks in the PXRD data. The nuclei grow and are evident in PXRD data at the end of the plateau and beyond. Since the PXRD data exhibit expansion of the tetragonal phase up to the plateau onset at $x = 0.1$, we must assume that despite the formation of the orthorhombic phase, intercalation into the tetragonal phase continues. It may be that the surfaces of the growing nuclei or their interfaces with the parent, anatase, phase, contribute to the free energy of the system and permit a change in the composition of the tetragonal phase. Certainly changes of composition in two phase regions are not unprecedented, especially for nanomaterials.¹⁵⁷ However such a hypothesis requires detailed investigation by for example computational methods. Raman data after the onset of the plateau at $x = 0.12$ exhibit increasingly broadened peaks of lower intensity. This loss of intensity of all peaks continues along the plateau. Extraction of lithium reverses these processes which are repeated on subsequent cycling.

6.3 Electrochemical performance

Titanate anodes are employed because of their superior safety and ability to sustain high charge/discharge rates compared with graphite, features that are important for high power applications such as electric vehicles. Therefore we have investigated the rate capability of mesoporous anatase and compared it with the best performance reported for anatase in the literature, which was for 6 nm anatase nanoparticles.¹⁵⁶ Electrodes were prepared identically with the same mass loading of active material and the same 15 wt.% of carbon. However, in the case of the nanoparticulate anatase material, additional

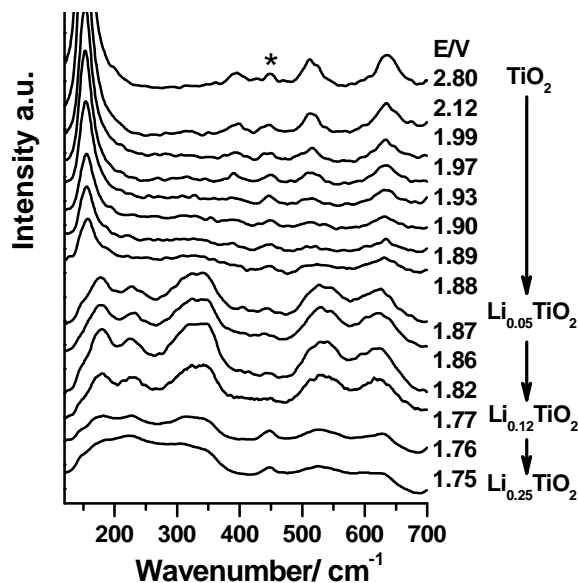


Figure 6-5 *In-situ* Raman spectral series during lithium insertion into anatase that shows the tetragonal to orthorhombic phase change. Spectra were taken at different positions along the discharge curve. Asterisk at 448 cm^{-1} indicates a band originating from the electrolyte.

electrodes were constructed with 45 wt.% of carbon (TiO_2 :SuperS:Kynar = 50:40:5) corresponding to the composition used in the literature report for 6 nm nanoparticulate anatase that showed the highest rate capability so far.¹⁵⁶ The results are reported in Fig. 6-6 where the capacities are plotted as a function of increasing rate. Considering first Fig. 6-6a where the capacities obtained on the first intercalation are normalized by the active mass, it is evident that the nanoparticulate material with 45 wt.% carbon exhibits a capacity that is slightly greater than the mesoporous material with only 15 wt.% carbon throughout the range of rates. However, nanoparticulate anatase with 15 wt.% carbon shows a dramatic decrease in capacity at high rates (greater than 1500 mA g^{-1}). The main conclusion from these results is that the 6 nm particles struggle to maintain satisfactory electron pathways through the electrode compared with the micron sized mesoporous materials. Much higher carbon contents are required in the case of the nanoparticulate material in order to exhibit high rate capability. When the capacity is normalized by the total electrode mass (Fig. 6-6b), the mesoporous material exhibits capacities that exceed the nanoparticulate material even with 45 wt.% carbon. Perhaps the most significant

result is seen in Fig. 6-6c where the capacity is normalized by the volume of the electrode. Volumetric capacity is increasingly recognized as an important parameter whether for consumer electronics or EV applications. The electrode volume is obtained directly by measuring the electrode thickness and knowing the electrode area. The mesoporous materials exhibit significantly higher volumetric capacities than the nanoparticulate materials, up to 2 times higher at the highest rates, despite the lower intrinsic density of mesoporous anatase.

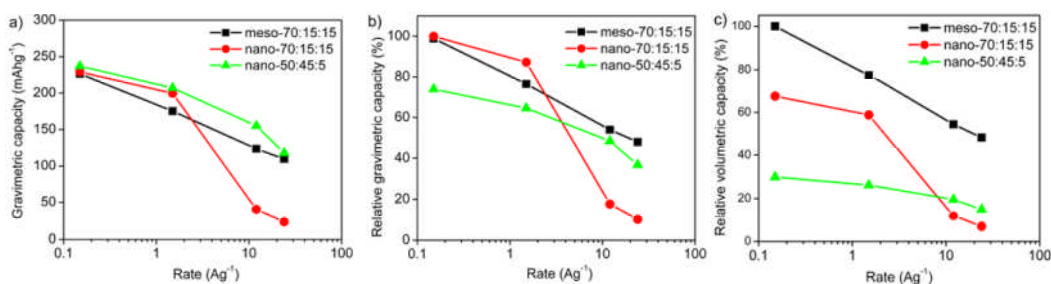


Figure 6-6 a) gravimetric capacity retention based on active mass, b) relative gravimetric capacity retention based on total electrode mass (including the mass of carbon and binder), and c) relative volumetric capacity retention based on total electrode volume, for mesoporous anatase (TiO_2 :Super S:Kyner = 70:15:15), and 6 nm anatase nanoparticle (TiO_2 :Super S:Kyner = 70:15:15 and 50:45:5).

Comparing the behavior of nanoparticle and ordered mesoporous anatase, both exhibit short diffusion distances for Li intercalation (6 nm diameter particles and 6.5 nm thick walls respectively) but:

1. It is difficult to pack nanoparticles efficiently into an electrode so they take up a relatively large volume. In contrast the mesoporous material is composed of micron sized particles that pack like dense micron sized particles.
2. In a nanoparticulate electrode, the porosity is located between the particles and is random in size, some voids being too small for electrolyte ingress and some too large. In the mesoporous phase, the pores are uniform in size and shape, as well as being connected in a continuous 3D network, thus facilitating electrolyte contact and hence maximizing the electrode/electrolyte contact area, without wasting volume.
3. The hierarchical pore structure will aid transport through the electrolyte.

4. More carbon is required to maintain electron pathways to the nm particles than is the case for micron sized particles. Carbon coating could be used to more efficiently distribute the conducting additive; although such methods, including the application of redox active molecules or conducting polymer layers, may add some complexity and cost to the electrodes.

The increase in capacity and reversibility that is often observed for 2-phase intercalation reactions on moving to the nanoscale is usually attributed to the ease of the 2-phase transformation in nanoparticles.^{155,157} However the mesoporous materials are micron sized particles with channels and hence an entire particle cannot transform spontaneously between phases, as has been proposed for nanoparticle anatase and LiFePO_4 .^{149,157} The nucleation front of a new phase (e.g. the orthorhombic phase that forms on intercalation) must spread across the particle. In the case studied here the walls of the mesopore are composed of nanodomains of anatase and they could spontaneously switch structures, with strain being relieved at the boundaries between the domains. A related process has been described before for LiMn_2O_4 derived from layered LiMnO_2 .^{160,161} Also the strain of the phase transition is relieved by the thin walls even if though switching of entire particles between phases cannot occur.

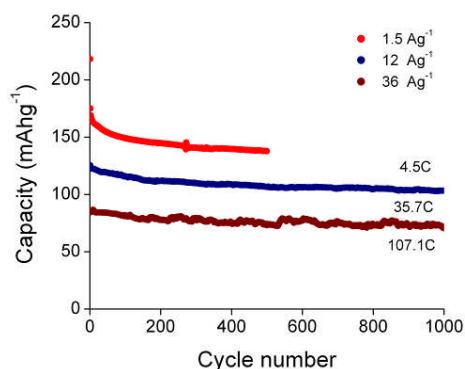


Figure 6-7 High-rate capacity retention for mesoporous anatase materials.

Comparing the results for ordered mesoporous anatase with those obtained previously for disordered mesoporous anatase, excellent rate performance was demonstrated in particular by Guo and Maier for the latter when it contained a metalized coating of RuO_2 . These elegant studies reported a capacity of 91 mAhg^{-1} at 10 Ag^{-1} .¹⁶² Interestingly, the ordered mesoporous anatase reported here shows even higher rate

performance of 125 mAhg^{-1} at 12 Ag^{-1} (35.7C , Fig. 6-7) without metallization. Of course there may be a number of reasons for these differences and it is difficult to establish clearly the origin without more detailed knowledge of the loading, electrode thickness etc. used in the previous work. However, it does suggest that electron transport (metalizing pore walls), although important, may not be the only rate limiting factor. We suggest that the ordered mesostructure may offer important advantages compared with disordered mesopores in achieving high rate performance. As stated above, all of the pores are of equal size, they are interconnected in a 3D array ensuring equal access of the electrolyte to the entire internal surface of the walls and the walls themselves are all equivalent. These features are not present in disordered mesoporous materials.

6.4 Conclusion

In conclusion, an ordered 3-dimensional mesoporous anatase have been synthesised using a hard template and lithium intercalation has also been investigated. The structural changes are similar to those observed for nanoparticles, with continuous Li insertion into tetragonal anatase up to $\text{Li}_{0.05}\text{TiO}_2$, then a 2-phase process between anatase and orthorhombic $\text{Li}_{0.45}\text{TiO}_2$ followed by continuous insertion into the orthorhombic phase up to $\text{Li}_{0.96}\text{TiO}_2$. Despite the intrinsic porosity of the mesoporous phase, the volumetric capacity is higher than the best results for nanoparticulate anatase reported previously, a 2 fold increase being observed at the highest rates (24 Ag^{-1}). The rate capability is better than disordered mesoporous anatase even when the latter is metalized, suggesting that the ordered pore structure is important in achieving high rate capability.

Chapter 7 Ordered crystalline mesoporous α -MnO₂

High surface area porous solids have impact on some of most important problems facing us presently—energy, greenhouse gas control, and novel catalysts for improved chemical processes.^{1,3,163-165} The distribution of pore sizes, shape, and volume in porous materials is directly related to their ability to perform the desired function in a particular application.³ For example, due to their pore size limitation (0.3-1.3 nm), zeolites often impose a diffusion limitation for catalytic applications involving large molecules.¹⁶⁶ In addition to this issue, effort has been devoted to preparing porous materials with a hierarchical pore structure, such as the synthesis of nano-crystalline zeolites containing open mesopores in the inter-crystalline void space,¹⁶⁷ synthesis of zeolites with mesopore-micropore hierarchical structures using hard templates,¹⁶⁸⁻¹⁷⁰ or the use of supramolecular soft templates to synthesize mesoporous materials with or without using ‘zeolitic nanoclusters’ precursor.¹⁷¹

For decades, manganese oxides have attracted much research interests due to their wide applications in batteries, catalysts, molecular sieves etc.¹⁷²⁻¹⁷⁶ Recently different ordered mesoporous manganese oxides, such as β -MnO₂, Mn₂O₃, Mn₃O₄, or Mn_xO_y have been prepared and used as electrode materials, catalysts, or magnetic materials.^{30,40,63,76,83,85,97} Previously we prepared mesoporous Fe₂O₃ with amorphous walls containing micropores by using decylamine as the template.¹⁷⁷ However, to the best of our knowledge, there are no reports of ordered crystalline mesoporous metal oxides with microporous walls. Here we describe, for the first time, the preparation of three dimensional ordered crystalline mesoporous α -MnO₂ (cryptomelane) with microporous wall, in which K⁺ and KIT-6 mesoporous silica act to template the micropores and mesopores, respectively, and they have an interesting trimodal pore size structure. (0.5, 3.4, and 11.4 nm)

7.12 Characterization of mesoporous α -MnO₂

7.1.1 TEM, XRD, N₂ adsorption

TEM data for mesoporous α -MnO₂, Fig. 1(a-c), demonstrate a highly ordered 3D pore structure, replicating that of KIT-6 (space group *Ia3d*).²⁸ From the TEM data, an a_0

lattice parameter of 23.0 nm for the mesostructure was extracted, in good agreement with the value obtained from the low angle powder X-ray diffraction (PXRD) data, $a_0 = 23.4$ nm. HRTEM images in Fig. 7-1 show that the walls are highly crystalline with a typical wall thickness of 7.8 nm. The lattice spacings of 6.93 Å and 3.11 Å, agree well with the values of 6.92 and 3.09 Å for the [110] and [310] planes of α -MnO₂ (ICDD No. 00-044-0141). The wide angle PXRD data matches well with the PXRD data for bulk α -MnO₂, Fig. 7-2(ii)a and (ii)b, confirming that the walls of the mesoporous material possess the α -MnO₂ structure.

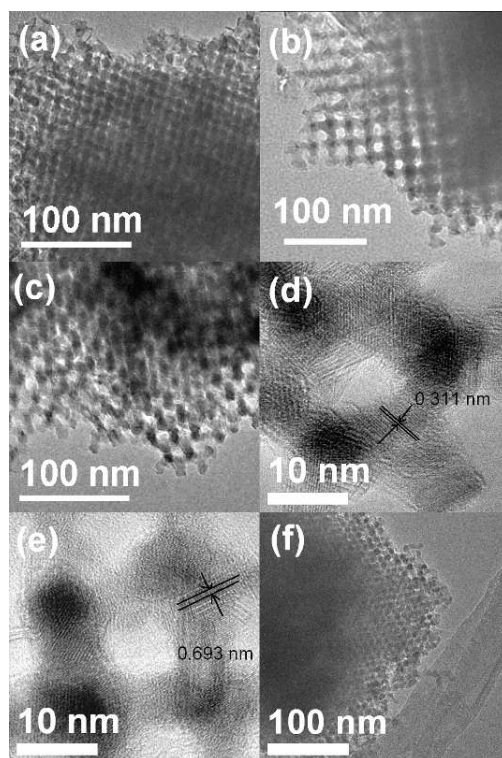


Figure 7-1 TEM images of mesoporous α -MnO₂ along (a) [110], (b) [100] (c) [111]; HRTEM images of mesoporous α -MnO₂, (d) and (e); TEM images of mesoporous α -MnO₂ (f) after 50 cycles.

Composition of the mesoporous α -MnO₂ ($K_{0.18}MnO_{2.06} \cdot 0.24H_2O$) and oxidation state of manganese (3.92) was obtained by atomic absorption, redox titration and TG analysis. The K⁺ cation sits in the 2×2 channel creating edge and corner sharing of MnO₆

octahedral (cryptomelane type structure).¹⁷⁸ Bulk α -MnO₂ has formula MnO₂·0.28H₂O, with no potassium ions present.

Further characterization of the mesostructure was carried out by N₂-sorption measurements (Fig. 7-3a), which show a type IV isotherm.¹⁵ The mesoporous α -MnO₂ shows an interesting trimodal pore size distribution—one micropore (0.50 nm) and other two mesopores (3.4 nm and 11.4 nm). By the H-K pore size distribution analysis (< 2 nm), mesoporous α -MnO₂ has a micropore size distribution peak at 0.50 nm (Fig. 7-3b), in good accordance with the 0.46 nm size of the 2×2 channel of the α -MnO₂.^{175,176} The BJH pore size distribution (for pore diameter > 1.7 nm), calculated from the desorption branch of the isotherm, exhibits a bimodal pore size distribution with one minor peak at 3.4 nm and the other strong peak at 11.4 nm. Such a bimodal pore size distribution in the mesopore range (2-50 nm) has been observed before for mesoporous metal oxides templated by gyroidal KIT-6 silica. The larger pore arise when the microporous bridges linking the two sets of pores in KIT-6 are broken, resulting in the filling of one or other set of pores but not both simultaneously.^{64,72,79} However, unlike previous examples, here the large pore size is dominant, indicating that many of the microporous bridges linking

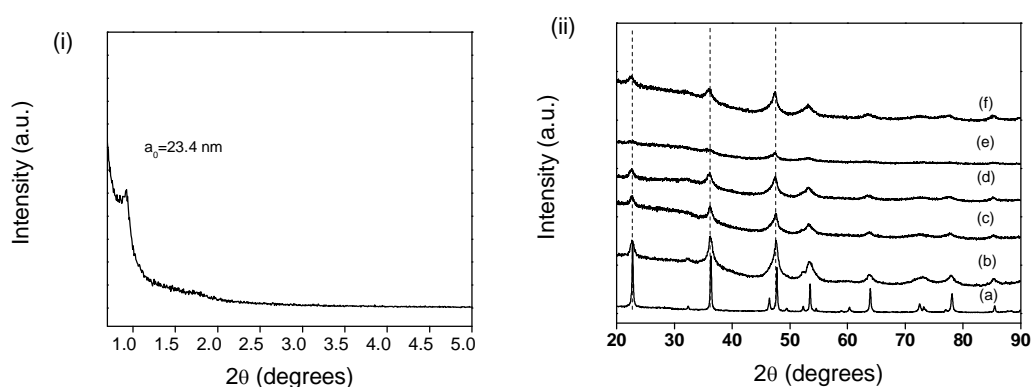


Figure 7-2 (i) Small-angle and (ii) wide-angle XRD pattern of mesoporous α -MnO₂. In (ii) the bulk α -MnO₂ was shown for comparison, (a) bulk α -MnO₂, (b) mesoporous α -MnO₂, (c) charged to 4.5 V on 1st cycle, (d) charged to 4.5 V on 32nd cycles, (e) discharged to 2.0 V on 1st cycle, and (f) discharged to 2.0 V on 32nd cycle.

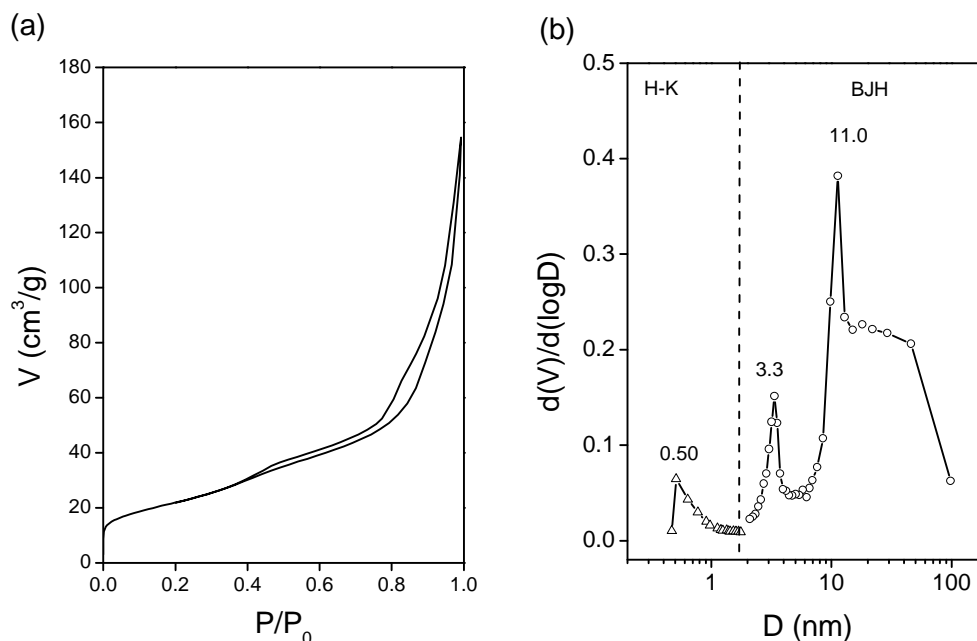


Figure 7-3 N₂ adsorption-desorption isotherms (a) and pore size distributions (b) for mesoporous α -MnO₂.

the two sets of pores in KIT-6 were broken, this may be due to the condensation of silica resulting from the presence of potassium. Alkaline (including Li⁺, Na⁺, K⁺, Rb⁺, Cs⁺) cations have been used to facilitate zeolite preparation. Since silica polymer was generally electric negative, the addition of cation could stabilize it by charge balance and favor polymerization of the silica fragment to give a molecular coherent unit of increased size. Such condensation of silica species by potassium was also observed in the preparation of mesoporous silica materials.¹⁷⁹ This hypothesis is supported by the lower K/Mn ratio of final product (*ca.* 1/5) compared with the starting materials (1/3). The BET surface area of mesoporous α -MnO₂ is 77 m²g⁻¹, with a pore volume of 0.23 cm³g⁻¹.

7.1.2 Characterization of microporosity by N₂ and CO₂ adsorption, and HRTEM

The microporosity of mesoporous α -MnO₂ was first analyzed by the t-plot method, which gave a micropore surface area of 6 m²g⁻¹. Using H-K pore size analysis (approach for pore size < 2 nm), mesoporous α -MnO₂ was shown to have a micropore size at 0.50 nm. The material also exhibited 3% CO₂ adsorption at low P/P₀ (0.03) and Langmuir

adsorption behavior (Fig. 7-4a), which is typical for microporous α -MnO₂.¹⁵ The detailed HRTEM analysis shows clear 2×2 channel directly, with some distorted channel structure.

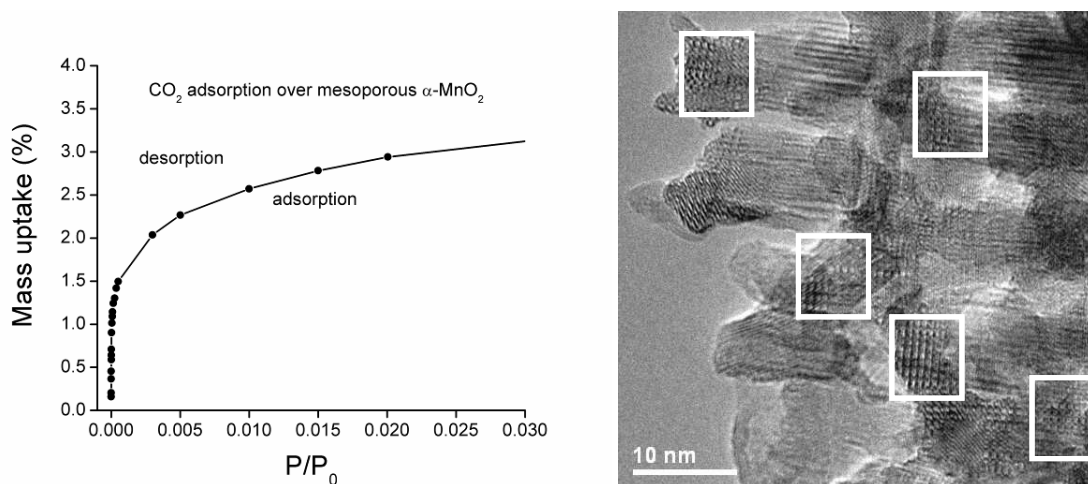


Figure 7-4 a, CO₂ adsorption, shows type I adsorption isotherm (Langmuir monolayer adsorption) at low pressure P/P_0 (< 0.03), corresponding to 3% of CO₂ uptake; b, HRTEM of mesoporous α -MnO₂, showing 2×2 micropore channels (0.46 nm × 0.46 nm) in white box.

7.1.3 Electrochemistry

Mesoporous α -MnO₂ was incorporated as the positive electrode in an electrochemical cell composed of a lithium metal counter/reference electrode and a non-aqueous lithium electrolyte. The cycling results are shown in Fig. 7-5, from which it is apparent that the material can deliver a high initial capacity of ca. 180 mAhg⁻¹ and, after some initial fade, can retain a capacity of 120 mAhg⁻¹ at a rate of 30 mA g⁻¹. The mesostructure is preserved throughout cycling, as demonstrated by the TEM data in Fig. 1(f). After 50 cycles of Li intercalation and deintercalation within the walls, the ordered mesostructure is clearly retained. Although bulk α -MnO₂ shows similar performance to mesoporous α -MnO₂ at low rates, e.g. 30 mA g⁻¹, it shows poor rate capability, with a capacity of only 20 mAhg⁻¹ at 1500 mA g⁻¹, while mesoporous α -MnO₂ shows excellent rate capability, with a stable discharge capacity of 90 mAhg⁻¹ even at a high rate of 6 000 mA g⁻¹.

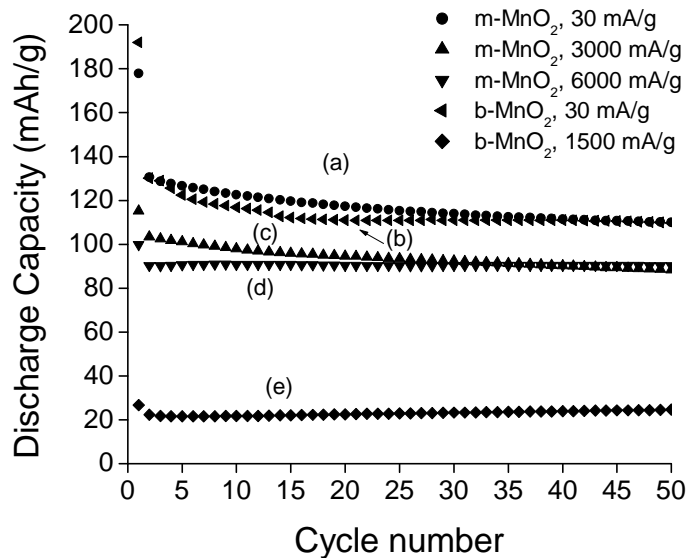


Figure 7-5 Capacity retention for mesoporous α -MnO₂ cycled at (a) 30 (●), (b) 3000 (▲), and (c) 6000 mA g⁻¹ (▼); bulk α -MnO₂ cycled at (d) 30 mA g⁻¹ (◄) and (e) 1500 mA g⁻¹ (◆).

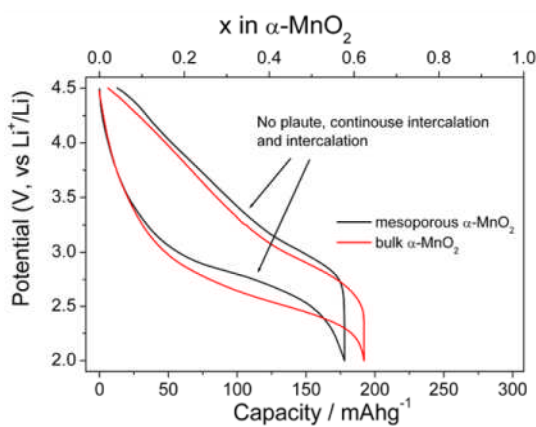


Figure 7-6 Variation of voltage with state of charge (capacity) for mesoporous α -MnO₂ on the first cycle.

The variation of voltage on discharge (Li intercalation) and charge (Li deintercalation) is shown in Fig. 7-6. The potential decreases continuously with no evidence of a plateau, characteristic of a single-phase reaction. In addition the profile is very similar to the bulk α -MnO₂. It is known that the intercalated Li is located in the 0.46 nm \times 0.46 nm 1D channels of α -MnO₂.¹⁷³ The PXRD patterns (Fig. 7-2(ii)) of the fresh,

charged (4.5 V) and discharged (2.0 V) samples were almost the same, confirming the single phase intercalation process. Mesoporous α -MnO₂ can be indexed on a tetragonal structure (space group I4/m) with $a = 9.866 \pm 0.005$, $c = 2.860 \pm 0.001$ Å. The lattice parameters change to $a = 9.926 \pm 0.011$ Å, $c = 2.859 \pm 0.010$ Å, and $a = 9.885 \pm 0.011$ Å, $c = 2.867 \pm 0.008$ Å for the fully-discharged and fully-charged mesoporous α -MnO₂ on the first cycle, respectively, corresponding to expansion along the a and b axis, and contraction along the c for Li insertion.¹⁷³ The unit lattice parameters of mesoporous α -MnO₂ after 32 cycles were similar to that of the 1st cycles.

Table 7-1 Unit cell lattice parameters for mesoporous α -MnO₂

Sample	a (Å)	c (Å)
As prepared α -MnO ₂	9.866±0.005	2.860±0.001
Discharged to 2.0 V, 1 cycles	9.926±0.011	2.859±0.010
Discharge to 2.0 V, 32 cycles	9.933±0.006	2.851±0.005
Charged to 4.5 V, 1 cycles	9.885±0.011	2.867±0.008
Charged to 4.5 V, 32 cycles	9.883±0.010	2.872±0.007

7.1.4 Magnetic properties

Magnetization dependence with temperature was performed on polycrystalline samples of mesoporous and bulk α -MnO₂ with a MPMS[®] Quantum Design SQUID magnetometer. Divergence between the zfc and fc susceptibilities can be seen in both samples (Fig. 7-7). The bulk system diverges at 46 K, whereas the mesoporous material demonstrates divergence at a higher temperature of 50 K.

Plots of $\chi_m T$ against T can yield information about the ordering temperature in these antiferromagnetic materials.¹⁸⁰ The ordering temperature is taken as the point at which the $\chi_m T$ slope is greatest. Néel transition temperatures (T_N) where the material changes from an antiferromagnet to a paramagnet are approximately 50 K for the bulk sample and 55 K for the mesoporous sample (Fig. 7-8). These are much higher than values estimated for 1-dimensional α -MnO₂ nanostructures (24-25 K),¹⁸¹ or single crystal needles (~25 K).¹⁸²

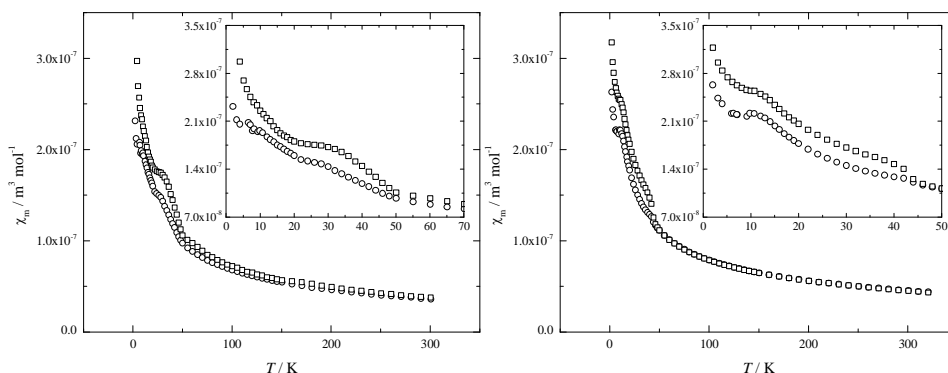


Figure 7-7 Zero field cooled (circles) and field cooled (squares) molar susceptibility (χ_m) of mesoporous (left) and bulk α -MnO₂ in 100 Oe (right). Inserts are magnifications of the zfc-fc divergence.

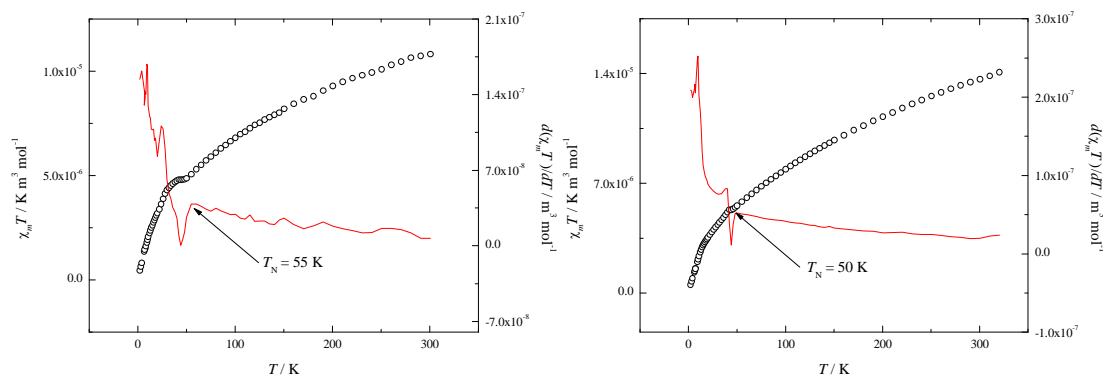


Figure 7-8 $\chi_m T$ plots against T for mesoporous α -MnO₂ (left) and bulk α -MnO₂ (right). The (red) lines are the gradient of the plots ($d\chi_m T/dT$), which indicate the Néel transition temperature by a sudden change in gradient upon cooling.

7.2 Conclusion

In conclusion, the first three dimensionally ordered crystalline mesoporous α -MnO₂ with microporous wall has been synthesized (cryptomelane). It has been used as a positive electrode in lithium battery and shows excellent rate capability—showing 91 mAhg⁻¹ at a rate of 6 000 mA g⁻¹. Its magnetic properties were also investigated.

Chapter 8 Ordered crystalline mesoporous Cu_xO exhibiting high NO storage capacity

Among the gas storage and delivery applications currently under investigation, nitric oxide (NO) show great promise for the development of new therapies for several different human diseases.¹⁸³ NO is critical to a number of biological processes including vasodilatation, anti-platelet activation, angiogenesis, collagen deposition and wound healing etc.¹⁸⁴ As a result it can play an important therapeutic role in medicine if a suitable medium for its storage and controlled release can be identified. One particularly promising method of delivering NO locally uses triggered release of gas stored in porous inorganic,¹⁸⁵ inorganic-organic hybrid^{186,187} or polymer materials.¹⁸⁸⁻¹⁹¹ In this chapter, the synthesis and characterization of a mesoporous CuO material, and the controlled reduction of such a material to form a mesoporous Cu-Cu₂O solid is first described. Then it is also demonstrated that both types of mesoporous solid have a competitively high adsorption, storage and release capacity for nitric oxide, and that the reduced Cu-Cu₂O material can be used both to store NO and to produce NO from nitrite substrates in large amounts.

8.1 Characterization of mesoporous Cu_xO by XRD, TEM, and N₂ adsorption

The preparation of the mesoporous materials are described in detail in Section 3.8 and 3.10. The small-angle PXRD pattern of mesoporous CuO (Fig. 8-1a) exhibits two peaks, the first of which can be indexed to the [211] reflection in space group *Ia3d*, corresponding to a unit cell parameter of 269 Å. The wide-angle PXRD pattern of mesoporous CuO (Fig. 8-1c) agrees well with the pattern of bulk CuO (Aldrich, 99.995%), except for some peak broadening due to the restricted dimension of the walls. While there is one example of a mesoporous CuO previously in the literature using mesoporous carbon as template,¹⁹² there are no examples of any reduced ordered copper-containing mesoporous oxides. Controlled reduction of the mesoporous CuO using H₂/Ar produces a mesoporous Cu-Cu₂O material. The small angle PXRD (Fig. 8-1b) indicates retention of the mesoporous structure, while the wide-angle PXRD pattern of mesoporous Cu-Cu₂O (Fig. 8-1d) exhibits diffraction peaks of Cu metal (the [111] and [200] reflections), along with a peak at 46.7° which could be assigned to the [111] diffraction peak of Cu₂O (46.3°).

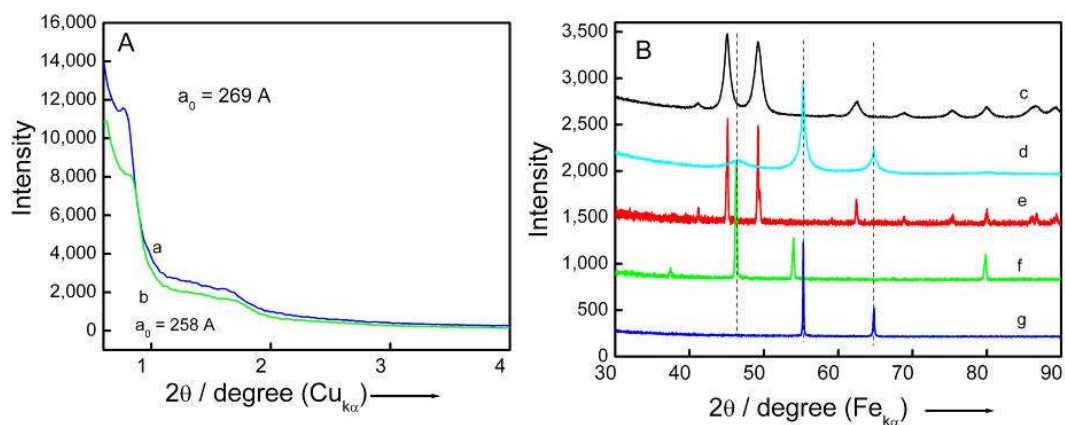


Figure 8-1 Powder X-ray diffraction patterns of crystalline mesoporous copper oxide. A, small angle X-ray diffraction patterns of a, mesoporous CuO; b, mesoporous Cu-Cu₂O. B, wide angle X-ray diffraction pattern of c, mesoporous CuO; d, mesoporous Cu-Cu₂O; e, bulk CuO; f, bulk Cu₂O; g, bulk Cu.

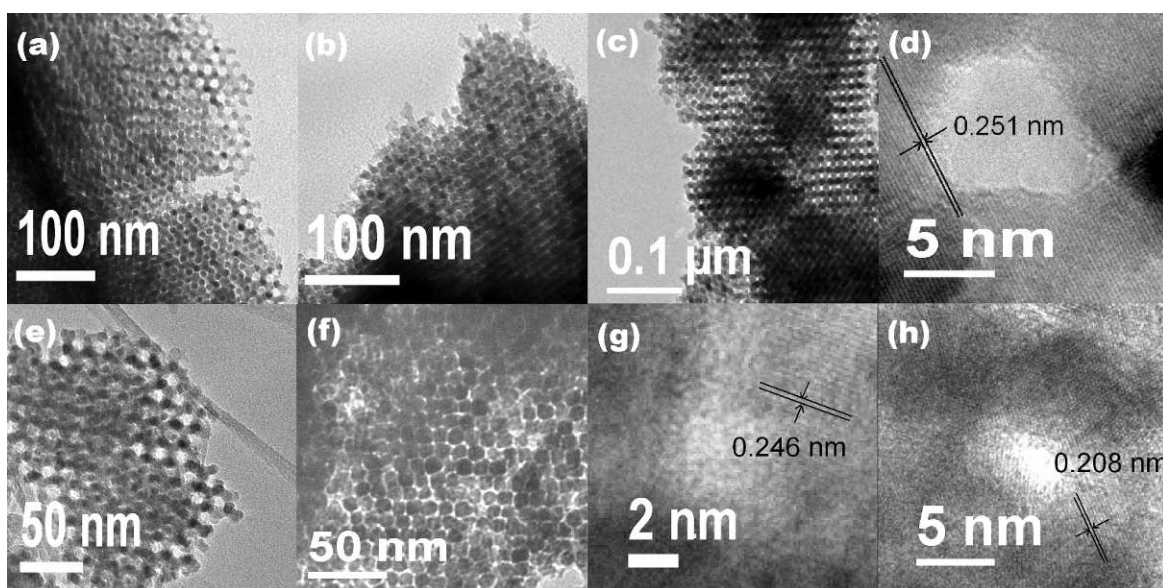


Figure 8-2 TEM images of mesoporous CuO (a-d) and mesoporous Cu-Cu₂O (e-h) by post-synthesis reduction from mesoporous CuO. (a), [111] direction of 3D meso-structure; (b), [310] direction of 3D meso-structure; (c), [110] direction of 3D meso-structure; (d), HRTEM of mesoporous CuO; (e) and (f), [111] direction of mesoporous Cu-Cu₂O; (g) and (h), HRTEM of mesoporous Cu-Cu₂O.

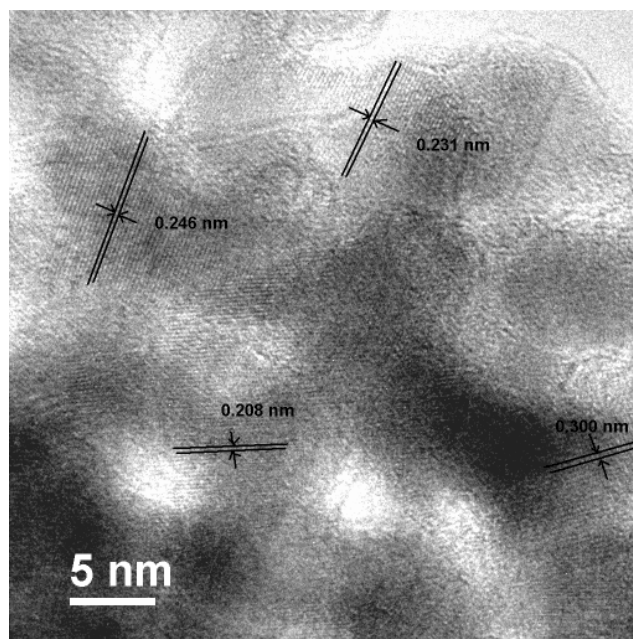


Figure 8-3 Typical HRTEM of mesoporous CuO after reduction in H₂/Ar at 180 °C for 1 h. The lattice spacing of 0.300 nm, 0.246 nm, 0.231 nm, and 0.208 nm, could be assigned to the (110) plane and (111) plane of Cu₂O (0.301 nm and 0.246 nm, ICDD No. 01-078-2076), (111) plane of CuO (0.232 nm, ICDD No. 00-048-1548), and (111) plane of Cu (0.208 nm, ICDD No. 00-001-1241). So three phases of CuO, Cu₂O, and Cu coexist.

Transmission electron micrographs of mesoporous CuO and Cu-Cu₂O are shown in Fig. 8-2. Both the mesoporous structures are highly ordered, with *Ia3d* symmetry, reflecting the mesostructure of the KIT-6 silica template. Fig. 8-2a shows a view of mesoporous CuO, down the [111] direction from which a unit cell parameter $a_0 = 270 \text{ \AA}$ was obtained, in good agreement with the a_0 of 269 \AA obtained from PXRD. The HRTEM of mesoporous CuO demonstrates directly its crystalline character, with a lattice spacing of 0.251 nm, which agrees well with the value of 0.252 nm for the $(1\bar{1}\bar{1})$ plane of CuO (ICDD No. 00-048-1548). From Fig. 8-2e, a unit cell parameter for the Cu-Cu₂O mesopore structure of $a_0 = 256 \text{ \AA}$ was obtained, which is in good agreement with $a_0 = 258 \text{ \AA}$, obtained from the PXRD data. The HRTEM of mesoporous Cu-Cu₂O also shows the presence of crystalline walls, with lattice spacings of 0.246 nm and 0.208 nm, in good accordance with the (111) plane of Cu₂O (0.246 nm, ICDD No. 01-078-2076) and (111) plane of Cu (0.208 nm, ICDD No. 00-001-1241) respectively. Reduction of mesoporous CuO results in mesoporous Cu-Cu₂O with an intergrowth structure.

Through detailed HRTEM analysis of the intermediate CuO reduction product (Fig. 8-3, reduction by 5% H₂-95% Ar at 180 °C for 1 h), it is found that in the intergrowth within one particle, the three phases, CuO, Cu₂O, and Cu, are evident. None of the reduction conditions used resulted in pure mesoporous Cu₂O—it is always present with CuO, Cu or both. Also, pure mesoporous Cu could not be obtained. Reduction to pure metallic Cu resulted in ultimately the formation of bulk Cu. This may be due to the ‘Tammann effect’, in which the surface of nanomaterials melts at temperatures much lower than the bulk. We suggest that Cu diffusion results in first the deformation of the mesostructure and then grain growth to form bulk copper ultimately.

In order to examine the pore size and its distribution in more detail, low temperature nitrogen adsorption and desorption measurements were performed (Fig. 8-4A). Mesoporous CuO and Cu-Cu₂O show typical type IV isotherms,¹⁵ which are similar to other crystalline mesoporous metal oxides obtained by hard templating. Also they exhibit a similar pore size of 3.8 nm and 3.6 nm respectively. Reduction induces a shrinkage of the pore structure. The pore size distribution of CuO is interestingly bimodal (Fig. 8-4B), with a narrow peak centered at 3.8 nm corresponding to the mesopores observed by TEMs in Fig. 8-2(a-c) and a wider peak center at 10.0 nm, which could be assigned to the filling of one or other set of KIT-6 pores but not both simultaneously (detailed discussion could be seen in final paragraph of Chapter 4).⁶⁴ The surface areas from the Brunauer-Emmett-Teller (BET) method are 171 m²·g⁻¹ for CuO and 50 m²·g⁻¹ for Cu-Cu₂O.

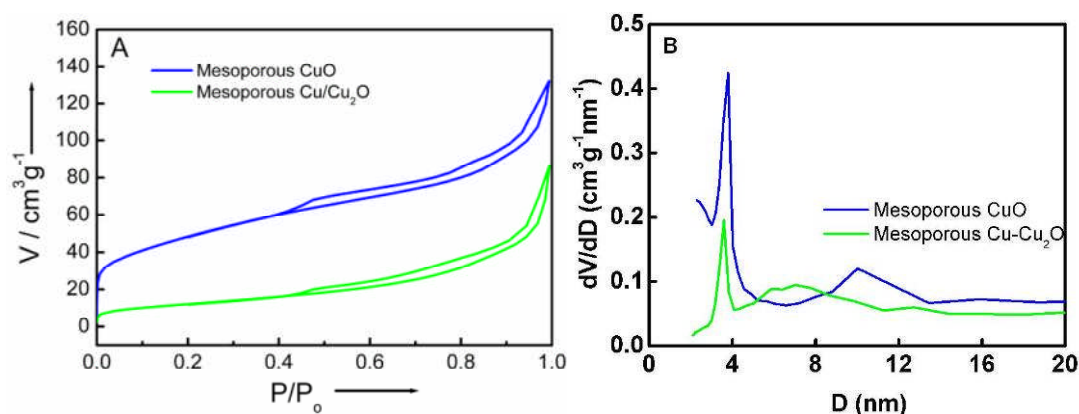


Figure 8-4 A, N₂ adsorption-desorption isotherms for mesoporous CuO and Cu-Cu₂O. B, the pore size distribution of mesoporous CuO and Cu-Cu₂O calculated from desorption branch by the BJH method.

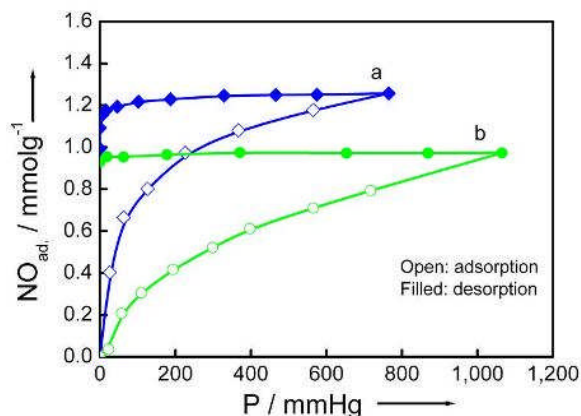


Figure 8-5 NO adsorption and desorption isotherms of mesoporous CuO and Cu-Cu₂O at 298 K. a, CuO; b, Cu-Cu₂O.

Table 8-1 Metal oxides prepared by using mesoporous silica as templates

Mesoporous metal oxide	D (nm)	V _p (cm ³ g ⁻¹)	S _{BET} (m ² g ⁻¹)	NO adsorption weight capacity (mmolg ⁻¹)
Co ₃ O ₄	3.5	0.17	98	0.583
Cr ₂ O ₃	3.4	0.14	93	0.8
CuO	3.8	0.186	171	1.256
Cu-Cu ₂ O	3.6	0.11	50	0.97
α-Fe ₂ O ₃	3.8	0.22	139	-
β-MnO ₂	3.3	0.20	121	-
Mn ₂ O ₃	3.7	0.19	119	-
Mn ₃ O ₄	3.7	0.20	100	-
NiO	3.8	0.30	94	-
CuO ^a	4.0	0.16	157	-
CuO ^b	3.9	0.17	148	-

^a Before NO adsorption and release; ^b After NO adsorption and release.

The partial radial distribution functions of EXAFS spectra for the mesoporous and bulk CuO are shown in Fig. 8-6. Generally, the agreement with the counterpart bulk phase is very good, distances for mesoporous CuO (bulk CuO in brackets) of Cu-O at 1.91 Å (1.94 Å), Cu-Cu at 2.90 Å (2.93 Å), Cu-Cu at 3.38 Å (3.38 Å), Cu-Cu at 3.92 Å (3.94 Å) and Cu-Cu at 5.83 Å (5.91 Å).¹⁹³ Differences in the region from 4.75 – 4.95 Å may reflect the structure on the

pore surfaces of mesoporous CuO. The BET surface areas and porosities of the different crystalline mesoporous materials are shown in Table 8-1.

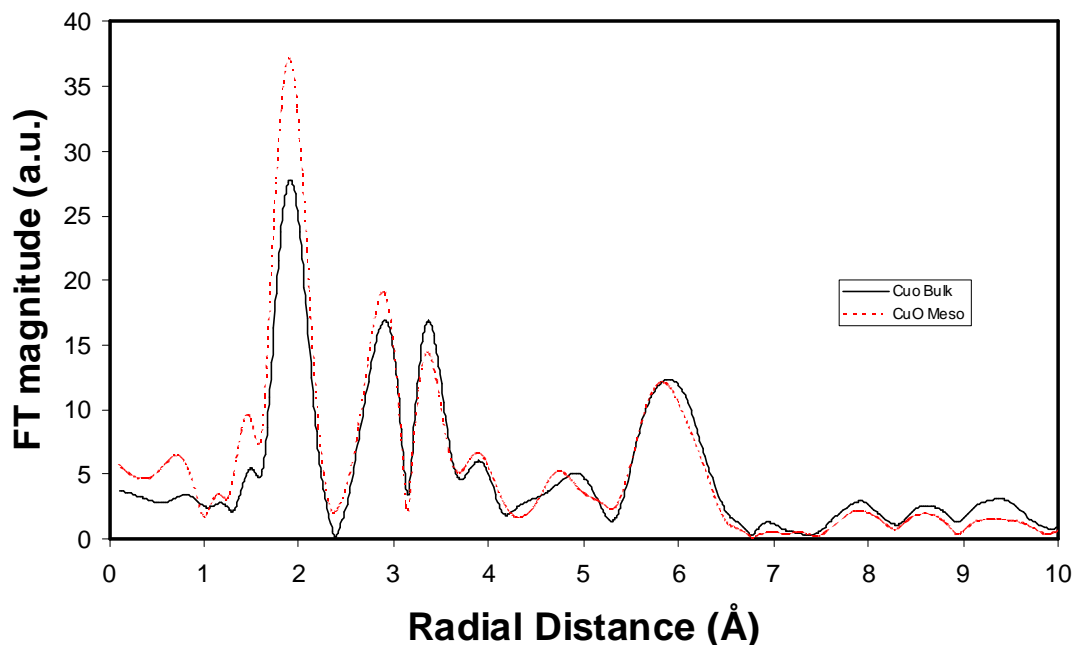


Figure 8-6 EXAFS analysis of mesoporous crystalline CuO-partial radial distribution functions (partial RDFs) obtained by Fourier transformation of the Cu K-EXAFS spectra.

8.2 NO adsorption and delivery

Turning to the NO adsorption by the mesoporous materials, various crystalline mesoporous metal oxides were examined for NO storage (Table 8-1). Less than half of them show any significant adsorption capacity. Mesoporous α -Fe₂O₃, β -MnO₂, Mn₂O₃, Mn₃O₄ and NiO essentially adsorb no nitric oxide. Cr₂O₃ and Co₃O₄ have modest but significant adsorption capacities of 0.12 mmol·g⁻¹ and 0.583 mmol·g⁻¹ respectively. However, the adsorption capacity of Cu-Cu₂O (0.97 mmol·g⁻¹) and CuO (1.25 mmol·g⁻¹) are much higher (Fig. 8-5). The adsorption capacity of crystalline mesoporous CuO and Cu-Cu₂O is comparable to that of some metal-containing zeolites,¹⁸⁵ many organic polymers¹⁹⁴⁻¹⁹⁶ and metal-containing polymers.¹⁹⁷ The NO adsorption/desorption isotherms of both CuO and Cu-Cu₂O show strong hysteresis on the desorption branch, indicative of strong interaction between the NO gas and the metal sites in the materials, as is expected given previous studies of NO in contact with

metal-containing zeolites and metal organic frameworks. The NO isotherms in Fig. 8-5 indicate that almost all the NO adsorption is retained even when the external pressure of NO is reduced. This is an excellent situation for NO storage materials, as it indicates that no release of the gas occurs without an external stimulus. Such strong interaction between NO and the metal ion in mesoporous CuO related materials accounts for the high efficiency of NO adsorption.

After NO adsorption and release for mesoporous CuO, the XRD pattern is still pure CuO phase, with no observable change (Fig. 8-7). The BET surface area was decreased by 5.7% after NO adsorption and release and the pore size was decreased by 0.1 nm (Table 8-1), probably due to the residue NO species. Both the crystalline structure and mesostructure of mesoporous CuO were retained.

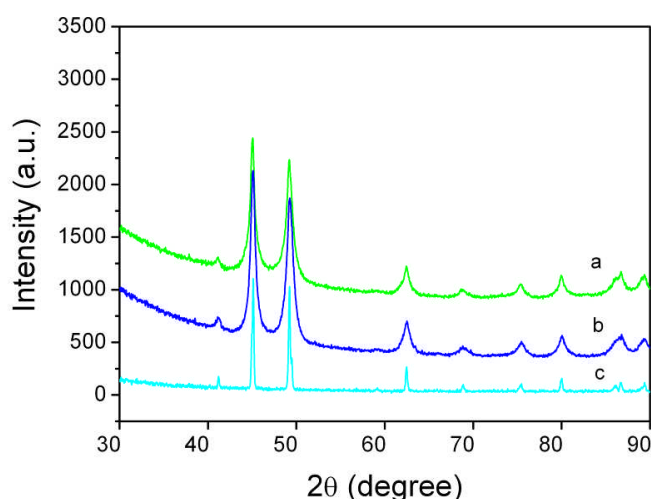


Figure 8-7 The powder XRD pattern of (a) mesoporous CuO, (b) mesoporous CuO after NO adsorption and release, and (c) bulk CuO (Aldrich, > 99.7%).

Of course, the adsorption capacity, while important, is not the only factor in determining the effectiveness of a material for NO storage. The potential usefulness of an NO storage material is governed by both the amount and rate of delivery of the gas. The rate of delivery must be in the range that is beneficial biologically – too little and there will be no effect and too much and there may be unintended reactions such as cytotoxicity. In the area of NO storage materials, exposure to water as a trigger for the release of the NO has been used. Both the NO-loaded CuO and NO-loaded Cu-Cu₂O release NO on exposure to a simulated physiological solution (MOPSO buffer pH 7.4) at 25 °C with a profile following that normally seen for NO releasing solids, a sharp burst of NO followed by a slowly decreasing amount, that falls to

approximately nil after several hours. A representative release profile for NO loaded Cu-Cu₂O is shown for the first 200 minutes in Fig. 8-8. The release profile indicates that NO is released in approximately similar amounts to materials that have shown biological activity previously. However, perhaps the most interesting feature of the Cu-Cu₂O mesoporous solid is the presence of copper (I) species. In recent years copper in its +1 oxidation state has been proved to be an excellent reagent for the reduction of the nitrite ion (NO₂⁻) to NO. Copper containing polymers¹⁹⁸ and zeolites¹⁹⁹ have both shown this effect, and there is speculation that such a reaction could be used to deliver NO at the surface of a material from a naturally occurring substrate like NO₂⁻ in a mimic of the natural enzymatic nitrite reductase mechanism.²⁰⁰

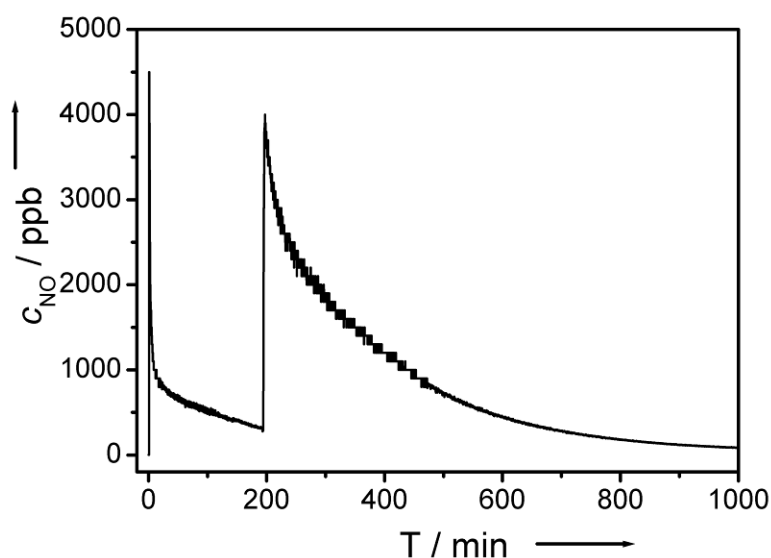


Figure 8-8 NO release and NO production from mesoporous Cu-Cu₂O. A sample of pre-loaded NO-Cu-Cu₂O releases the gas when exposed to a simulated physiological solution (MOPSO, pH = 7.4, total volume 2.6 mL). Addition of nitrite after $t = 200$ mins (NO₂⁻, concentration immediately after addition = 480 μ M) leads to a second burst of NO production indicative of the presence of significant amounts of Cu(I).

One of the drawbacks of the simple gas storage approach is that the reservoir of stored gas in a material is finite and is inevitably depleted as it is released for use. An alternative method of delivering an active gas by chemical production from a suitable substrate has the potential to significantly increase the capacity and lifetime of a gas-delivery material beyond what is possible with gas storage alone. When a small aliquot of sodium nitrite is added to the solution in contact with Cu-Cu₂O there is an immediate and sustained production of NO (Fig.8-

8). It is known that such a reaction depends on the presence of Cu(I), and this is confirmed by the fact that there is no production of NO when nitrite is added to the unreduced mesoporous CuO material. In addition, if the reduced Cu-Cu₂O material is left in air for a week, the NO production on addition of nitrite is significantly reduced, consistent with the expected increase in Cu(II) versus Cu(I) through aerial oxidation. The freshly prepared Cu-Cu₂O material produces 7.4×10^{-4} moles of NO per g of solid in the first 300 minutes after nitrite addition, while the aerially oxidized Cu-Cu₂O produced only about 40% of this amount, consistent with significant reduction of accessible Cu(I) species. The amount of NO produced on addition of nitrite to fresh Cu-Cu₂O is much greater than that produced by Cu(I) containing zeolites (5.7×10^{-5} mol NO per g solid under the same conditions), again consistent with the expected increase in accessible Cu(I) content of the Cu-Cu₂O material compared with the relatively dilute Cu(I) content in an aluminosilicate based zeolite. This increased NO production has an important consequence in that the exciting possibility of using the small naturally occurring reservoirs of nitrite as the substrate in the production of NO at the surface of, for example, a medical device as has been suggested by several workers, is significantly enhanced if the efficiency of the gas production reaction is high. This offers the possibilities of enhancing the lifetime of NO producing at least an order of magnitude beyond those possible with gas-storage materials alone.

8.3 Conclusion

In summary, in this chapter we have described the preparation and characterization of the first reduced mesoporous copper (I) oxide containing material, and demonstrated that both the oxidized CuO and reduced Cu-Cu₂O materials have competitively high storage capacities for nitric oxide. The reduced Cu-Cu₂O also shows extremely high NO production on exposure to nitrite ions – a feature that offers significant opportunities for the development of new NO production technologies, especially in *ex vivo* (e.g. anti-bacterial) applications where the potential toxicity of the copper-containing materials are mitigated.

Chapter 9 Catalytic CO oxidation by mesoporous metal oxides

Low-temperature CO oxidation is one of the most important topics in catalysis.²⁰¹ The pioneering work of Haruta and coworkers demonstrated excellent CO oxidation catalysed by finely dispersed gold nanoparticles.²⁰² However, because of the high cost of noble metals, cheaper metal oxide catalysts are being actively sought.²⁰³⁻²⁰⁸ Despite the high internal surface area of mesoporous transitional metal oxides, the redox activity of their surfaces and the confinement of reactions close to the surface due to the dimensions of the pores, investigation of ordered mesoporous metal oxides as CO oxidation catalysts has been limited, e.g., CuO/meso-CeO₂,⁶⁸ Pt/meso-Ce_{0.5}Zr_{0.5}O₂,¹¹⁷ and mesoporous Co₃O₄.¹¹⁸ Here a series of crystalline ordered mesoporous metal oxides were prepared and tested for CO oxidation.

9.1 Mesoporous metal oxides characterized by PXRD, TEM, and N₂ sorption

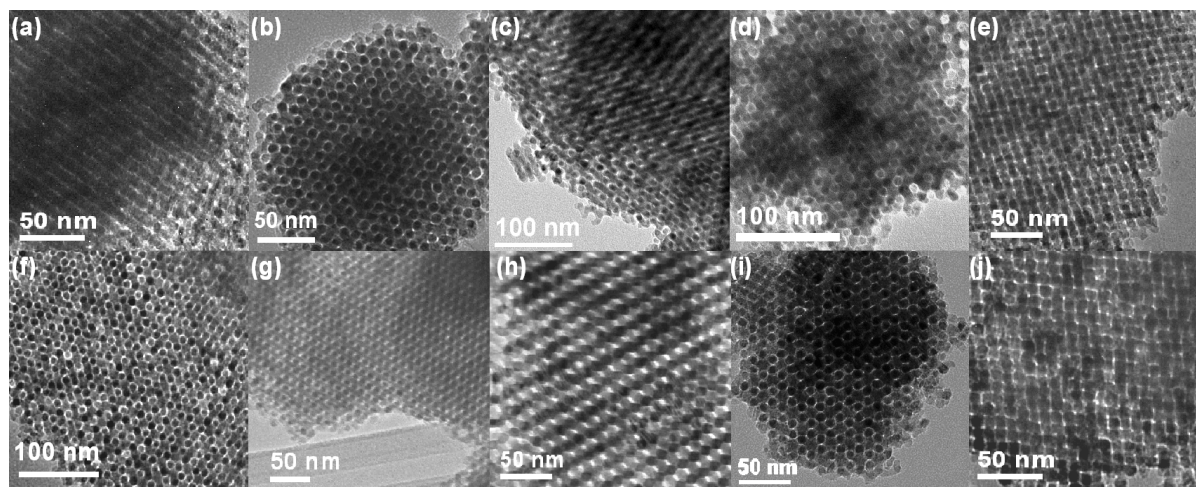


Figure 9-1 TEM images of ordered crystalline mesoporous metal oxides: (a) CeO₂, (b) Co₃O₄, (c) Cr₂O₃, (d) CuO, (e) Fe₂O₃, (f) β -MnO₂, (g) Mn₂O₃, (h) Mn₃O₄, (i) NiO, and (j) spinel NiCoMnO₄.

The formation of ordered mesoporous structures for all the mesoporous metal oxides was demonstrated by TEM (Fig. 9-1). The 3D pore structures replicate that of KIT-6 template with space group of *Ia3d*. The mesoporous structure is preserved throughout, as demonstrated by examining many different particles. The ordered mesostructures and crystalline nature of the walls of the mesoporous materials were confirmed by low and

wide-angle PXRD, respectively. As shown in Fig. 9-2, all mesoporous materials exhibit one relatively sharp peak below 1° , indexed as the 211 reflection in the $Ia3d$ space group. In Fig. 9-3, peaks corresponding to the crystalline metal oxides are clearly seen and are in good agreement with those for the corresponding bulk materials. Mesoporous spinel NiCoMnO_4 exhibits a PXRD pattern similar to Co_3O_4 spinel but with a different unit cell parameter.

The mesoporosity was further confirmed by N_2 adsorption-desorption measurements. Type IV isotherms were obtained for all the mesoporous metal oxide materials (Fig. 9-4), consistent with the mesoporosity observed by TEM and low angle PXRD. The Barrett-Joyner-Halenda (BJH) pore size distributions, calculated from the desorption branches, show a narrow distribution centred at 3.2-3.8 nm (Table 9-1) corresponding to the mesopores observed by TEM in Fig. 9-1. The BET surface areas of these mesoporous metal oxides are between 93 and 171 m^2/g (Table 9-1). For comparison, the BET surface areas of the bulk metal oxides used in this work are all below 9 m^2/g (Table 9-1).

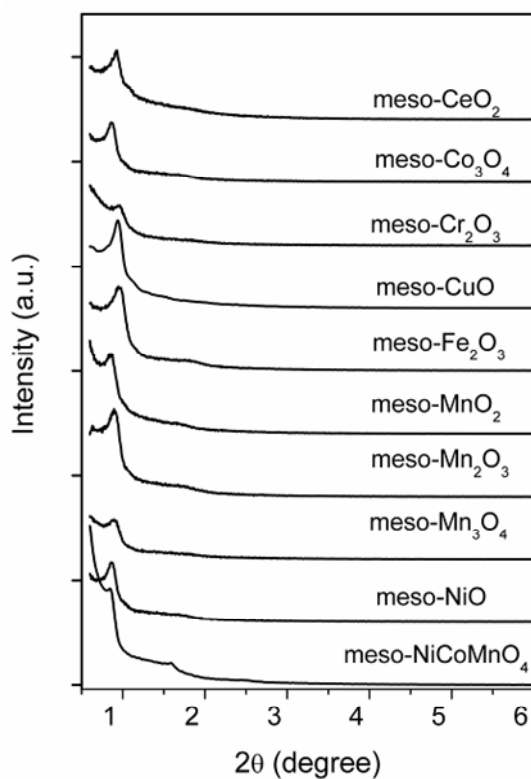


Figure 9-2 Low angle PXRD patterns of ordered crystalline mesoporous metal oxides.

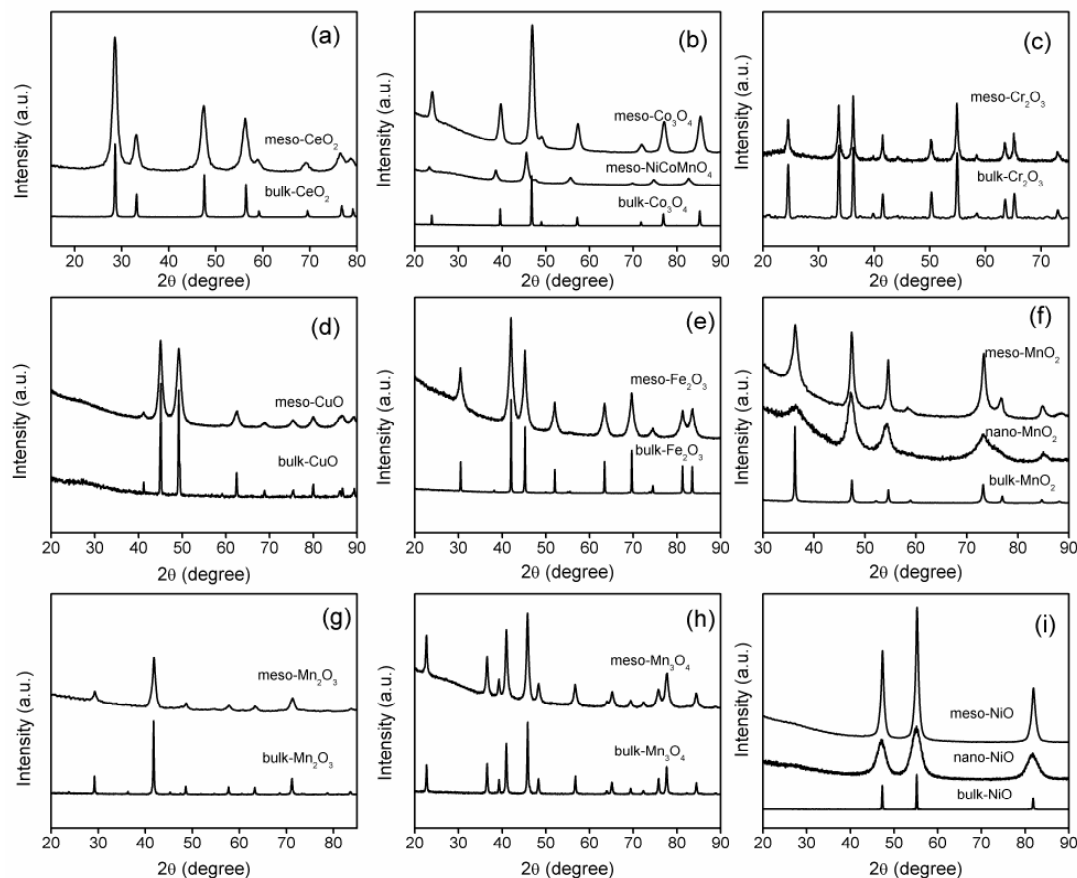


Figure 9-3 Wide-angle PXRD patterns of ordered crystalline mesoporous metal oxides: (a) CeO_2 , (b) Co_3O_4 and mesoporous spinel NiCoMnO_4 , (c) Cr_2O_3 , (d) CuO , (e) Fe_2O_3 , (f) MnO_2 , (g) Mn_2O_3 , (h) Mn_3O_4 , and (i) NiO . The PXRD patterns of corresponding bulk samples and MnO_2 and NiO nanoparticles are shown for comparison.

Table 9-1 Texture properties of mesoporous, bulk, and nanoparticles metal oxides determined by N_2 -sorption measurements

Metal oxide	Mesoporous		Nanoparticle	Bulk
	D_{BJH} (nm)	S_{BET} (m^2/g)	S_{BET} (m^2/g)	S_{BET} (m^2/g)
CeO_2	3.2	152	-	4.5
Co_3O_4	3.5	98	-	0.9
Cr_2O_3	3.4	93	-	3.0
CuO	3.8	171	-	1.3
$\alpha\text{-Fe}_2\text{O}_3$	3.8	139	-	8.6
$\beta\text{-MnO}_2$	3.3	121	162	0.5
Mn_2O_3	3.7	119	-	1.2
Mn_3O_4	3.7	100	-	5.2
NiCoMnO_4	3.7	99	-	-
NiO	3.8	94	170	4.7

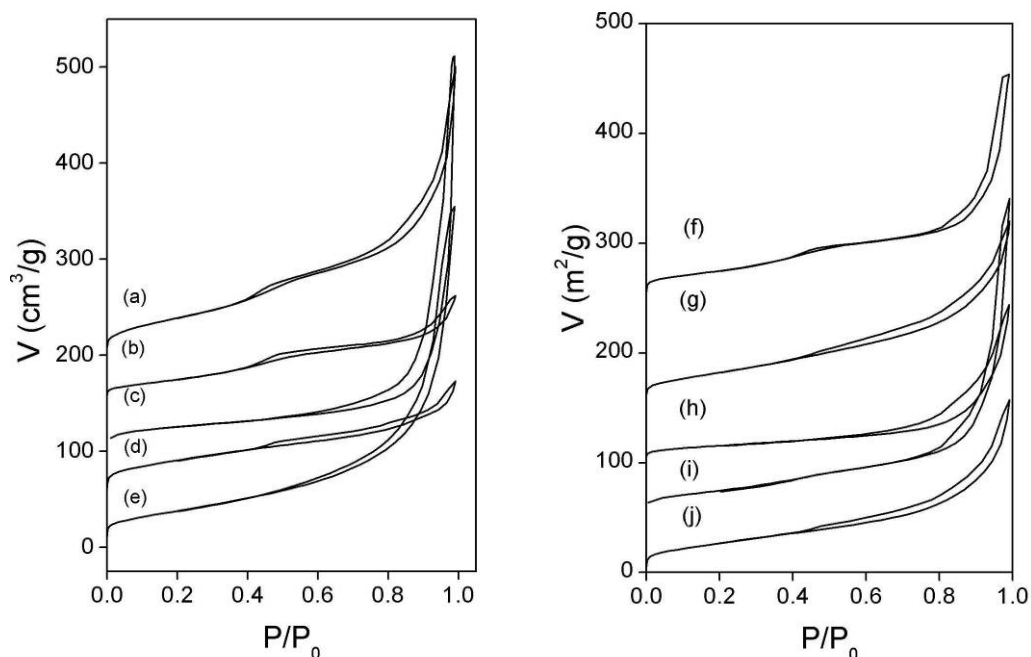


Figure 9-4 N₂ adsorption-desorption isotherms for the ordered crystalline mesoporous metal oxides: (a) CeO₂, (b) Co₃O₄, (c) Cr₂O₃, (d) CuO, (e) Fe₂O₃, (f) MnO₂, (g) Mn₂O₃, (h) Mn₃O₄, (i) NiO, and (j) spinel NiCoMnO₄. The isotherms for CeO₂, Co₃O₄, Cr₂O₃, CuO, Fe₂O₃, MnO₂, Mn₂O₃, Mn₃O₄, NiO, and spinel NiCoMnO₄ are offset vertically by 200, 150, 100, 50, 0, 250, 150, 100, 50, and 0 cm³/g, respectively for clarity of presentation.

9.2 Catalytic CO oxidation

The catalytic activities of the mesoporous metal oxides towards CO oxidation are shown in Fig. 9-5(a-b). These catalysts were all pretreated at 400 °C prior to testing. To compare the activities directly, the temperatures required for 50% CO conversion (T_{50}) are presented in Table 9-2, along with the values for the equivalent bulk phases, Fig. 9-4(c-d). Since the experimental conditions (i.e., catalyst amount, CO concentration, and flow rate) are the same, the lower the T_{50} value, the higher the catalytic activity.²⁰⁹

After being pretreated at 400 °C, all the mesoporous metal oxides except for Fe₂O₃ show much higher activity than the corresponding bulk materials. In particular, the T_{50} value for mesoporous NiO (39 °C) is over 100 °C lower than that of bulk NiO (143 °C), and the T_{50} values for mesoporous CeO₂ (203 °C), Co₃O₄ (-64 °C), Cr₂O₃ (147 °C), and β -MnO₂ (39 °C) are more than 200 °C lower than those of the corresponding bulk CeO₂ (>

430 °C), Co_3O_4 (201 °C), Cr_2O_3 (369 °C), and $\beta\text{-MnO}_2$ (397 °C). Amongst all these samples, crystalline mesoporous Co_3O_4 , $\beta\text{-MnO}_2$, and NiO show the highest activities, with T_{50} values of -64, 39, and 39 °C, respectively. There is a dip in the conversion curve of NiO, probably due to catalyst deactivation during reaction testing and/or operation of different reaction mechanisms in different temperature regions. The catalytic activity of mesoporous $\beta\text{-MnO}_2$ ($T_{50} = 39$ °C) is significantly higher than those of mesoporous Mn_2O_3 (107 °C), Mn_3O_4 (136 °C), and NiCoMnO_4 (114 °C), probably because of its higher oxidation state.

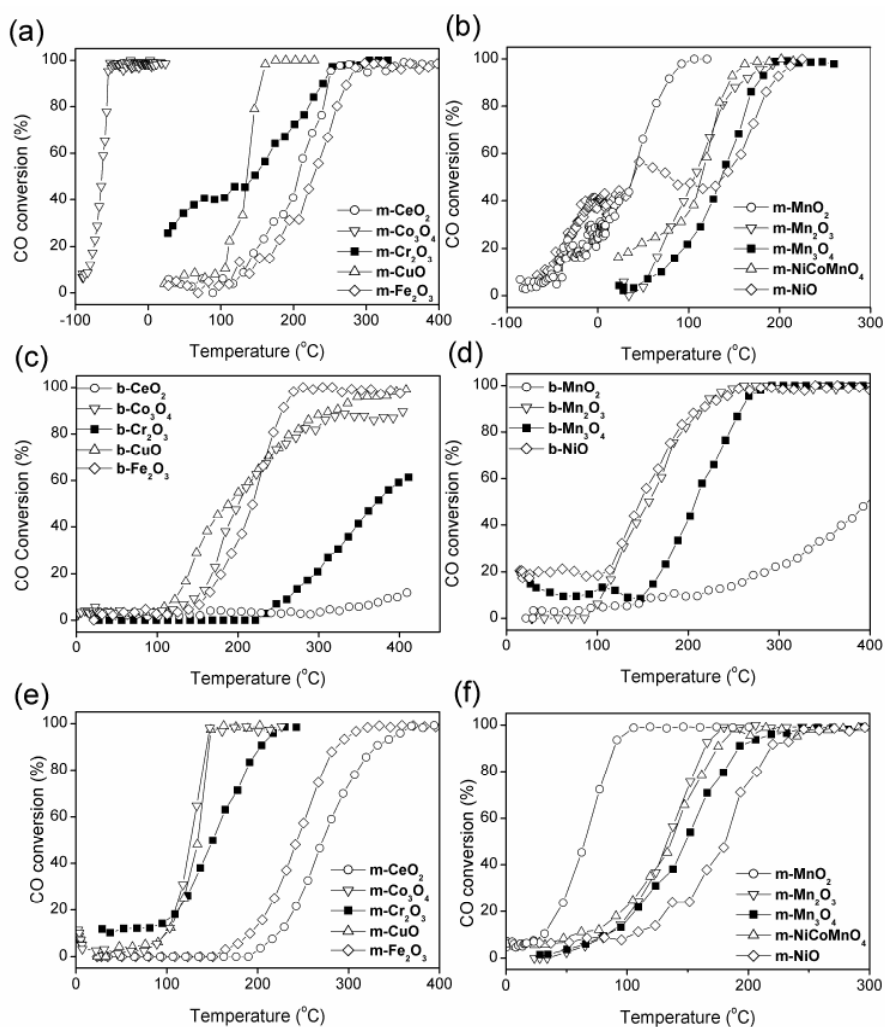


Figure 9-5 CO conversions on metal oxide catalysts: (a) and (b), mesoporous catalysts (denoted as m) pretreated at 400 °C; (c) and (d) bulk catalysts (denoted as b) pretreated at 400 °C; (e) and (f) mesoporous catalysts pretreated at 200 °C.

Table 9-2 T₅₀ values for metal oxide catalysts pretreated at 200 °C or 400 °C.

Metal oxide	T ₅₀ of metal oxides (°C)			
	200 °C-pretreated mesoporous	400 °C-pretreated mesoporous	400 °C-pretreated bulk	400 °C-pretreated nanoparticles
CeO ₂	272	203	> 430	-
Co ₃ O ₄	126	-64	201	-
Cr ₂ O ₃	151	147	369	-
CuO	134	136	190	-
α-Fe ₂ O ₃	244	227	218	-
β-MnO ₂	65	39	397	90
Mn ₂ O ₃	133	107	156	-
Mn ₃ O ₄	149	136	209	-
NiCoMnO ₄	137	114	-	-
NiO	181	39	143	135

To determine whether the high activities of our mesoporous samples are affected by the morphology, we prepared high-surface-area β-MnO₂ (162 m²/g) and NiO (170 m²/g) nanoparticles. Their catalytic activities, T₅₀ = 135 and 90 °C respectively, are higher than those of bulk β-MnO₂ and NiO, T₅₀ = 397 and 143 °C (surface areas 0.5 and 4.7 m²/g), but are still lower than those of mesoporous β-MnO₂ and NiO, T₅₀ = 39 and 39 °C, despite the lower surface areas of these mesoporous materials (121 and 94 m²/g), (Fig. 9-5). Evidently, the high surface area of mesoporous metal oxides is not the only reason for their high activities, and the mesoporous morphology is also important. We suggest three main reasons for the morphological enhancement.

- (i) Confinement of the gases close to the internal concave surfaces due to the size of the pores.
- (ii) Unlike a nanoparticulate powder, all of the surface is equally accessible because of the equal pore size.
- (iii) The pores are connected in three dimensional giving equivalent pathways for gas transport, unlike the random porosity between nanoparticles in a powder.

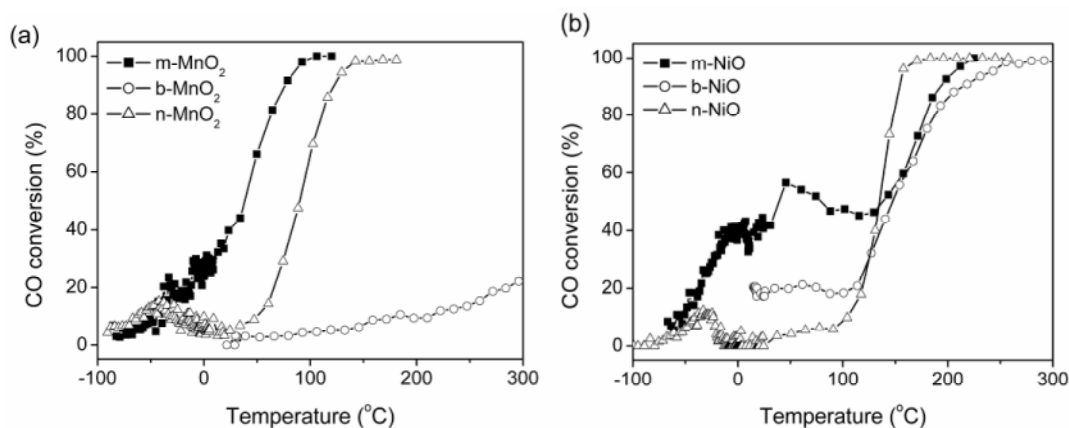


Fig. 9-6 Comparison of CO conversions on metal oxides of different morphologies pretreated at 400 °C: (a) mesoporous, bulk, and nanoparticle β -MnO₂; (b) mesoporous, bulk, and nanoparticle NiO.

Recently, Li et al. prepared a NiO nanoring structure which showed higher CO oxidation activity than the nanoparticles.²¹⁰ The authors attributed the high activity to the unique nanoring morphology, in agreement with our results.

In testing gas-phase catalytic reactions (e.g., CO oxidation), the catalyst should be pretreated at an elevated temperature to remove moisture and volatile contaminants, and the pretreatment temperature is normally higher than the reaction temperature. That is the reason why we pretreated the catalysts at 400 °C in the catalytic testing mentioned above. Since all mesoporous metal oxides show high activities well below 400 °C, we then attempted to pretreat these catalysts at a lower temperature (200 °C) to investigate the influence of pretreatment temperature.

As shown in Table 9-2, the T₅₀ values of 200 °C-pretreated mesoporous Cr₂O₃, CuO, α -Fe₂O₃, β -MnO₂, Mn₂O₃, Mn₃O₄, and NiCoMnO₄ are higher than those of the corresponding 400 °C-pretreated samples by 2-26 °C, demonstrating relative insensitivity to pretreatment temperature. β -MnO₂ exhibits the highest activity, higher than Co₃O₄ when pretreated at this temperature. The T₅₀ values of 200 °C-pretreated CeO₂, Co₃O₄, and NiO are higher than those pretreated at 400 °C by 69, 190, and 142 °C, respectively, indicating an obvious effect of pretreatment temperature. Therefore, we selected mesoporous Co₃O₄ and systematically studied the influence of pretreatment temperature on its activity.

As seen in Fig. 9-6a, mesoporous Co₃O₄ without pretreatment shows catalytic activity

only above 120 °C. When pretreated at 200 °C, it shows unstable activity below 0 °C (also observed for NiO pretreated at 400 °C), but remains inactive between 0 and 100 °C. Mesoporous Co_3O_4 had to be pretreated at 300-500 °C to obtain significant activity below 0 °C. Also, the low-temperature activity of the 500 °C-pretreated sample is unstable, decreasing dramatically above 0 °C, and cannot be restored by cooling the catalyst after the first test and re-recording the conversion curve afterwards. Therefore, the influence of pretreatment temperature on mesoporous Co_3O_4 is dramatic. In the literature, some reports indicate that pure Co_3O_4 is active for CO oxidation below ambient temperature,^{203,208} whereas others observed activities only at higher temperatures.²¹¹ Even the recent paper reporting high catalytic activity for mesoporous Co_3O_4 described its instability.¹¹⁸ Evidently the catalytic activity of Co_3O_4 is very sensitive to a number of factors and not yet well understood.

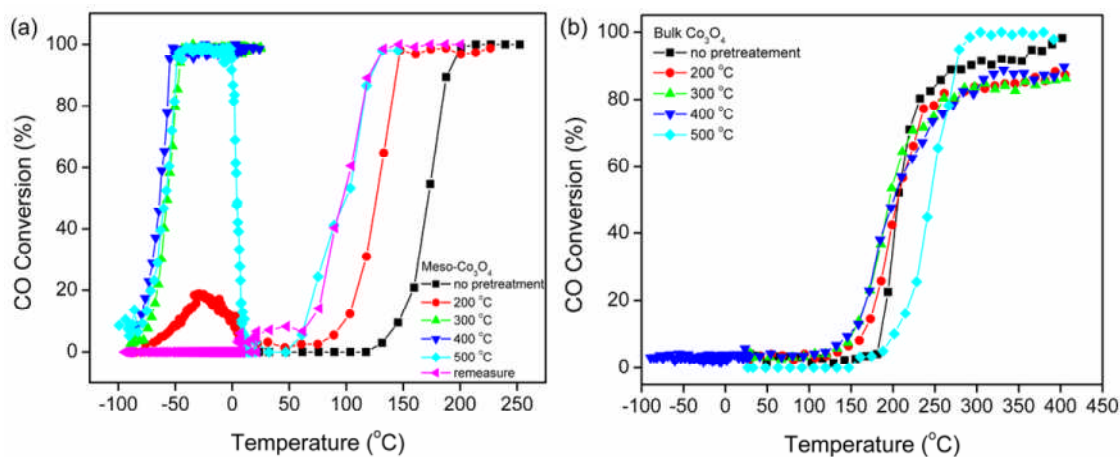


Figure 9-7 CO conversions on (a) mesoporous and (b) bulk Co_3O_4 samples pretreated under different temperatures.

To put our results in proper perspective, it is necessary to compare the catalytic data with those in the literature. Although the T_{50} value is a convenient index to compare quickly the catalytic activity under the same experimental conditions, it is not particularly well suited to compare the catalytic activities of different catalysts under different test conditions (e.g., amount of catalyst, CO concentration, and flow rate). Instead, specific rate offers a better means of comparison. Therefore, we selected several samples and compared their specific rates with the literature values, including in particular Co_3O_4 , because of its

high activity and β -MnO₂ because it is much cheaper, environmental-benign and more stable than Co₃O₄.

As shown in Table 9-3, the specific rate of our mesoporous CeO₂ at 220 °C is 12 mmol·g⁻¹·h⁻¹, much faster than that of commercial CeO₂ (0.7 mmol·g⁻¹·h⁻¹). This value is even higher than those achieved on highly active CeO₂ nanoparticles and nanorods reported in the literature (4.1-11 mmol·g⁻¹·h⁻¹).²¹²⁻²¹⁴ The specific rate of our mesoporous β -MnO₂ (17 mmol·g⁻¹·h⁻¹) at 80 °C indicates much higher activity than bulk β -MnO₂ (0.5 mmol·g⁻¹·h⁻¹) and β -MnO₂ nanocrystals reported in the literature (1.1 mmol·g⁻¹·h⁻¹)²¹⁵. The specific rate of our mesoporous Co₃O₄ (> 18 mmol·g⁻¹·h⁻¹) at -20 °C is at least 20 times faster than that of the recently reported mesoporous Co₃O₄ (0.8 mmol·g⁻¹·h⁻¹).¹¹⁸

9.3 Conclusions

To summarize, by studying a series of crystalline mesoporous metal oxides, we have been able to show that most but not all exhibit much higher catalytic activities than the corresponding bulk materials; with such activity being due to the mesoporous morphology, not just the high surface area. Mesoporous Co₃O₄, β -MnO₂, and NiO show appreciable CO conversions even below 0 °C. Although mesoporous Co₃O₄ exhibits the highest activity among the materials studied; when pretreated at 400 °C its activity is at least 20 times higher than that of mesoporous Co₃O₄ reported recently,¹¹⁸ its performance is very dependent on pretreatment temperature. Such instability makes mesoporous Co₃O₄ unattractive as a CO oxidation catalyst. In contrast, β -MnO₂ is the most active catalyst when pretreated at 200 °C and second only to Co₃O₄ when pretreated at 400 °C. It is cheap, environmentally benign and shows relative insensitivity to pretreatment temperature. Thus it is of potential interest for further studies as a CO oxidation catalyst.

In general terms, mesoporous metal oxides have been actively synthesized and characterized from a materials perspective,^{13,14,50} but reports on their catalytic applications are rather lacking. We believe that the current work may bridge such a gap. Although here we have selected CO oxidation as a probe reaction to demonstrate the catalytic application of mesoporous metal oxides, we believe that more studies on the catalytic applications of mesoporous metal oxides are certainly expected in the future.

Table 9-3 Comparison of specific rates of catalysts used in CO oxidation

Sample	Catalyst weight (g)	CO Concentration (%)	Flow rate (cm ³ min ⁻¹)	Reaction temperature (°C)	CO Conversion (%)	Specific rate (mmol g ⁻¹ h ⁻¹)	Reference
Mesoporous CeO ₂	0.05	1	37	220	67	12	This work
Bulk CeO ₂	0.05	1	37	220	4	0.7	This work
CeO ₂ nanoparticles	0.05	1	33.6	220	25	4.1	²¹⁴
CeO ₂ nanorods	0.05	1	33.6	220	20	3.3	²¹⁴
CeO ₂ nanocrystals	0.05	1	33.6	220	50	8.2	²¹³
CeO ₂ nanoparticles	0.2	1	100	220	42	5.2	²¹³
CeO ₂ nanorods	0.2	1	100	220	86	11	²¹²
Mesoporous β-MnO ₂	0.05	1	37	80	93	17	This work
Bulk β-MnO ₂	0.05	1	37	80	3	0.5	This work
β-MnO ₂ nanocrystals	0.15	1	100	80	7	1.1	²¹⁵
Mesoporous Co ₃ O ₄	0.05	1	37	-20	> 99	> 18	This work
Bulk Co ₃ O ₄	0.05	1	37	-20	4	0.7	This work
Mesoporous Co ₃ O ₄	0.2	1	60	-20	10	0.8	¹¹⁸

Chapter 10 Conclusions and future work

First, a new method of controlling the pore size and wall thickness of mesoporous silica was developed by controlling the calcination temperature. Such kind of KIT-6 silica materials obtained between 500 to 1000 °C have been used as hard templates to form the mesoporous metal oxide Co_3O_4 , with pore sizes and wall thicknesses within the ranges 3.7 to 11.9 nm and 2.2 to 8.2 nm respectively.

At the same time, by varying the silica template hydrothermal treatment temperature and using silica beads etc., we have prepared a series of positive electrodes based on mesoporous $\beta\text{-MnO}_2$ and used as the intercalation host, with pore sizes ranging from 3.4 to 28 nm in diameter, and wall thicknesses from 4.7 to 30 nm. So it has been possible to explore the influence of pore size and wall thickness on the rate of intercalation. The rate capabilities of both one and two-phase intercalation processes have been investigated by examining the first discharge (two phase) and tenth discharge (single phase) behavior, permitting comparison of the influence of the pore size/wall thickness between the two mechanisms. The pore size and wall thickness have a significant effect on the rate of lithium intercalation *via* single phase and two phase mechanisms. However the former requires more extreme variation in pore size/wall thickness to promote a change in rate than the latter.

An ordered 3D mesoporous anatase has been synthesized and its lithium intercalation as an anode material has also been investigated. The structural changes are similar to those observed for nanoparticles, with continuous Li insertion into tetragonal anatase up to $\text{Li}_{0.05}\text{TiO}_2$, then a 2-phase process between anatase and orthorhombic $\text{Li}_{0.45}\text{TiO}_2$ followed by continuous insertion into the orthorhombic phase up to $\text{Li}_{0.96}\text{TiO}_2$. Despite the intrinsic porosity of the mesoporous phase, the volumetric capacity is higher than the best results for nanoparticulate anatase reported previously, a 2 fold increase being observed at the highest rates (24 Ag^{-1}).

To the best of our knowledge, there are no reports of ordered crystalline mesoporous metal oxides with microporous walls. Here we describe, for the first time, the preparation of three dimensional ordered crystalline mesoporous $\alpha\text{-MnO}_2$ (cryptomelane) with microporous wall, in which K^+ and KIT-6 mesoporous silica act to template the micropores and mesopores, respectively. It has an interesting trimodal pore

size structure (0.5, 3.4, and 11.4 nm) with Langmuir CO₂ adsorption behavior at low P/P₀ (≤ 0.03). It has been used as a positive electrode in lithium battery and shows excellent rate capability-91 mAhg⁻¹ at a rate of 6 000 mA g⁻¹.

The preparation and characterization of mesoporous CuO and reduced Cu-Cu₂O has been described, and demonstrated that both the CuO and reduced Cu-Cu₂O materials have competitively high storage capacities for nitric oxide. The reduced Cu-Cu₂O also shows extremely high NO production on exposure to nitrite ions – a feature that offers significant opportunities for the development of new NO production technologies, especially in *ex vivo* (e.g. anti-bacterial) applications where the potential toxicity of the copper-containing materials are mitigated.

Finally by studying a series of crystalline mesoporous metal oxides (CeO₂, Co₃O₄, Cr₂O₃, CuO, Fe₂O₃, β -MnO₂, Mn₂O₃, Mn₃O₄, NiO, and spinel NiCoMnO₄), we have been able to show that most mesoporous metal oxide exhibit much higher catalytic activities than the corresponding bulk materials; with such activity being due to the mesoporous morphology, not just the high surface area. Mesoporous Co₃O₄, β -MnO₂, and NiO show appreciable CO conversions even below 0 °C.

In this thesis we have got quite a lot interesting properties of ordered mesoporous metal oxides and they demonstrate the potential for in industrial application. There are still quite a lot of applications and properties research could be carried on in the future based on current work. Mesoporous anatase could be used as a photocatalyst for dye-sensitised solar cells and organic molecules decomposition. Mesoporous manganese oxide (Mn₂O₃, Mn₃O₄, MnO₂) could also be used as supercapacitor. Mesoporous α -MnO₂ could be used as a heterogeneous catalyst for aerobic oxidation reaction due to its interesting micro-meso porosity. Besides, Li diffusion behavior in intercalated mesoporous Li_xMnO₂- β and Li_xTiO₂ is quite interesting. We could use dynamic solid state NMR to study Li⁺ diffusion in these electrode materials and probably could get some useful information to demonstrate the factor(s) which is related to their superior electrochemical performance. These information will help people to design better Li-ion batteries.

References

- (1) Corma, A. *Chem. Rev.* **1997**, *97*, 2373.
- (2) Schüth, F. *Chem. Mater.* **2001**, *13*, 3184.
- (3) Davis, M. E. *Nature* **2002**, *417*, 813.
- (4) Hartmann, M. *Chem. Mater.* **2005**, *17*, 4577.
- (5) Corma, A.; Diaz-Cabanas, M. J.; Jorda, J. L.; Martinez, C.; Moliner, M. *Nature* **2006**, *443*, 842.
- (6) Bruce, P. G.; Scrosati, B.; Tarascon, J. M. *Angew. Chem.-Int. Edit.* **2008**, *47*, 2930.
- (7) Kresge, C. T.; Leonowicz, M. E.; Roth, W. J.; Vartuli, J. C.; Beck, J. S. *Nature* **1992**, *359*, 710.
- (8) Yang, P. D.; Zhao, D. Y.; Margolese, D. I.; Chmelka, B. F.; Stucky, G. D. *Nature* **1998**, *396*, 152.
- (9) Ying, J. Y.; Mehnert, C. P.; Wong, M. S. *Angew. Chem. Int. Ed.* **1999**, *38*, 56.
- (10) Grosso, D.; Boissiere, C.; Smarsly, B.; Brezesinski, T.; Pinna, N.; Albouy, P. A.; Amenitsch, H.; Antonietti, M.; Sanchez, C. *Nat. Mater.* **2004**, *3*, 787.
- (11) Deshpande, A. S.; Pinna, N.; Smarsly, B.; Antonietti, M.; Niederberger, M. *Small* **2005**, *1*, 313.
- (12) Valdes-Solis, T.; Fuertes, A. B. *Mater. Res. Bull.* **2006**, *41*, 2187.
- (13) Tiemann, M. *Chem. Mater.* **2008**, *20*, 961.
- (14) Yang, H. F.; Zhao, D. Y. *J. Mater. Chem.* **2005**, *15*, 1217.
- (15) Sing, K. S. W.; Everett, D. H.; Haul, R. A. W.; Moscou, L.; Pierotti, R. A.; Rouquerol, J.; Siemieniewska, T. *Pure Appl. Chem.* **1985**, *57*, 603.
- (16) Taramasso, M.; Perego, G.; Notar, B. US patent, 1983; Vol. 4410501.
- (17) Beck, J. S.; Vartuli, J. C.; Roth, W. J.; Leonowicz, M. E.; Kresge, C. T.; Schmitt, K. D.; Chu, C. T. W.; Olson, D. H.; Sheppard, E. W.; McCullen, S. B.; Higgins, J. B.; Schlenker, J. L. *J. Am. Chem. Soc.* **1992**, *114*, 10834.
- (18) Antonietti, M.; Ozin, G. A. *Chem. Eur. J.* **2004**, *10*, 29.
- (19) Huo, Q. S.; Margolese, D. I.; Ciesla, U.; Feng, P. Y.; Gier, T. E.; Sieger, P.; Leon, R.; Petroff, P. M.; Schuth, F.; Stucky, G. D. *Nature* **1994**, *368*, 317.
- (20) Tanev, P. T.; Pinnavaia, T. J. *Science* **1995**, *267*, 865.
- (21) Zhao, D. Y.; Feng, J. L.; Huo, Q. S.; Melosh, N.; Fredrickson, G. H.; Chmelka, B. F.; Stucky, G. D. *Science* **1998**, *279*, 548.
- (22) Kruk, M.; Jaroniec, M.; Ko, C. H.; Ryoo, R. *Chem. Mater.* **2000**, *12*, 1961.
- (23) Ryoo, R.; Ko, C. H.; Kruk, M.; Antochshuk, V.; Jaroniec, M. *J. Phys. Chem. B* **2000**, *104*, 11465.
- (24) Jun, S.; Joo, S. H.; Ryoo, R.; Kruk, M.; Jaroniec, M.; Liu, Z.; Ohsuna, T.; Terasaki, O. *J. Am. Chem. Soc.* **2000**, *122*, 10712.
- (25) Kim, T. W.; Kleitz, F.; Paul, B.; Ryoo, R. *J. Am. Chem. Soc.* **2005**, *127*, 7601.
- (26) Liu, X. Y.; Tian, B. Z.; Yu, C. Z.; Gao, F.; Xie, S. H.; Tu, B.; Che, R. C.; Peng, L. M.; Zhao, D. Y. *Angew. Chem. Int. Ed.* **2002**, *41*, 3876.
- (27) Flodstrom, K.; Alfredsson, V.; Kallrot, N. *J. Am. Chem. Soc.* **2003**, *125*, 4402.
- (28) Kleitz, F.; Choi, S. H.; Ryoo, R. *Chem. Commun.* **2003**, 2136.

- (29) Sakamoto, Y.; Kim, T. W.; Ryoo, R.; Terasaki, O. *Angew. Chem. Int. Ed.* **2004**, *43*, 5231.
- (30) Tian, B. Z.; Liu, X. Y.; Solovyov, L. A.; Liu, Z.; Yang, H. F.; Zhang, Z. D.; Xie, S. H.; Zhang, F. Q.; Tu, B.; Yu, C. Z.; Terasaki, O.; Zhao, D. Y. *J. Am. Chem. Soc.* **2004**, *126*, 865.
- (31) Armatas, G. S.; Kanatzidis, M. G. *Nat. Mater.* **2009**, *8*, 217.
- (32) Sayari, A.; Liu, P. *Microporous Mater.* **1997**, *12*, 149.
- (33) Soler-illia, G. J. D.; Sanchez, C.; Lebeau, B.; Patarin, J. *Chem. Rev.* **2002**, *102*, 4093.
- (34) De Vos, D. E.; Dams, M.; Sels, B. F.; Jacobs, P. A. *Chem. Rev.* **2002**, *102*, 3615.
- (35) Ciesla, U.; Schuth, F. *Micropor. Mesopor. Mater.* **1999**, *27*, 131.
- (36) Antonelli, D. M.; Ying, J. Y. *Curr. Opin. Colloid Interface Sci.* **1996**, *1*, 523.
- (37) Antonelli, D. M.; Nakahira, A.; Ying, J. Y. *Inorg. Chem.* **1996**, *35*, 3126.
- (38) Brinker, C. J.; Lu, Y. F.; Sellinger, A.; Fan, H. Y. *Adv. Mater.* **1999**, *11*, 579.
- (39) Antonelli, D. M.; Ying, J. Y. *Angew. Chem., Int. Ed.* **1995**, *34*, 2014.
- (40) Tian, Z. R.; Tong, W.; Wang, J. Y.; Duan, N. G.; Krishnan, V. V.; Suib, S. L. *Science* **1997**, *276*, 926.
- (41) Smarsly, B.; Antonietti, M. *Eur. J. Inor. Chem.* **2006**, 1111.
- (42) Martin, M. E.; Narske, R. M.; Klabunde, K. J. *Micropor. Mesopor. Mat.* **2005**, *83*, 47.
- (43) Zelenski, C. M.; Dorhout, P. K. *J. Am. Chem. Soc.* **1998**, *120*, 734.
- (44) Shin, H. J.; Ryoo, R.; Liu, Z.; Terasaki, O. *J. Am. Chem. Soc.* **2001**, *123*, 1246.
- (45) Ryoo, R.; Joo, S. H.; Jun, S. *J. Phys. Chem. B* **1999**, *103*, 7743.
- (46) Kruk, M.; Jaroniec, M.; Ryoo, R.; Joo, S. H. *J. Phys. Chem. B* **2000**, *104*, 7960.
- (47) Shin, H. J.; Ryoo, R.; Kruk, M.; Jaroniec, M. *Chem. Commun.* **2001**, 349.
- (48) Che, S. N.; Lund, K.; Tatsumi, T.; Iijima, S.; Joo, S. H.; Ryoo, R.; Terasaki, O. *Angew. Chem. Int. Ed.* **2003**, *42*, 2182.
- (49) Kondo, J. N.; Domen, K. *Chem. Mater.* **2008**, *20*, 835.
- (50) Lu, A. H.; Schuth, F. *Adv. Mater.* **2006**, *18*, 1793.
- (51) Schuth, F. *Angew. Chem. Int. Ed.* **2003**, *42*, 3604.
- (52) Zhu, K. K.; Yue, B.; Zhou, W. Z.; He, H. Y. *Chem. Commun.* **2003**, 98.
- (53) Tian, B. Z.; Liu, X. Y.; Yang, H. F.; Xie, S. H.; Yu, C. Z.; Tu, B.; Zhao, D. Y. *Adv. Mater.* **2003**, *15*, 1370.
- (54) Zhu, K. K.; He, H. Y.; Xie, S. H.; Zhang, X.; Zhou, W. Z.; Jin, S. L.; Yue, B. *Chem. Phys. Lett.* **2003**, *377*, 317.
- (55) Yue, B.; Tang, H. L.; Kong, Z. P.; Zhu, K.; Dickinson, C.; Zhou, W. Z.; He, H. Y. *Chem. Phys. Lett.* **2005**, *407*, 83.
- (56) Jiao, F.; Yue, B.; Zhu, K. K.; Zhao, D. Y.; He, H. Y. *Chem. Lett.* **2003**, *32*, 770.
- (57) Wang, Y. Q.; Yang, C. M.; Schmidt, W.; Spliethoff, B.; Bill, E.; Schuth, F. *Adv. Mater.* **2005**, *17*, 53.

- (58) Jiao, K.; Zhang, B.; Yue, B.; Ren, Y.; Liu, S. X.; Yan, S. R.; Dickinson, C.; Zhou, W. Z.; He, H. Y. *Chem. Commun.* **2005**, 5618.
- (59) Jiao, F.; Shaju, K. M.; Bruce, P. G. *Angew. Chem. Int. Ed.* **2005**, *44*, 6550.
- (60) Yue, W.; Zhou, W. Z. *Chem. Mater.* **2007**, *19*, 2359.
- (61) Laha, S. C.; Ryoo, R. *Chem. Commun.* **2003**, 2138.
- (62) Bao, R. L.; Jiao, K.; He, H. Y.; Zhuang, J. H.; Yue, B. *Stud. Surf. Sci. Catal.* **2006**, *165*, 267.
- (63) Ren, Y.; Ma, Z.; Qian, L. P.; Dai, S.; He, H. Y.; Bruce, P. G. *Catal. Lett.* **2009**, *131*, 146.
- (64) Dickinson, C.; Zhou, W. Z.; Hodgkins, R. P.; Shi, Y. F.; Zhao, D. Y.; He, H. Y. *Chem. Mater.* **2006**, *18*, 3088.
- (65) Wang, Y. G.; Yuan, X. H.; Liu, X. H.; Ren, J. W.; Tong, W. Y.; Wang, Y. Q.; Lu, G. Z. *Solid State Sci.* **2008**, *10*, 1117.
- (66) Wang, Y. G.; Wang, Y. Q.; Liu, X. H.; Guo, Y.; Guo, Y. L.; Lu, G. Z.; Schuth, F. *J. Nanosci. Nanotechnol.* **2008**, *8*, 5652.
- (67) Rossinyol, E.; Arbiol, J.; Peiro, F.; Cornet, A.; Morante, J. R.; Tian, B.; Bo, T.; Zhao, D. *Sensor Actuat. B-Chem.* **2005**, *109*, 57.
- (68) Shen, W. H.; Dong, X. P.; Zhu, Y. F.; Chen, H. R.; Shi, J. L. *Micropor. Mesopor. Mat.* **2005**, *85*, 157.
- (69) Roggenbuck, J.; Schafer, H.; Tsoncheva, T.; Minchev, C.; Hanss, J.; Tiemann, M. *Micropor. Mesopor. Mat.* **2007**, *101*, 335.
- (70) Yue, W. B.; Zhou, W. Z. *J. Mater. Chem.* **2007**, *17*, 4947.
- (71) Zhu, J. K.; Gao, Q. M.; Chen, Z. *Appl. Catal. B-Environ.* **2008**, *81*, 236.
- (72) Jiao, F.; Hill, A. H.; Harrison, A.; Berko, A.; Chadwick, A. V.; Bruce, P. G. *J. Am. Chem. Soc.* **2008**, *130*, 5262.
- (73) Prim, A.; Pellicer, E.; Rossinyol, E.; Peiro, F.; Cornet, A.; Morante, J. R. *Adv. Funct. Mater.* **2007**, *17*, 2957.
- (74) An, Z.; He, J.; Shu, X.; Wu, Y. X. *Chem. Commun.* **2009**, 1055.
- (75) Waitz, T.; Wagner, T.; Sauerwald, T.; Kohl, C. D.; Tiemann, M. *Adv. Funct. Mater.* **2009**, *19*, 653.
- (76) Tian, B. Z.; Liu, X. Y.; Yang, H. F.; Xie, S. H.; Yu, C. Z.; Tu, B.; Zhao, D. Y. *Adv. Mater.* **2003**, *15*, 1370.
- (77) Jiao, F.; Harrison, A.; Jumas, J. C.; Chadwick, A. V.; Kockelmann, W.; Bruce, P. G. *J. Am. Chem. Soc.* **2006**, *128*, 5468.
- (78) Jiao, F.; Jumas, J. C.; Womes, M.; Chadwick, A. V.; Harrison, A.; Bruce, P. G. *J. Am. Chem. Soc.* **2006**, *128*, 12905.
- (79) Ruplecker, A.; Kleitz, F.; Salabas, E. L.; Schuth, F. *Chem. Mater.* **2007**, *19*, 485.
- (80) Shaju, K. M.; Jiao, F.; Debart, A.; Bruce, P. G. *Phys. Chem. Chem. Phys.* **2007**, *9*, 1837.
- (81) Ren, Y.; Jiao, F.; Bruce, P. G. *Micropor. Mesopor. Mat.* **2009**, *121*, 90.
- (82) Luo, J. Y.; Zhang, J. J.; Xia, Y. Y. *Chem. Mater.* **2006**, *18*, 5618.
- (83) Jiao, F.; Bruce, P. G. *Adv. Mater.* **2007**, *19*, 657.
- (84) Ren, Y.; Armstrong, A. R.; Jiao, F.; Bruce, P. G. *J. Am. Chem. Soc.* **2010**, *132*, 996.

- (85) Jiao, F.; Harrison, A.; Hill, A. H.; Bruce, P. G. *Adv. Mater.* **2007**, *19*, 4063.
- (86) Rossinyol, E.; Prim, A.; Pellicer, E.; Arbiol, J.; Hernández-Ramírez, F.; Peiro, F.; Cornet, A.; Morante, J. R.; Solovyov, L. A.; Tian, B.; Bo, T.; Zhao, D. *Adv. Funct. Mater.* **2007**, *17*, 1801.
- (87) Cui, X. Z.; Zhang, H.; Dong, X. P.; Chen, H. R.; Zhang, L. X.; Guo, L. M.; Shi, J. L. *J. Mater. Chem.* **2008**, *18*, 3575.
- (88) Zhou, L.; Ren, Q. J.; Zhou, X. F.; Tang, J. W.; Chen, Z. H.; Yu, C. Z. *Micropor. Mesopor. Mat.* **2008**, *109*, 248.
- (89) Cui, X. Z.; Shi, J. L.; Chen, H. R.; Zhang, L. X.; Guo, L. M.; Gao, J. H.; Li, J. B. *J. Phy. Chem. B* **2008**, *112*, 12024.
- (90) Yue, W. B.; Xu, X. X.; Irvine, J. T. S.; Attidekou, P. S.; Liu, C.; He, H. Y.; Zhao, D. Y.; Zhou, W. Z. *Chem. Mater.* **2009**, *21*, 2540.
- (91) Yue, W. B.; Randorn, C.; Attidekou, P. S.; Su, Z. X.; Irvine, J. T. S.; Zhou, W. Z. *Adv. Funct. Mater.* **2009**, *19*, 2826.
- (92) Ren, Y.; Hardwick, L. J.; Bruce, P. G. *Angew. Chem. Int. Ed.* **2010**, *49*, 2570.
- (93) Noda, Y.; Lee, B.; Domen, K.; Kondo, J. N. *Chem. Mater.* **2008**, *20*, 5361.
- (94) Ye, L.; Xie, S. H.; Yue, B.; Qian, L. P.; Feng, S. J.; Tsang, S. K.; Li, Y. C.; He, H. *CrystEngComm* **2010**, DOI: 10.1039/b913268f.
- (95) Lee, J.; Orilall, M. C.; Warren, S. C.; Kamperman, M.; Disalvo, F. J.; Wiesner, U. *Nat. Mater.* **2008**, *7*, 222.
- (96) Tüysüz, H.; Liu, Y.; Weidenthaler, C.; Schüth, F. *J. Am. Chem. Soc.* **2008**, *130*, 14108.
- (97) Jiao, F.; Bao, J. L.; Hill, A. H.; Bruce, P. G. *Angew. Chem. Int. Ed.* **2008**, *47*, 9711.
- (98) Ren, Y. *First Year Report of Postgraduate, University of St Andrews* **2007**.
- (99) Luo, J. Y.; Wang, Y. G.; Xiong, H. M.; Xia, Y. Y. *Chem. Mater.* **2007**, *19*, 4791.
- (100) Hill, M. R.; Booth, J.; Bourgeois, L.; Whitfield, H. J. *Dalton T* **2010**, *39*, 5306.
- (101) Lu, Y. F.; Ganguli, R.; Drewien, C. A.; Anderson, M. T.; Brinker, C. J.; Gong, W. L.; Guo, Y. X.; Soyez, H.; Dunn, B.; Huang, M. H.; Zink, J. I. *Nature* **1997**, *389*, 364.
- (102) Grosso, D.; Soler-Illia, G. J. D. A. A.; Babonneau, F.; Sanchez, C.; Albouy, P. A.; Brunet-Bruneau, A.; Balkenende, A. R. *Adv. Mater.* **2001**, *13*, 1085.
- (103) Tian, B. Z.; Liu, X. Y.; Tu, B.; Yu, C. Z.; Fan, J.; Wang, L. M.; Xie, S. H.; Stucky, G. D.; Zhao, D. Y. *Nat. Mater.* **2003**, *2*, 159.
- (104) Li, D. L.; Zhou, H. S.; Honma, I. *Nat. Mater.* **2004**, *3*, 65.
- (105) Liu, Q.; Wang, A. Q.; Wang, X. D.; Zhang, T. *Chem. Mater.* **2006**, *18*, 5153.
- (106) Polarz, S.; Orlov, A. V.; Schuth, F.; Lu, A. H. *Chem.-Eur. J.* **2007**, *13*, 592.
- (107) Ranjit, K. T.; Klabunde, K. J. *Chem. Mater.* **2005**, *17*, 65.
- (108) Roggenbuck, J.; Koch, G.; Tiemann, M. *Chem. Mater.* **2006**, *18*, 4151.

- (109) Waitz, T.; Tiemann, M.; Klar, P. J.; Sann, J.; Stehr, J.; Meyer, B. K. *Appl. Phys. Lett.* **2007**, *90*.
- (110) Zhou, H. S.; Zhu, S. M.; Hibino, M.; Honma, I.; Ichihara, M. *Adv. Mater.* **2003**, *15*, 2107.
- (111) Fan, J.; Wang, T.; Yu, C. Z.; Tu, B.; Jiang, Z. Y.; Zhao, D. Y. *Adv. Mater.* **2004**, *16*, 1432.
- (112) Jiao, F.; Bao, J. L.; Bruce, P. G. *Electrochem. Solid State Lett.* **2007**, *10*, A264.
- (113) Lim, S. Y.; Yoon, C. S.; Cho, J. P. *Chem. Mater.* **2008**, *20*, 4560.
- (114) Kim, H.; Cho, J. *J. Mater. Chem.* **2008**, *18*, 771.
- (115) Ji, X. L.; Lee, K. T.; Nazar, L. F. *Nat. Mater.* **2009**, *8*, 500.
- (116) Cheng, F.; Tao, Z.; Liang, J.; Chen, J. *Chem. Mater.* **2008**, *20*, 667.
- (117) Yuan, Q.; Liu, Q.; Song, W. G.; Feng, W.; Pu, W. L.; Sun, L. D.; Zhang, Y. W.; Yan, C. H. *J. Am. Chem. Soc.* **2007**, *129*, 6698.
- (118) Tüysüz, H.; Comotti, M.; Schüth, F. *Chem. Commun.* **2008**, 4022.
- (119) Tsoncheva, T.; Roggenbuck, J.; Tiemann, M.; Ivanova, L.; Paneva, D.; Mitov, I.; Minchev, C. *Micropor. Mesopor. Mat.* **2008**, *110*, 339.
- (120) Ma, C. Y.; Mu, Z.; Li, J. J.; Jin, Y. G.; Cheng, J.; Lu, G. Q.; Hao, Z. P.; Qiao, S. Z. *J. Am. Chem. Soc.* **2010**, *132*, 2608.
- (121) Puertolas, B.; Solsona, B.; Agouram, S.; Murillo, R.; Mastral, A. M.; Aranda, A.; Taylor, S. H.; Garcia, T. *Appl. Catal. B-Environ.* **2010**, *93*, 395.
- (122) Aranda, A.; Puertolas, B.; Solsona, B.; Agouram, S.; Murillo, R.; Mastral, A. M.; Taylor, S. H.; Garcia, T. *Catal. Lett.* **2010**, *134*, 110.
- (123) Cui, X. Z.; Zhou, J.; Ye, Z. Q.; Chen, H. R.; Li, L.; Ruan, M. L.; Shi, J. L. *J. Catal.* **2010**, *270*, 310.
- (124) Varghese, O. K.; Grimes, C. A. *J. Nanosci. Nanotechnol.* **2003**, *3*, 277.
- (125) Tiemann, M. *Chem.-Eur. J.* **2007**, *13*, 8376.
- (126) Wagner, T.; Waitz, T.; Roggenbuck, J.; Froba, M.; Kohl, C. D.; Tiemann, M. In *5th International Workshop on Semiconductor Gas Sensors (SGS 2006)*; Elsevier Science Sa: Ustron, POLAND, 2006, p 8360.
- (127) Hyodo, T.; Shimizu, Y.; Egashira, M. *Electrochemistry* **2003**, *71*, 387.
- (128) Hyodo, T.; Nishida, N.; Shimizu, Y.; Egashira, M. *Sensor Actuat. B-Chem.* **2002**, *83*, 209.
- (129) Hyodo, T.; Abe, S.; Shimizu, Y.; Egashira, M. *Sensor Actuat. B-Chem.* **2003**, *93*, 590.
- (130) Xu, X.; Tian, B. Z.; Kong, J. L.; Zhang, S.; Liu, B. H.; Zhao, D. Y. *Adv. Mater.* **2003**, *15*, 1932.
- (131) Dyer, J. A.; Trivedi, P.; Sanders, S. J.; Scrivner, N. C.; Sparks, D. L. *J. Colloid Interface Sci.* **2004**, *270*, 66.
- (132) Fuertes, A. B. *J. Phys. Chem. Solids* **2005**, *66*, 741.
- (133) Patterson, A. L. *Physical Review* **1939**, *56*, 978.
- (134) Novak, P.; Goers, D.; Hardwick, L.; Holzapfel, M.; Scheifele, W.; Ufhiel, J.; Wursig, A. *J. Power Sources* **2005**, *146*, 15.
- (135) Hardwick, L. J.; Holzapfel, M.; Novak, P.; Dupont, L.; Baudrin, E. *Electrochim. Acta* **2007**, *52*, 5357.

- (136) Dieringer, J. A.; McFarland, A. D.; Shah, N. C.; Stuart, D. A.; Whitney, A. V.; Yonzon, C. R.; Young, M. A.; Zhang, X. Y.; Van Duyne, R. P. *Faraday Discuss.* **2006**, *132*, 9.
- (137) Coelho, A. A. *J. Appl. Crystallogr.* **2000**, *33*, 899.
- (138) Brunauer, S.; Emmett, P. H.; Teller, E. *J. Am. Chem. Soc.* **1938**, *60*, 309.
- (139) Paterson, A. J., University of St Andrews, 1996.
- (140) Davidson, I. J.; Greedan, J. E. *J. Solid State Chem.* **1984**, *51*, 104.
- (141) Armstrong, A. R.; Bruce, P. G. *private communication*.
- (142) Johns, P. A.; Roberts, M. R.; Wakizaka, Y.; Sanders, J. H.; Owen, J. R. *Electrochem. Commun.* **2009**, *11*, 2089.
- (143) Huang, H.; Yin, S. C.; Nazar, L. F. *Electrochem. Solid State Lett.* **2001**, *4*, A170.
- (144) Delacourt, C.; Poizot, P.; Levasseur, S.; Masquelier, C. *Electrochem. Solid State Lett.* **2006**, *9*, A352.
- (145) Wang, Y. G.; Wang, Y. R.; Hosono, E. J.; Wang, K. X.; Zhou, H. S. *Angew. Chem. Int. Ed.* **2008**, *47*, 7461.
- (146) Kim, D. H.; Kim, J. *Electrochem. Solid State Lett.* **2006**, *9*, A439.
- (147) Meethong, N.; Huang, H. Y. S.; Speakman, S. A.; Carter, W. C.; Chiang, Y. M. *Adv. Funct. Mater.* **2007**, *17*, 1115.
- (148) Chen, G. Y.; Song, X. Y.; Richardson, T. J. *Electrochem. Solid State Lett.* **2006**, *9*, A295.
- (149) Delmas, C.; Maccario, M.; Croguennec, L.; Le Cras, F.; Weill, F. *Nat. Mater.* **2008**, *7*, 665.
- (150) Ren, Y.; Armstrong, A. R.; Jiao, F.; Bruce, P. G. *paper in preparation*.
- (151) Armstrong, G.; Armstrong, A. R.; Canales, J.; Bruce, P. G. *Chem Commun* **2005**, 2454.
- (152) Armstrong, G.; Armstrong, A. R.; Canales, J.; Bruce, P. G. *Electrochem. Solid State Lett.* **2006**, *9*, A139.
- (153) Andreev, Y. G.; Bruce, P. G. *J. Am. Chem. Soc.* **2008**, *130*, 9931.
- (154) Plitz, I.; DuPasquier, A.; Badway, F.; Gural, J.; Pereira, N.; Gmitter, A.; Amatucci, G. G. *Appl. Phys. A-Mater. Sci. Process.* **2006**, *82*, 615.
- (155) Sudant, G.; Baudrin, E.; Larcher, D.; Tarascon, J. M. *J Mater Chem* **2005**, *15*, 1263.
- (156) Jiang, C. H.; Wei, M. D.; Qi, Z. M.; Kudo, T.; Honma, I.; Zhou, H. S. *J. Power Sources* **2007**, *166*, 239.
- (157) Wagemaker, M.; Borghols, W. J. H.; Mulder, F. M. *J. Am. Chem. Soc.* **2007**, *129*, 4323.
- (158) Armstrong, A. R.; Armstrong, G.; Canales, J.; Garcia, R.; Bruce, P. G. *Adv. Mater.* **2005**, *17*, 862.
- (159) Deng, D.; Kim, M. G.; Lee, J. Y.; Cho, J. *Ener. & Environ. Sci.* **2009**, *2*, 818.
- (160) Bruce, P. G.; Armstrong, A. R.; Gitzendanner, R. L. *J. Mater. Chem.* **1999**, *9*, 193.
- (161) Robertson, A. D.; Armstrong, A. R.; Fowkes, A. J.; Bruce, P. G. *J. Mater. Chem.* **2001**, *11*, 113.
- (162) Guo, Y. G.; Hu, Y. S.; Sigle, W.; Maier, J. *Adv. Mater.* **2007**, *19*, 2087.

- (163) Eddaoudi, M.; Kim, J.; Rosi, N.; Vodak, D.; Wachter, J.; O'Keeffe, M.; Yaghi, O. M. *Science* **2002**, *295*, 469.
- (164) Ferey, G. *Chem. Soc. Rev.* **2008**, *37*, 191.
- (165) Yaghi, O. M.; O'Keeffe, M.; Ockwig, N. W.; Chae, H. K.; Eddaoudi, M.; Kim, J. *Nature* **2003**, *423*, 705.
- (166) Corma, A. *J. Catal.* **2003**, *216*, 298.
- (167) Tosheva, L.; Valtchev, V. P. *Chem. Mater.* **2005**, *17*, 2494.
- (168) Holland, B. T.; Abrams, L.; Stein, A. *J. Am. Chem. Soc.* **1999**, *121*, 4308.
- (169) Fan, W.; Snyder, M. A.; Kumar, S.; Lee, P. S.; Yoo, W. C.; McCormick, A. V.; Penn, R. L.; Stein, A.; Tsapatsis, M. *Nat. Mater.* **2008**, *7*, 984.
- (170) Jacobsen, C. J. H.; Madsen, C.; Houzvicka, J.; Schmidt, I.; Carlsson, A. *J. Am. Chem. Soc.* **2000**, *122*, 7116.
- (171) Choi, M.; Cho, H. S.; Srivastava, R.; Venkatesan, C.; Choi, D. H.; Ryoo, R. *Nat. Mater.* **2006**, *5*, 718.
- (172) Armstrong, A. R.; Bruce, P. G. *Nature* **1996**, *381*, 499.
- (173) Jean, F.; Cachet, C.; Yu, L. T.; Lecerf, A.; Quivy, A. *J. Appl. Electrochem.* **1997**, *27*, 635.
- (174) Johnson, C. S.; Mansuetto, M. F.; Thackeray, M. M.; Shao-Horn, Y.; Hackney, S. A. *J. Electrochem. Soc.* **1997**, *144*, 2279.
- (175) Suib, S. L. *Accounts Chem. Res.* **2008**, *41*, 479.
- (176) Suib, S. L. *J. Mater. Chem.* **2008**, *18*, 1623.
- (177) Jiao, F.; Bruce, P. G. *Angew. Chem. Int. Ed.* **2004**, *43*, 5958.
- (178) Kijima, N.; Ikeda, T.; Oikawa, K.; Izumi, F.; Yoshimura, Y. *J. Solid State Chem.* **2004**, *177*, 1258.
- (179) Ryoo, R.; Jun, S. *J. Phys. Chem. B* **1997**, *101*, 317.
- (180) Bragg, E. E.; Seehra, M. S. *Phys. Rev. B* **1973**, *7*, 4197.
- (181) Li, L. P.; Pan, Y. Z.; Chen, L. J.; Li, G. S. *J. Solid State Chem.* **2007**, *180*, 2896.
- (182) Yamamoto, N.; Endo, T.; Shimada, M.; Takada, T. *Japanese Journal of Applied Physics* **1974**, *13*, 723.
- (183) Mowbray, M.; Tan, X. J.; Wheatley, P. S.; Morris, R. E.; Weller, R. B. *J. Invest. Dermatol.* **2008**, *128*, 352.
- (184) Morris, R. E.; Wheatley, P. S. *Angew. Chem. Int. Ed.* **2008**, *47*, 4966.
- (185) Wheatley, P. S.; Butler, A. R.; Crane, M. S.; Fox, S.; Xiao, B.; Rossi, A. G.; Megson, I. L.; Morris, R. E. *J. Am. Chem. Soc.* **2006**, *128*, 502.
- (186) McKinlay, A. C.; Xiao, B.; Wragg, D. S.; Wheatley, P. S.; Megson, I. L.; Morris, R. E. *J. Am. Chem. Soc.* **2008**, *130*, 10440.
- (187) Xiao, B.; Wheatley, P. S.; Zhao, X. B.; Fletcher, A. J.; Fox, S.; Rossi, A. G.; Megson, I. L.; Bordiga, S.; Regli, L.; Thomas, K. M.; Morris, R. E. *J. Am. Chem. Soc.* **2007**, *129*, 1203.
- (188) Parzuchowski, P. G.; Frost, M. C.; Meyerhoff, M. E. *J. Am. Chem. Soc.* **2002**, *124*, 12182.
- (189) Smith, D. J.; Chakravarthy, D.; Pulfer, S.; Simmons, M. L.; Hrabie, J. A.; Citro, M. L.; Saavedra, J. E.; Davies, K. M.; Hutsell, T. C.; Mooradian, D. L.; Hanson, S. R.; Keefer, L. K. *J. Med. Chem.* **1996**, *39*, 1148.
- (190) Nablo, B. J.; Schoenfisch, M. H. *Biomaterials* **2005**, *26*, 4405.

- (191) Reynolds, M. M.; Hrabie, J. A.; Oh, B. K.; Politis, J. K.; Citro, M. L.; Keefer, L. K.; Meyerhoff, M. E. *Biomacromolecules* **2006**, *7*, 987.
- (192) Lai, X. Y.; Li, X. T.; Geng, W. C.; Tu, J. C.; Li, J. X.; Qiu, S. L. *Angew. Chem. Int. Ed.* **2007**, *46*, 738.
- (193) Cheah, S. F.; Brown, G. E.; Parks, G. A. *Am. Miner.* **2000**, *85*, 118.
- (194) EspadasTorre, C.; Oklejas, V.; Mowery, K.; Meyerhoff, M. E. *J. Am. Chem. Soc.* **1997**, *119*, 2321.
- (195) Mowery, K. A.; Schoenfisch, M. H.; Baliga, N.; Wahr, J. A.; Meyerhoff, M. E. *Electroanalysis* **1999**, *11*, 681.
- (196) Mowery, K. A.; Schoenfisch, M. H.; Saavedra, J. E.; Keefer, L. K.; Meyerhoff, M. E. *Biomaterials* **2000**, *21*, 9.
- (197) Mitchell-Koch, J. T.; Reed, T. M.; Borovik, A. S. *Angew. Chem. Int. Ed.* **2004**, *43*, 2806.
- (198) Oh, B. K.; Meyerhoff, M. E. *Biomaterials* **2004**, *25*, 283.
- (199) Boes, A. K.; Wheatley, P. S.; Xiao, B.; Megson, I. L.; Morris, R. E. *Chem. Commun.* **2008**, 6146.
- (200) Tocheva, E. I.; Rosell, F. I.; Mauk, A. G.; Murphy, M. E. P. *Science* **2004**, *304*, 867.
- (201) Corti, C. W.; Holliday, R. J.; Thompson, D. T. *Top Catal.* **2007**, *44*, 331.
- (202) Haruta, M.; Date, M. *Appl. Catal. A-Gen.* **2001**, *222*, 427.
- (203) Cunningham, D. A. H.; Kobayashi, T.; Kamijo, N.; Haruta, M. *Catal. Lett.* **1994**, *25*, 257.
- (204) Luo, M. F.; Zhong, Y. J.; Yuan, X. X.; Zheng, X. M. *Appl. Catal. A-Gen.* **1997**, *162*, 121.
- (205) Jansson, J. J. *Catal.* **2000**, *194*, 55.
- (206) Skoglundh, M.; Fridell, E. *Top Catal.* **2004**, *28*, 79.
- (207) Kim, M. H.; Choo, K. H. *Catal. Commun.* **2007**, *8*, 462.
- (208) Wang, Y. Z.; Zhao, Y. X.; Gao, C. G.; Liu, D. S. *Catal. Lett.* **2008**, *125*, 134.
- (209) B. Cornils, W. A. H., R. Schlögl, C.-H. Wong *Catalysis from A to Z*; Wiley-VCH: Weinheim, 2000.
- (210) Wang, D. S.; Xu, R.; Wang, X.; Li, Y. D. *Nanotechnology* **2006**, *17*, 979.
- (211) Haruta, M.; Tsubota, S.; Kobayashi, T.; Kageyama, H.; Genet, M. J.; Delmon, B. J. *Catal.* **1993**, *144*, 175.
- (212) Huang, P. X.; Wu, F.; Zhu, B. L.; Gao, X. P.; Zhu, H. Y.; Yan, T. Y.; Huang, W. P.; Wu, S. H.; Song, D. Y. *J. Phys. Chem. B* **2005**, *109*, 19169.
- (213) Zhou, K. B.; Wang, X.; Sun, X. M.; Peng, Q.; Li, Y. D. *J. Catal.* **2005**, *229*, 206.
- (214) Zheng, X. C.; Wang, S. P.; Wang, X. Y.; Wang, S. R.; Wu, S. H. *Mater. Lett.* **2005**, *59*, 2769.
- (215) Xu, R.; Wang, X.; Wang, D. S.; Zhou, K. B.; Li, Y. D. *J. Catal.* **2006**, *237*, 426.

Publication List

- [1] Lithium Intercalation into Mesoporous Anatase with an Ordered 3D Pore Structure
Y. Ren, L. J. Hardwick, P. G. Bruce, *Angew. Chem. Int. Ed.* **2010**, *49*, 2570.
- [2] Influence of Size on the Rate of Mesoporous Electrodes for Lithium Batteries
Y. Ren, A. R. Armstrong, F. Jiao, P. G. Bruce, *J. Am. Chem. Soc.* **2010**, *132*, 996.
- [3] Ordered Crystalline Mesoporous Oxides as Catalysts for CO Oxidation
Y. Ren, Z. Ma, L. P. Qian, S. Dai, H. Y. He, P. G. Bruce, *Catal. Lett.* **2009**, *131*, 146.
- [4] Tailoring the pore size/wall thickness of mesoporous transition metal oxides Y. Ren, F. Jiao, P. G. Bruce, *Micropor. Mesopor. Mat.* **2009**, *121*, 90.

List of Abbreviations and Acronyms

PXRD, powder X-ray diffraction

TEM, transmission electron microscopy

SAED, selected area electron diffraction

EDX or EDS, Energy Dispersive X-ray Spectroscopy

SBA-15, a type of mesoporous silica with one dimensional pore structure (p6mm)

KIT-6, a type of mesoporous silica with three dimensional pore structure (Ia3d)

LT-LiCoO₂, low temperature form of LiCoO₂

SQUID, superconducting quantum interference devices, they are used to measure very small magnetic fields with extremely high sensitivity.

BET, Brunauer-Emmett-Teller gas adsorption method, a 'standard' kind of surface area determination method.

BJH, Barrett, Joyner and Halenda method, a practical method of extracting mesopore distribution from isotherm data using Kelvin-based theories.

TG, thermalgravimetry

EXAFS, Extended X-Ray Absorption Fine Structure (EXAFS)

XANES, X-ray Absorption Near Edge Structure (XANES)